Dissertation
submitted to the
Combined Faculties of the Natural Sciences and Mathematics
of the Ruperto-Carola-University of Heidelberg, Germany
for the degree of
Doctor of Natural Sciences

Put forward by
Martin Gerhard Ries
Born in Gießen
Oral examination: 21.01.2015

A Two-Dimensional Fermi Gas in the BEC-BCS Crossover

Referees:	**Prof. Dr. Selim Jochim**
	Prof. Dr. Matthias Weidemüller

Abstract:

This thesis reports on the preparation of a 2D Fermi gas in the BEC-BCS crossover and the observation of the BKT transition into a quasi long-range ordered superfluid phase.

The pair momentum distribution of the gas is probed by means of a matter-wave focusing technique which relies on time-of-flight evolution in a weak harmonic potential. This distribution holds the coherence properties of the gas.

The quasi long-range ordered phase manifests itself as a sharp low-momentum peak. The temperature where it forms is identified as the transition temperature. By tuning the temperature and the interaction strength, the phase diagram of the 2D Fermi gas in the BEC-BCS crossover is mapped out.

The phase coherence is investigated in a self-interference experiment. Furthermore, algebraic decay of correlations is observed in the trap average of the first order correlation function, which is obtained from the Fourier transform of the pair momentum distribution. This is in qualitative agreement with predictions of homogeneous theory for the superfluid phase in a 2D gas.

The presented results provide a foundation for future experimental and theoretical studies of strongly correlated 2D Fermi gases. They might thus help to elucidate complex systems such as the electron gas in high-T_c superconductors.

Zusammenfassung:

Diese Arbeit beschreibt die Realisierung eines zweidimensionalen Fermi-Gases im BEC-BCS Crossover, sowie die Beobachtung des BKT-Phasenüberganges in eine superfluide Phase, welche quasi-langreichweitige Ordnung aufweist.

Die Paar-Impulsverteilung des Gases wird mit Hilfe einer Materiewellen-Fokussierungstechnik gemessen, welche auf ballistischer Expansion in einem schwachen harmonischen Potential beruht. Sie beinhaltet die Kohärenzeigenschaften des Gases.

Die Phase von quasi-langreichweitiger Ordnung zeigt sich als steiler Peak bei niedrigen Impulsen, welcher an der kritischen Temperatur zuerst auftritt. Durch Messungen bei verschiedenen Temperaturen und Wechselwirkungsstärken wird das Phasendiagramm des 2D Fermi-Gases bestimmt.

Die Phasenkohärenz wird in einem Selbst-Interferenz Experiment gemessen. Außerdem wird im Fallenmittel der Korrelationsfunktion erster Ordnung algebraischer Zerfall beobachtet. Ein solcher algebraischer Zerfall wird für die superfluide Phase in einem homogenen 2D Gas erwartet.

Diese Ergebnisse stellen die Grundlage für zukünftige experimentelle und theoretische Arbeiten über stark korrellierte 2D Fermi-Gase dar. Sie können zum Verständnis komplexer Systeme, wie dem Elektronengas in Hochtemperatur-Supraleitern beitragen.

Contents

1. Introduction

The dimensionality of a system fundamentally influences its behavior. One of the most intriguing and simultaneously technologically relevant examples are layered superconductors such as cuprates [Bed86, Wu87]. Here the electron gas is confined to quasi two-dimensional layers and the transition to the superfluid phase occurs at unusually high temperatures up to approximately 130 K [Sch93]. Unfortunately, the mechanisms which lead to this high critical temperature are not yet fully understood. This is due to the complexity of the system, which makes a rigorous theoretical treatment difficult [Nor11].

A reliable strategy used in physics to overcome such a challenge is to reduce the complexity of the system by omitting some of the details and considering only the essential properties. One can then investigate whether the simplified model still exhibits the key properties of the system, in this case the transition into a superconducting phase at high temperatures. The obtained understanding of the physics in the simplified system can then be used to understand more and more complex systems, until one arrives at the full complexity of the original problem.

A simple model for the electron gas in the layered superconductor which still features the crucial points is a two-dimensional, two-component Fermi gas with contact interactions. However, despite its simplicity it is hard to solve this model in the strongly coupled regime, where the interactions cannot be treated perturbatively. For a complete solution, which extends beyond the weakly interacting regime, a purely theoretical treatment is thus not sufficient.

To provide a benchmark for theory, we model the simplified system with a quasi two-dimensional gas of ultracold fermionic atoms in an optical dipole potential and thus perform an analog quantum simulation of its Hamiltonian [Fey82, Blo12]. Ultracold atoms are an ideal tool to engineer simple Hamiltonians. Due to their low kinetic energy, they can be described as effectively structureless bosons or fermions, which interact via a generic contact potential [Ket08]. The interaction strength between the atoms can be described by a single number, the s-wave scattering length a. It can be tuned to almost arbitrary values with the help of Feshbach resonances [Chi10]. Furthermore, ultracold atoms can be confined in magnetic and optical potentials, which allow for the creation of a wide range of geometries. In contrast to solid state systems, it is possible to realize systems which are well decoupled from the environment.

Although our model system is much simpler than the electron gas in the superconductor, it already features rich physics. At positive scattering lengths, which correspond to repulsive mean field interactions, the atoms are bound in diatomic molecules which form a bosonic superfluid phase at low temperatures due to their integer total spin. At negative scattering lengths, which correspond to attractive mean field interactions, the binding energy of the molecules becomes negligible and the system consists of attractively interacting free fermions, which can be described by BCS theory [Bar57]. By ramping the interaction strength from the bosonic side across a Feshbach resonance to the fermionic side, it is possible to continuously transform the bosonic superfluid of molecules into a fermionic superfluid of loosely bound Cooper pairs. This is the 2D equivalent of the famous 3D BEC-BCS crossover.

The 3D BEC-BCS crossover has been studied extensively in theory and in experiment [Eag69, Leg80, Reg04, Bar04, Zwi04, Ket08, Gio08, Zwe11]. Its 2D equivalent, which is investigated in this thesis, is harder to access both in theory and experiment due to its reduced dimensionality and the associated increased role of fluctuations. It has been studied theoretically in several publications, including [Ran89, Pro01, Pro02, Pet03, Isk09, Ber11, Bau14, Lev14]

A striking feature of homogeneous 2D systems is the impossibility of condensation into a true long-range ordered phase at finite temperatures [Mer66, Hoh67]. However, the transition into a quasi long-range ordered superfluid phase, where correlations decay algebraically with distance is still possible. This so-called BKT (Berezinskii, Kosterlitz, and Thouless) transition can be explained by the pairing of vortices with opposite rotation [Ber72, Kos73]. Above the transition temperature, the free vortices destroy correlations on length scales larger than the thermal wavelength. Below the transition temperature, the vortices form pairs and their rotations cancel. Hence, they do not contribute to the long-range behavior of the gas, and quasi long-range order forms. The BKT transition was first observed in a thin film of liquid ^{4}He [Bis78].

Experimentally, the realization of a truly two-dimensional gas is impossible in our three-dimensional world. However, by confining the gas in a highly anisotropic oblate potential, it is possible to freeze out motional excitations in the third dimension and thus to obtain a so-called quasi-2D system. Although it is three-dimensional on microscopic scales, this system has the density of states of a 2D system and can be described by 2D theory.

Quasi-2D ultracold quantum gases were first realized with bosonic atoms [Gör01]. The BKT phase transition was observed in this system in [Had06], and the superfluidity of the low temperature phase was experimentally confirmed in [Des12].

The preparation of a quasi-2D Fermi gas of ultracold atoms is experimentally more challenging. It was recently achieved by several groups [Gün05, Mar10, Frö11, Dyk11, Fel11, Som12, Kos12, Frö12, Zha12, Mak14]. However, the BKT transition into the quasi long-range ordered superfluid phase could not be observed until now.

This thesis reports on the direct observation of the BKT transition across the 2D BEC-BCS crossover. The coherence properties of the gas are encoded in its momentum distribution, where long-range order manifests itself as an enhanced population of low-momentum states. With the help of a matter-wave focusing time-of-flight technique, we obtain the momentum distribution of a strongly interacting two-component quasi-2D Fermi gas. At low temperatures, we observe a sharp low-momentum peak, which is a clear signature of long-range order.

By tuning the interaction strength and the temperature, we map out the phase diagram of the Fermi gas in the 2D BEC-BCS crossover. We find the transition into the long-range order phase on the bosonic as well as on the fermionic side of the crossover. In the strongly interacting limit, we find a critical temperature of $T_c/T_F \approx 0.2$. It is an order of magnitude higher than those of currently known high-T_c superconductors. An analysis of the correlation function confirms the algebraically decaying quasi long-range order in the low-temperature regime, which is predicted for the 2D superfluid phase.

Outline

This thesis is organized as follows: chapter 2 gives a brief introduction into the theory of three- and two-dimensional quantum gases. It focuses on the differences between the different dimensionalities and on the phase transition into a long-range ordered superfluid phase at low temperatures.

The experimental setup which was designed and built during this thesis is presented in chapter 3. In addition to the preparation of a quasi-2D Fermi gas in the strongly interacting regime, it also provides the possibility to prepare a gas in a single layer square optical lattice. This will enable us to simulate a large class of different Hamiltonians with our setup.

The preparation of the quasi-2D Fermi gas in our setup and the measurement process are described in chapter 4. There are several key techniques which are necessary for the preparation. They include the preparation of a degenerate gas in a single oblate layer of an optical standing wave trap, and the confirmation that the quasi-2D regime is reached where excitations in the third dimension are frozen out. The measurement process is described in the two last parts of chapter 4. They describe the calibration of the absorption imaging setup as well as a momentum space imaging technique. This technique allows the identification of pair condensation across the BEC-BCS crossover in a consistent way.

With these experimental tools at hand, chapter 5 presents the results of our measurements. After a description of how temperature, non-thermal fraction, and the critical temperature of the superfluid transition are extracted, the obtained phase diagram is shown. Furthermore, the analysis of the coherence properties of the superfluid phase is described.

The thesis concludes in chapter 6 with a summary of the measured data and an outlook. Since a large part of this thesis consisted in the planning and setting up of the experimental apparatus, the outlook not only features physics directly connected to the presented experiments, but also gives a perspective for other future experiments with the apparatus.

2. Low-Dimensional Quantum Gases

In the experiments described in this thesis, a strongly interacting quasi two-dimensional (quasi-2D) Fermi gas is created and its properties are examined as a function of interaction strength and temperature.

A quasi-2D system is characterized by an effectively frozen out third dimension, which leads to a many-body behavior governed by 2D physics. This is for example the case in materials like graphene or layered superconductors, where the electron gas is confined in two-dimensional planes [Nor11, Jos13]. Although axially excited quantum states still exist, they are not populated since they have an energy which is higher than all other energy scales of the system. The density of states is thus that of a 2D system, and the macroscopic properties can be described in the 2D framework [Pet00, Mar10].

However, when the energy of the particles becomes close to that of the first axially excited state, the residual influence of the third dimension becomes important. In this regime, the critical temperature for superfluid pair condensation is predicted to be enhanced [Fis14]. This effect could help explain the high critical temperatures found in quasi-2D solid state systems.

The chapter starts by reviewing the few-body physics in a quantum gas. First, the properties of fermions and bosons and the experimental realization of a quantum gas with ultracold atoms are investigated. Then, the interactions in such a gas are reviewed while considering the dimensionality of the sample. In the second part of the chapter, the many-body physics of the system are discussed. This part focuses on the condensation into a superfluid phase in the BEC-BCS crossover between an effectively bosonic and a fermionic system. Unlike in three dimensions, the superfluid in two dimensions does not exhibit true long range order at finite temperature. Instead, it features quasi long range order, which is characterized by algebraically decaying phase correlations.

2.1. Fermions and Bosons

In a system where the de-Broglie wavelength $\lambda_{dB} = h/p$ [Bro23], where h is Planck's constant and p is the momentum of a particle, of the constituting particles becomes comparable to the interparticle spacing, quantum mechanical behavior becomes relevant. The particles then have to be described in terms of their wave function. Due to the overlap of their wave functions, identical particles thus become indistinguishable, i.e.

$$|P_{\mu\nu}\Psi|^2 = |\Psi|^2, \tag{2.1}$$

where Ψ is the many-body wave function of the system and $P_{\mu\nu}$ is an operator which exchanges the μth and the νth identical particle [Sak94]. In particular, exchanging the same pair of particles twice must not change the wave function, and $P_{\mu\nu}$ must have the eigenvalues ±1. Equation (2.1) thus yields two solutions:

$$P_{\mu\nu}\Psi = -\Psi \quad \text{and} \quad P_{\mu\nu}\Psi = +\Psi. \tag{2.2}$$

These two solutions define two classes of particles:

- **Fermions** fulfill the antisymmetric solution and carry a half-integer spin. Due to their antisymmetry, no state can be occupied by more than one particle: if the μth and the νth particle are in the same single-particle quantum state, their exchange must not change the many-body wave function. This directly contradicts the antisymmetric solution in equation (2.2). Hence, two identical fermions must not occupy the same single-particle quantum state. This fundamental law is known as the Pauli exclusion principle [Pau25].
- **Bosons** comply with the symmetric solution and carry an integer spin. Due to their symmetric behavior under particle exchange, there is no restriction for the occupation number of single-particle states.

It is important to note that a dimer consisting of two fermions has an integer spin and thus behaves as a boson as long as its binding energy is big compared to all other energy scales.

2.2. Realization of a Quantum Gas with Ultracold Atoms

In this thesis, we realize a gas in which the quantum mechanical behavior of the constituents becomes relevant as described above, with ultracold neutral atoms. Although they are composite particles, the internal structure is not resolved when the atoms scatter with each other at low energies. The atoms can then be treated as effective structureless bosons or fermions, depending on their total spin. We conduct our experiments with fermionic atoms. This allows to compare our results to the technologically relevant electron gas.

Although this realization of a quantum gas does not occur in nature, it has several benefits which make it an ideal system for our studies. The atoms in an ultracold gas interact with each other by means of scattering interactions. Due to their low collision energies, the interaction is well described by s-wave scattering on a generic point-like pseudopotential. Thus, the interaction can be described by a single number, the so-called scattering length a. This feature is described in chapter 2.2.1. It enables the realization of many-body systems which can be described by simple model Hamiltonians. In contrast, the electron gas exhibits long-range Coulomb interactions which make the theoretical treatment difficult.

In addition, ultracold gases provide the possibility to tune the interparticle interactions to almost arbitrary values by means of so-called Feshbach resonances. This is described in chapter 2.2.2. Closely related to the mechanism of these resonances is the existence of a universal two-body bound state. The bosonic character of this dimer and its dependence on the interaction strength lead to rich many-body physics. In particular, they are the key ingredients of the BEC-BCS crossover, which is described in chapter 2.3.

Furthermore, ultracold atoms can be confined in almost arbitrary trapping geometries. This allows for the experimental realization of a large class of different systems. In this thesis, the behavior of an ultracold quantum gas in a quasi-2D layer is investigated. Thus, the influence of the quasi-2D geometry on the physics in the gas is taken into account in the following chapters.

2.2.1. Interactions in an Ultracold Quantum Gas

This chapter reviews the interaction properties in a quantum gas of ultracold atoms which interact via two-body scattering.

The scattering cross section between the atoms is influenced by the dimensionality of the system in two ways: the scattering process itself depends on the dimensionality, and the density of available states for the scattering particles changes as will be shown in detail in chapter 2.3.1. Thus, this chapter treats scattering processes in 3D, in 2D, and in the quasi-2D regime, where the scattering process is three-dimensional but the density of states is that of a 2D system.

3D

In a 3D quantum gas with a radially symmetric short range interaction potential $V_{int}(r)$, the two-body scattering process is described in the center of mass frame by the Schrödinger equation [Gio08]

$$\left[\frac{\mathbf{p}^2}{2m_r} + V_{int}(r)\right]\psi(\mathbf{r}) = E\psi(\mathbf{r}) \quad . \tag{2.3}$$

Here, both $\mathbf{r} = \mathbf{r_1} - \mathbf{r_2}$ and $\mathbf{p} = \mathbf{p_1} - \mathbf{p_2}$ are given in relative coordinates, and $m_r = \frac{m_1 m_2}{m_1 + m_2}$ is the reduced mass. Equation 2.3 can be solved by an incoming plain wave ψ_0 and a scattered spherical wave ψ_s:

$$\psi(\mathbf{r}) \propto \psi_0(\mathbf{r}) + \psi_s(\mathbf{r}) \propto e^{ik_0 z} + f(k,\theta)\frac{e^{ikr}}{r} \tag{2.4}$$

where k_0 and k are the wave numbers of the incoming and scattered wave, respectively. The scattering cross section $\frac{d\sigma}{d\Omega}$ is determined by the scattering amplitude $f(\theta)$ as

$$\frac{d\sigma}{d\Omega} = \begin{cases} |f(k,\theta)|^2 & \text{for non-identical particles} \\ |f(k,\theta) - f(k,\theta+\pi)|^2 & \text{for identical fermions} \\ |f(k,\theta) + f(k,\theta+\pi)|^2 & \text{for identical bosons} \quad . \end{cases} \tag{2.5}$$

The results for identical fermions and bosons are different from the one for non-identical particles due to the different symmetry constraints of their wave functions.

The scattering amplitude f can be found by a partial wave expansion in terms of angular momentum l. Assuming low energy scattering, which is reasonable for an ultracold gas, angular momenta $l \geq 1$ are frozen out due to the centrifugal barrier. The scattering amplitude is then dominated by the so-called s-wave term with $l = 0$ [Ket08]:

$$f(k) = \frac{1}{k \cot \delta_0(k) - ik} \quad , \tag{2.6}$$

where δ_0 is the phase shift between the incoming and the scattered wave.

This solution is spherically symmetric, which has an important consequence: together with equation 2.5, it becomes evident that $d\sigma/d\Omega = 0$ for identical fermions. Thus, they do not interact with each other in s-wave scattering. A Fermi gas interacting via s-wave scattering can hence only be realized with at least two different kinds of fermions, which are then distinguishable and can interact.

The scattering amplitude f only depends on the wave vector k and the phase shift δ_0 of the scattered particles. Since these two quantities are not independent of each other, it is possible to describe the whole scattering process by a single number, the scattering length a. It can be found by expanding $k \cot \delta_0$ in k [Ket08]:

$$k\ \cot\delta_0(k) \approx -\frac{1}{a} + \frac{k^2}{2} r_{\text{eff}} \quad , \tag{2.7}$$

where r_{eff} is the effective range of the scattering potential. For low momenta $kr_{\text{eff}} \ll 1$, the scattering length is thus given by

$$a = -\frac{\tan\delta_0}{k} \quad . \tag{2.8}$$

The low energy scattering amplitude can now be rewritten as

$$f(k) = \frac{1}{-\frac{1}{a} + \frac{k^2}{2} r_{\text{eff}} - ik} \quad . \tag{2.9}$$

For $r_{\text{eff}} \ll k$, $f(k)$ can be simplified in two limits:

$$f = \begin{cases} -a & \text{for } k|a| \ll 1 \quad \text{(weakly interacting regime)} \\ \frac{i}{k} & \text{for } k|a| \gg 1 \quad \text{(unitary regime)} \quad . \end{cases} \tag{2.10}$$

In the weakly interacting regime, all interactions in the system are thus exclusively described by the scattering length a, which hence takes the role of an interaction parameter. In the unitary regime, which is reached in close vicinity of a scattering resonance where a diverges (see chapter 2.2.2), the interactions are limited by the wave vector k of the scattering particles.

For a de-Broglie wavelength $\lambda_{dB} \gg r_{\text{eff}}$ (as it is the case for the experiments with ultracold atoms described in this thesis), the interatomic potential is not resolved. The scattering process therefore becomes universal and can be described as a contact interaction [Ket08] with a pseudo-potential

$$V(\mathbf{r}) = g\,\delta(\mathbf{r}) \tag{2.11}$$

with the delta function δ [1] and the interaction strength

$$g = \frac{4\pi\hbar^2 a}{m} \quad . \tag{2.12}$$

The mean-field interaction energy in a sample with homogeneous density $n = N/V$

---

[1] In order to avoid divergence, the delta function still has to be regularized by replacing it with $\delta(\mathbf{r})\frac{\partial}{\partial r}r$.

is then given by [Wei09]

$$E_{\text{int}}(a) = g\,n = \frac{4\pi\hbar^2 n}{m} a \quad . \tag{2.13}$$

For $a > 0$, the mean-field interaction energy is thus positive which leads to a repulsive mean-field interaction. For $a < 0$, it is negative and the mean-field interaction is attractive.

2D

In a two-dimensional quantum gas, contact interactions between the constituting particles can be treated similarly to the 3D case. However, due to the different density of available quantum states and the reduced dimensionality of the scattering process itself, the results are slightly different. The s-wave scattering amplitude in the 2D system is given by [Lev14]

$$f_{2D}(k) = \frac{-4}{\cot\delta_0(k) - i} \quad . \tag{2.14}$$

Similar to the 3D case, the phase shift δ_0 can be expanded according to

$$\cot\delta_0(k) = \frac{2}{\pi}\ln(ka_{2D}) + \mathcal{O}(k^2) \quad , \tag{2.15}$$

where a_{2D} is the 2D scattering length. This leads to

$$f_{2D}(k) = \frac{-4}{\frac{2}{\pi}\ln(ka_{2D}) - i} \tag{2.16}$$

for low momenta. The interaction parameter of the 2D system is thus $\ln(ka_{2D})$.

To describe a many-body system, it is helpful to use a characteristic momentum scale of the system for the interaction parameter. In a Fermi gas, this momentum scale is given by the Fermi momentum k_F (see chapter 2.3.2). Thus, the dimensionless interaction parameter of the 2D Fermi gas is $\ln(k_F a_{2D})$. Similar to the 3D case, the mean-field interactions for $\ln(k_F a_{2D}) > (<)\ 0$ are attractive (repulsive).

Quasi-2D

In a quasi-2D system, the motion of particles is confined to a two-dimensional plane. Thus, the density of available quantum states is that of the 2D system, and the macroscopic properties of the system can be described by 2D theory [Pet00, Mar10]. In particular, the scattering amplitude in the quasi-2D system is given by equation 2.16 as in the 2D case [Blo08]. The interaction parameter for the quasi-2D Fermi gas is thus also $\ln(k_F a_{2D})$.

However, unlike in the true 2D case the third dimension still exists. In a typical quasi-2D system of ultracold atoms, the length scale of the interaction potential $V_{int}(r)$ is given by the van-der-Waals length $l_{vdW} \approx 50a_0 \approx 3\,\mathrm{nm}$, which is considerably smaller than that of the confinement to the 2D plane. Thus, the microscopic scattering process has to be described in three dimensions and the 2D scattering length a_{2D} can be derived from the 3D scattering length a.

For a harmonically confined quasi-2D quantum gas, the 2D scattering length can thus be calculated from the 3D scattering length a and the harmonic oscillator length $\ell_z = \sqrt{\hbar/m\omega_z}$ of the tight confinement [Lev14]. It is given by

$$a_{2D} = \ell_z \sqrt{\frac{\pi}{A}} \exp\left(-\sqrt{\frac{\pi}{2}}\frac{\ell_z}{a}\right) \quad , \tag{2.17}$$

where $A \approx 0.905$ [Pet01, Blo08]. In [Lev14], this expression is derived directly from the scattering properties of the particles in a T-Matrix approach. It is found to be valid for all interaction strengths and only requires the scattering energy to be negligible as compared to the strength of the tight confinement, which is automatically given in a quasi-2D framework. Thus, although there are other definitions of a_{2D} [Pet01, Blo08], in this thesis the definition according to equation 2.17 is used for all interaction strengths.

In analogy to the 3D case, the 2D interaction strength is then [Had11]

$$g_{2D} = \frac{\sqrt{8\pi}\hbar^2(a/\ell_z)}{m} = \frac{\hbar^2}{m}\tilde{g}_{2D} \tag{2.18}$$

with the dimensionless 2D coupling constant $\tilde{g}_{2D} = \sqrt{8\pi}(a/\ell_z)$.

2.2.2. Tuning the Interaction Strength: Feshbach Resonances

This chapter reviews the tunability of the scattering length a and thus the mean-field interaction between the particles in an ultracold quantum gas. In this system, the scattering length can be tuned easily by means of Feshbach resonances [Fes58, Chi10].

A Feshbach resonance is a scattering resonance which occurs when two free scattering atoms can couple to a bound state during the scattering process. This is depicted in figure 2.1. The atoms scatter in the so-called open channel, which corresponds to a certain spin configuration (black). At the same time, there is a different spin configuration called the closed channel (red), where there is a bound state close to the scattering continuum. Due to energy conservation, the atoms cannot enter the closed channel, which has a larger continuum energy. However when the energy difference $\Delta\epsilon$ between their incident energy and the bound state becomes small, they can couple to that state during the scattering process. For $\Delta\epsilon \to 0$, the scattering length diverges. It is positive when the bound state lies below the scattering continuum, and negative when it lies above.

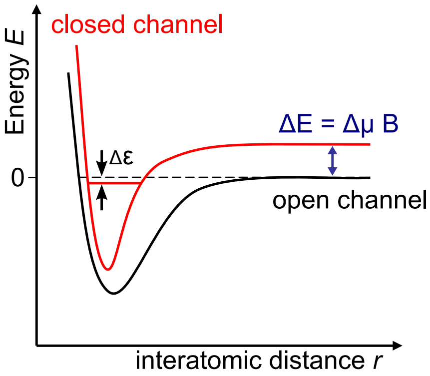

Figure 2.1.: Schematic model of a Feshbach resonance. Two atoms scatter with each other in a certain spin configuration, the so-called open channel (black interatomic potential). Their incident energy is negligible in the ultracold regime and can thus be approximated by the continuum of the open channel. There exists a spin configuration of the atoms which supports a bound state (closed channel, red interatomic potential). Due to the higher energy of the closed channel continuum, the atoms cannot access the closed channel. However if the energy difference $\Delta\epsilon$ between the bound state and the energy of the atoms is small, the free atoms can couple to the bound state and the scattering length a is resonantly enhanced. If there is a difference $\Delta\mu$ in magnetic moment between the two channels, $\Delta\epsilon$ and thus a can be tuned with the help of a homogeneous magnetic field B. Adapted from [Chi10].

If the two channels have different magnetic momenta μ, e.g. due to their different spin configuration, it is possible to tune their relative energies by applying a magnetic field B:

$$\Delta E = \Delta\mu \, B \quad . \tag{2.19}$$

Here, ΔE is the energy difference between the continua of the two channels, and $\Delta\mu$ is the difference in magnetic momentum.

The scattering length a can thus be tuned by the application of a magnetic offset field B. Its dependence on B can be modelled by [Chi10]

$$a(B) = a_{bg}\left(1 - \frac{\Delta}{B - B_0}\right) \quad , \tag{2.20}$$

where a_{bg} is the background scattering length, Δ is the width of the resonance, and B_0 its position.

The experiments described in this thesis are realized with ultracold ^{6}Li atoms. With a nuclear spin of $I = 1$ and an electronic spin of $S = 1/2$, ^{6}Li is an effective fermion. Hence, in order to obtain an interacting gas, two different spin states of the atoms are necessary. The experiments are thus conducted with a balanced mixture of the two lowest Zeeman sublevels, which are denoted $|1\rangle$ and $|2\rangle$ (see figure 2.2).

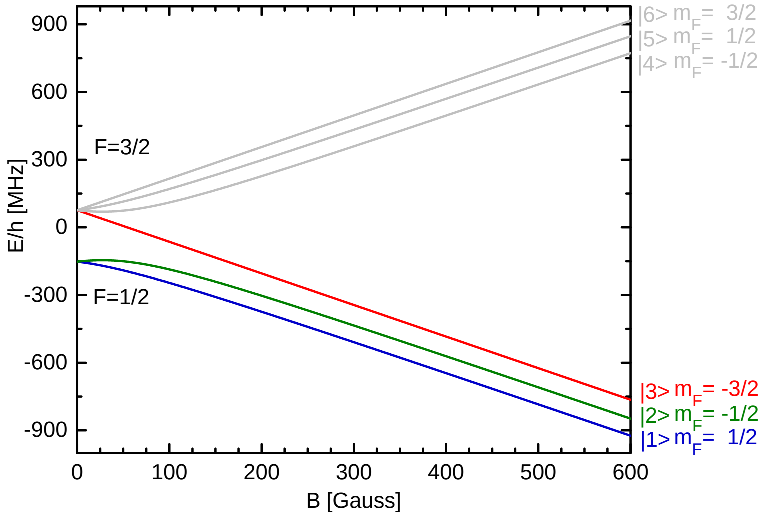

Figure 2.2.: Zeeman sublevels of the ^{6}Li $2\,^2S_{1/2}$ ground state. At low magnetic fields, it splits into a hyperfine doublet ($F = 1/2$) and a quadruplet ($F = 3/2$). At higher fields, the spins decouple and there are three $m_J = -1/2$ and three $m_J = +1/2$ states, which are labeled $|1\rangle$ through $|6\rangle$. Mixtures of the high field seeking states $|1\rangle$ - $|3\rangle$ are stable against spin-changing collisions and thus experimentally accessible. In the high field regime, they have magnetic moments of $\mu \approx \mu_{Bohr}/\hbar$. Atoms can be transferred between these states via radio-frequency (RF) transitions ($\Delta E \approx h \cdot 80\,\mathrm{MHz}$). Calculated according to [Bre31].

The scattering length between ultracold ^{6}Li atoms in state $|1\rangle$ and $|2\rangle$ is shown in figure 2.3 (A) for magnetic offset fields between 0 Gauss (G) and 1500 G. There is a broad Feshbach resonance at $B_0 = 832.2\,\mathrm{G}$ [Zür13], where the scattering length diverges. On the left side of the resonance, $a > 0$ and thus the mean field interaction is repulsive, until a crosses zero at 527 G. On the right side of the resonance, $a < 0$ and the mean field interaction is attractive.

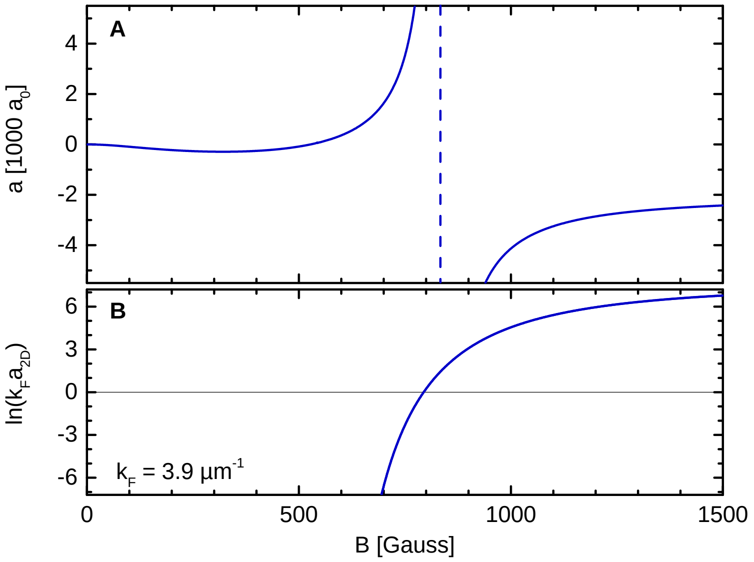

Figure 2.3.: **(A)** s-wave scattering length a between ^{6}Li atoms in state $|1\rangle$ and $|2\rangle$ in units of the Bohr radius a_0 as a function of the magnetic offset field B. The Feshbach resonance at $B_0 = 832.2\,\mathrm{G}$ is used in the experimental part of this thesis. Note that the narrow resonance at 543 G is not resolved in the plot. Data taken from [Zür13].
(B) $\ln(k_F a_{2D})$ as a function of B. a_{2D} is calculated from a using equation (2.17), assuming $\ell_z = 551.2\,\mathrm{nm}$ and $k_F = 3.9\,\mu\mathrm{m}^{-1}$, which are typical experimental values. For $a \to 0$ (527 G), $\ln(k_F a_{2D})$ diverges. Due to the large values of $\ln(k_F a_{2D})$ around the divergence, this is not shown in the figure.

The 2D interaction parameter $\ln(k_F a_{2D})$ of our harmonically trapped quasi-2D system is shown in figure 2.3 (B). It is calculated with equation 2.17, assuming typical experimental values of $\ell_z = 551.2\,\mathrm{nm}$ and $k_F = 3.9\,\mu\mathrm{m}^{-1}$. In contrast to a, it shows no divergence, but instead becomes zero where the sign of mean-field interactions changes. Unlike in the 3D case, this point can be tuned by changing k_F. This can be achieved by tuning the particle number (see equation 2.35), which directly corresponds to a change of the density. In a harmonically trapped system with fixed particle number, the density and thus k_F also change with temperature.

Bound State

Closely related to the mechanism of the Feshbach resonance is the existence of a two-body bound state. The binding energy of this dimer becomes universal when the scattering length is substantially larger than the effective range of the interatomic interaction potential, $a \gg r_{\text{eff}}$. It is thus independent of the microscopic properties of the atoms and only depends on the mass of its constituents and on a.

The experiments described in this thesis are conducted at magnetic offset fields between 692 G and 1400 G. In this regime, $|a| \gtrsim 1460\, a_0$ (see figure 2.3 (A)). The effective range of the attractive interatomic potential is given by the van-der-Waals length as $r_{\text{eff}} = l_{vdW} \approx 62.5a_0$ for ^{6}Li [Bra09]. Thus, the two-body bound state is well approximated by the universal description.

In 3D, the binding energy of the universal dimer is given as

$$E_B = \frac{\hbar^2}{2m_r a^2} \tag{2.21}$$

for $a > 0$. For $a < 0$, the dimer becomes unbound. Here, m_r is the reduced mass of the two particles. In our case, where both particles are atoms of the same species, $m_r = m/2$.

The situation is different in 2D where $a_{2D} > 0$ for positive and negative interaction parameters. Here, the dimer, whose binding energy is defined similarly to the 3D case as [Lev14]

$$E_{B,2D} = \frac{\hbar^2}{2m_r a_{2D}^2} \quad , \tag{2.22}$$

remains bound for all values of $\ln(k_F a_{2D})$.

In the experimentally accessible quasi-2D scenario, equation 2.22 does not hold. This is due to the introduction of the additional length scale ℓ_z of the tight confinement. Here, the dimer binding energy can be calculated from a via the transcendental equation [Pet01, Blo08, Lev14]

$$\frac{\ell_z}{a} = \int_0^\infty \frac{du}{\sqrt{4\pi u^3}} \left(1 - \frac{\exp(\frac{-E_{B,q2D}}{\hbar\omega_z} u)}{\sqrt{\frac{1}{2u}(1-\exp(-2u))}} \right) \quad . \tag{2.23}$$

This definition is valid under the assumptions that $(r_{\text{eff}}/\ell_z)^2 \to 0$, which is well fulfilled in our system. The quasi-2D dimer binding energy $E_{B,q2D}$ is displayed in figure 2.4 for our system, together with the 3D and 2D binding energy. For large binding energies ($\ell_z/a \gg 1$), the size of the dimer is on the order of $a \ll \ell_z$. It is thus only weakly perturbed by the tight confinement and its binding energy approaches that of the 3D dimer. For small binding energies ($\ell_z/a \ll -1$), the dimer becomes large. It is thus strongly influenced by the confinement and behaves like the 2D dimer. In particular, it remains bound for all $\ln(k_F a_{2D})$. The binding energy $E_{B,q2D}$ has been measured to agree well with the theoretical values using RF spectroscopy on ultracold atoms in two independent experiments [Som12, Bau12].

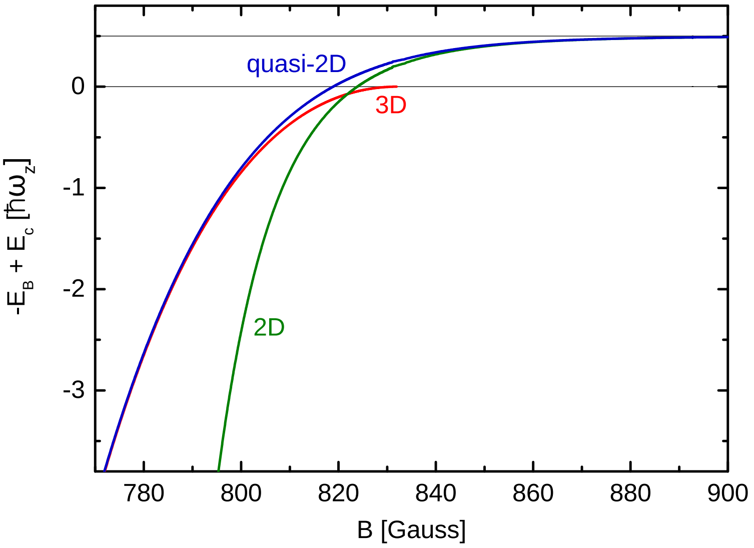

Figure 2.4.: Binding energy of the universal dimer in quasi-2D (blue, calculated according to equation (2.23)), 2D (green, equations (2.22) and (2.17)) and 3D (red, equation (2.21)) for ^{6}Li atoms in states $|1\rangle$ and $|2\rangle$. The quasi-2D confinement is given by $\ell_z = 551.2$nm. Whereas the 3D dimer becomes unbound on resonance (832.2 G), the quasi-2D and 2D dimers stay bound. The continuum of the quasi-2D dimer is shifted up to $E_c = 1/2\,\hbar\omega_z$ by the strong harmonic confinement. The continuum of the 2D dimer has thus been adjusted likewise. $E_{B,q2D}$ approaches the 3D solution in the limit of large binding energies, where the dimer becomes small and is not influenced by the confinement. For small binding energies, where the dimer is large and is thus heavily modified by the confinement, $E_{B,q2D}$ approaches the 2D case.
The quasi-2D binding energy is plotted over the full magnetic field range covered in our experiments in figure A.1 in the appendix.

2.3. Many-Body Physics in Ultracold Quantum Gases

After the few-body physics in an ultracold quantum gas has been introduced in the last chapter, this chapter gives an overview over the many-body properties.

Aside from interactions, the properties of such a gas are mainly determined by the quantum statistics of the constituting particles and the geometry of the system, which influences the density of states. These two parameters are first discussed in a general way. Then, the resulting properties of Fermi- and Bose gases in three and two dimensions are reviewed with a focus on the condensation into a superfluid phase in the Bose gas. In 3D, the famous BEC transition into a superfluid phase with true long-range order occurs at low temperatures. In 2D, Bose-Einstein condensation is forbidden at finite temperatures by the Mermin-Wagner theorem [Mer66]. However, there is a Berezinskii-Kosterlitz-Thouless (BKT) transition into a superfluid phase which exhibits quasi long-range order [Ber72, Kos73]. Finally, the BEC-BCS crossover, which connects bosonic and fermionic superfluidity is discussed. The 3D crossover has been subject to intense studies. In contrast, its 2D counterpart is not well understood yet. The experiments presented later in this thesis will thus be a benchmark for current theoretical models and contribute to the understanding of this intriguing phenomenon.

2.3.1. Quantum Statistics and Density of States

The population of energy states in fermionic or bosonic many-body systems is given by the Fermi-Dirac and Bose-Einstein distribution functions, respectively:

$$f^{\pm}(E) = \frac{1}{e^{(E-\mu)/k_B T} \pm 1}, \tag{2.24}$$

where the $+$ ($-$) holds for fermions (bosons) [Fli10]. Here, μ is the chemical potential and k_B is Boltzmann's constant. As will be detailed in chapter 2.3.2 and 2.3.3, fermions and bosons consequently behave fundamentally different for $T \to 0$. Fermions fulfill the Pauli principle and continuously populate all available quantum states from the lowest available energy to the Fermi energy E_F. In contrast, bosons only occupy the lowest quantum states, where they may form a Bose-Einstein condensate (BEC). This is depicted in figure 2.5 for a harmonically confined gas .

In addition to the distribution function of the particles in a system, the density of available quantum states $g(E)$ also fundamentally determines the many-body properties.

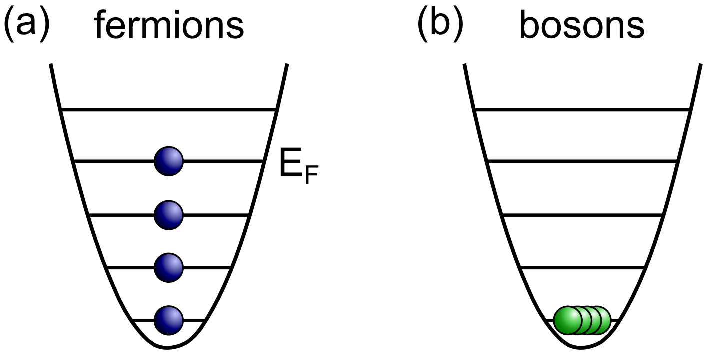

Figure 2.5.: Sketch of fermions (a) and bosons (b) in a harmonic potential at $T = 0$. Whereas fermions populate states up to the Fermi energy E_F, bosons condense in the lowest state in 3D and 2D. Adapted from [Wen13].

It is instructive to calculate $g(E)$ from the total number of available states $G(E)$ at energies up to E. $G(E)$ can be found by dividing the energetically accessible phase space by the size of a phase space cell [Pet02]. For a free particle with a maximum momentum $p = (2mE)^{1/2}$ in a homogeneous 3D volume L^3, this leads to

$$G(E) = \frac{\frac{4\pi}{3}(2mE)^{3/2}L^3}{(2\pi\hbar)^3} \quad . \tag{2.25}$$

The density of states is then

$$g_{3D}(E) = \frac{dG(E)}{dE} = \frac{L^3 m^{3/2}}{\sqrt{2}\pi^2\hbar^3}E^{1/2} \tag{2.26}$$

for $E > 0$. In 2D, the same argumentation leads to

$$g_{2D}(E) = \frac{L^2 m}{2\pi\hbar^2} \quad . \tag{2.27}$$

Unlike in the 3D case, g_{2D} is thus not energy dependent.

The total particle number N is now related to the distribution function and the density of states like

$$N = N_0 + \sum_{E>0} f(E)\, g(E) \quad . \tag{2.28}$$

where N_0 is the number of atoms in the ground state. In a semiclassical approximation it can be replaced by

$$N = N_0 + N_{ex} = N_0 + \int_0^\infty f(E)\, g(E)\, dE \quad . \tag{2.29}$$

2.3.2. Ideal Fermi Gases

In contrast to bosons, fermions cannot minimize their energy by condensing into the ground state due to the Pauli principle. For $T \to 0$, they thus fill up all quantum states from the lowest available energy to the Fermi energy E_F , which is defined as the chemical potential μ at zero temperature, $E_F \equiv \mu(T = 0)$. Thus, in the thermodynamic limit, the so-called Fermi sphere forms in momentum space.

3D

For a given particle number N, the Fermi energy E_F can be found by solving equation (2.28) at $T = 0$, where the Fermi distribution becomes

$$f^+(E) = \begin{cases} 1 & ; \; E < E_F = \mu(T = 0) \\ 0 & ; \; E > E_F = \mu(T = 0) \quad . \end{cases} \tag{2.30}$$

Thus, equation (2.28) simplifies to

$$N = N_0 + \int_0^{E_F} g(E)\, dE \tag{2.31}$$

in the semiclassical approximation (2.29). Due to the Pauli principle, one can safely neglect N_0 in the thermodynamic limit. Inserting g_{3D} from equation (2.26), one obtains

$$E_{F,3D} = \frac{\hbar^2}{2m} (6\pi^2 n_{3D})^{2/3} \quad . \tag{2.32}$$

Note that this is the Fermi energy of the one-component Fermi gas. In the experimentally relevant case of a two-component gas, n_{3D} thus corresponds to the density of one spin component.

From E_F, on can now define the Fermi temperature $T_F = E_F/k_B$ and the Fermi wave vector $k_F = \sqrt{2mE_F}/\hbar$, which give the system its characteristic temperature and momentum scales. It is important to note that these definitions are also used to describe interacting Fermi gases or even Bose gases, where no Fermi surface exists. They should then be interpreted as a scale for the density of the gas.

2D

The Fermi energy of the ideal homogeneous 2D Fermi gas can be obtained analogously to the 3D case as

$$E_{F,2D} = \frac{\hbar^2}{2m} (4\pi n_{2D}) \quad , \tag{2.33}$$

where again n_{2D} is the 2D density of one spin component.[2] This yields the Fermi temperature

$$T_{F,2D} = \frac{\hbar^2}{2mk_B}(4\pi n_{2D}) \tag{2.34}$$

and the Fermi wave vector

$$k_{F,2D} = \sqrt{4\pi n_{2D}} \quad . \tag{2.35}$$

Here, n_{2D} is the 2D density. As in the 3D case, it is common to also describe the interacting Fermi gas and the Bose gas by these terms.

In our experiments, we use a harmonically trapped gas. Here, the density of states and thus the Fermi energy is altered by the trap. However, it is possible to rescale the measured data to the homogeneous system by means of local density approximation (LDA). To do this, we use the central 2D density n_0 as n_{2D} to obtain the Fermi energy, temperature, and wave vector. We thus map the area of highest phase space density, where condensation occurs first, to the homogeneous gas. This is described in chapter 5.1.

2.3.3. Bose Gases

As mentioned above, bosons do not obey the Pauli exclusion principle. Thus, for low temperatures they minimize their energy by condensing into the lowest available quantum state, where they form a superfluid. The properties of this superfluid phase are influenced by the dimensionality of the system: whereas in 3D true long range order (TLRO) is allowed for finite temperatures, it only occurs for zero temperature in 2D. However, there is still a superfluid at finite temperature in 2D, which is then characterized by quasi long range order (QLRO).

3D

In an ideal homogeneous three-dimensional Bose gas, all atoms condense into the motional ground state for $T \to 0$. This can be shown by evaluating equation (2.29)

$$N = N_0 + N_{ex} = N_0 + \int_0^\infty f(E)\, g(E)\, dE$$

under the assumption of zero occupation of the ground state, i.e. $N_0 = 0$. Under the constraint of $\mu \leq 0$, which has to be fulfilled for the Bose gas, this leads to a

---

[2] In the experiment, we perform state-selective imaging, which directly yields the 2D density of one spin component.

maximum allowed phase space density [Pet02, Had11]

$$\rho_{3D} = n\lambda_{dB}^3 \leq \frac{2}{\pi}\int_0^\infty \frac{\sqrt{x}dx}{e^x - 1} = \zeta(3/2) \approx 2.612 \tag{2.36}$$

with the Riemann zeta function ζ. Thus, as the phase space density grows above $\rho = \rho_{BEC} \approx 2.612$, the ground state has to be macroscopically occupied and Bose-Einstein condensation (BEC) into a superfluid phase occurs. By plugging in the de-Broglie wavelength $\lambda_{dB} = h/p = 2\pi\hbar/\sqrt{2mk_BT}$, one can thus find the transition temperature T_{BEC}.

By evaluating the number of particles in the excited states N_{ex} in equation (2.29) for the critical value of $\mu = 0$ below T_{BEC}, one finds [Pet02]

$$N_{ex}(T) = N\left(\frac{T}{T_{BEC}}\right)^{3/2} \quad . \tag{2.37}$$

Thus, the number of particles in the ground state grows smoothly with decreasing temperature:

$$N_0(T) = N - N_{ex}(T) = N\left[1 - \left(\frac{T}{T_{BEC}}\right)^{3/2}\right] \quad . \tag{2.38}$$

This result is quantitatively valid also for the trapped 3D Bose gas. However, the exponent of the temperature dependence changes. For the experimentally relevant case of a gas in a 3D harmonic potential, it becomes 3. A general treatment can for example be found in [Pet02].

The observed condensation into the lowest energy state goes along with the appearance of long range correlations. To study these correlations, it is useful to introduce the first order correlation function [Had11]

$$g_1(\mathbf{r_0} + \mathbf{r}, \mathbf{r_0}) = \left\langle \hat{\Psi}^\dagger(\mathbf{r_0} + \mathbf{r})\,\hat{\Psi}(\mathbf{r_0})\right\rangle \quad , \tag{2.39}$$

where $\hat{\Psi}(\mathbf{r})$ is the annihilation operator for a particle at position $\mathbf{r}$ and $\hat{\Psi}^\dagger(\mathbf{r})$ the respective creation operator. In a homogeneous system, $g_1(\mathbf{r_0} + \mathbf{r}, \mathbf{r_0})$ can be written as $g_1(\mathbf{r})$. It is the Fourier transform of the momentum distribution $n(\mathbf{k})$ [Pit03]. The momentum distribution can be obtained by rewriting equation (2.29) in momentum space. At low temperatures, the condensate is clearly visible as a delta peak at zero momentum:

$$n(\mathbf{k}) = N_0\delta(\mathbf{k}) + n_{ex}(\mathbf{k}) \quad . \tag{2.40}$$

The thermal part n_{ex} of the momentum distribution follows a Gaussian. Thus, the first order correlation function $g_1(r)$ also exhibits a Gaussian decay, which is on the length scale of the de-Broglie wavelength λ_{dB}. A purely thermal gas at $T > T_{BEC}$ thus exhibits no long-range order beyond the thermal length scale. In contrast, the delta shaped condensed part transforms into a constant offset in $g_1(r)$. Thus, for $T < T_{BEC}$, $g_1(r)$ converges towards a non-zero constant for large distance r. Thus, the sample exhibits correlations over an infinite range. This behavior is called true long-range order (TLRO).

2D

In the homogeneous ideal 2D Bose gas, where the density of states is not energy dependent, an evaluation of equation (2.29) equivalent to the discussed 3D case yields

$$\rho_{2D} = n_{2D}\lambda_{dB}^2 = -\ln\left(1 - e^{\mu/k_B T}\right) \quad , \tag{2.41}$$

which always has a valid solution with $\mu \leq 0$ for finite ρ_{2D}. Thus, no Bose-Einstein condensation into the ground state occurs at finite temperatures.

The situation becomes more interesting when interactions are introduced: as in the ideal gas, true long range order is possible only in the experimentally irrelevant case of $T = 0$ [Bog60, Mer66, Hoh67] in a homogeneous 2D Bose gas with weak repulsive short range interactions. However, for sufficiently low temperatures $T < T_c$, there is a transition into a superfluid low-momentum phase with a slow algebraic decay of correlations with r [Blo08, Had11], i.e.

$$g_1(r) \propto r^{-\eta} \quad . \tag{2.42}$$

Similar to the 3D case, one can treat the superfluid and the thermal part of the gas separately. The phase transition can then be understood by an argumentation which neglects the thermal part [Had11]. Since the thermal part exhibits only short-range correlations, this simplification is justified for the description of the long-range behavior.

In the presence of interactions, density fluctuations in the gas are strongly suppressed at low temperatures on length scales greater than the healing length $\xi = \hbar/\sqrt{m g_{2D} n}$. Here, m is the particle mass, g_{2D} is the 2D interaction strength, and n is the 2D density. Thus, one can assume that at low temperatures excitations only affect the phase θ of the superfluid wave function, which can be written as

$$\hat{\Psi}_s(\mathbf{r}) = \left|\hat{\Psi}_s(\mathbf{r})\right| e^{i\theta(\mathbf{r})} = \sqrt{n_s} e^{i\theta(\mathbf{r})} \quad . \tag{2.43}$$

Here, $n_s < n$ is the density of the superfluid phase. There are two kinds of excitations which affect the phase: phonon excitations, which correspond to smooth variations of the phase, and vortices. A vortex is a topological excitation around which the phase θ circulates by a multiple of 2π. Thus, the superfluid density in the vortex core vanishes. Furthermore, vortices carry a quantized angular momentum and lead to a rotation of the superfluid around the vortex core. Without a transfer of angular momentum into the sample, they can thus only form in pairs of opposite rotation.

One can intuitively understand that the excitation of a vortex requires a higher energy than that of a phonon. Thus, at low temperatures vortices can be neglected and only phonon excitations are relevant. Since the energy arising from interactions is constant in this approximation, one can then describe the gas by an effective Hamiltonian

$$H_\theta = \frac{\hbar^2}{2m} n_s \int d^2r (\nabla\theta)^2 \quad . \tag{2.44}$$

This Hamiltonian is the continuous generalization of the XY spin model. In contrast to the discrete XY Hamiltonian, it does not allow for vortices since it assumes constant superfluid density for arbitrarily short length scales. In the presence of vortices, this assumption does not hold due to the vanishing superfluid density in their cores, where the phase is not defined. However, it is possible to include vortices by means of a UV cutoff.

In the homogeneous case, the first order correlation function of this system can be written as

$$g_1(\mathbf{r}) = \left\langle \hat{\Psi}^\dagger(\mathbf{r})\, \hat{\Psi}(\mathbf{0}) \right\rangle = n_s \left\langle e^{i(\theta(\mathbf{r})-\theta(0)} \right\rangle \quad . \tag{2.45}$$

In the presence of phonon excitations, it can be calculated to be [Had11]

$$g_1(r) = n_s \left(\frac{r}{\xi}\right)^{-1/(n_s\lambda_{dB}^2)} \quad . \tag{2.46}$$

The correlations thus exhibit an algebraic decay. This slow decay, which does not exhibit a typical length scale is called quasi long range order (QLRO). Like true long-range order (TLRO), it is a necessary and sufficient condition for superfluidity [Blo08].

At temperatures $T > T_c$ above the superfluid transition temperature, the 2D Bose gas does not exhibit long range correlations. However, depending on the phase space density of the gas, there are two regimes where correlations decay in different ways. Assuming the non-interacting case, they can be found by Fourier transforming the momentum distribution of the thermal gas, which one obtains by setting $N_0 = 0$ in equation (2.29) and plugging in the Bose distribution (2.24) in its momentum representation. In combination with the relation between the phase space density $n_{2D}\lambda_{dB}^2$ and the chemical potential μ given by equation (2.41), the momentum distribution yields the following behavior of the correlation function [Had11]:

In the non-degenerate regime, where $n_{2D}\lambda_{dB}^2 \ll 1$, the Gaussian momentum distribution leads to a fast Gaussian decay of correlations on the length scale $\lambda_{dB}/\sqrt{\pi}$, similar to the 3D thermal gas:

$$g_1(r) \approx n e^{-\pi r^2/\lambda_{dB}^2} \quad . \tag{2.47}$$

In the degenerate regime, where $n_{2D}\lambda_{dB}^2 > 1$, the momentum distribution still has a Gaussian high-momentum tail. Thus, the correlations are Gaussian at short length scales up to the thermal wavelength, and follow equation (2.47). At longer length scales however, $g_1(r)$ is dominated by the low-momentum part of the momentum distribution, which is enhanced above the Gaussian distribution [Pro01, Pro02, Bis09] and can be described by a Lorentzian. At length scales above λ_{dB}, the correlation function can thus be approximated by an exponential decay

$$g_1(r) \approx e^{-r/\ell} \quad , \tag{2.48}$$

where the decay length ℓ can be approximated by $\ell \approx \lambda_{dB} e^{n\lambda_{dB}^2/2}/\sqrt{4\pi}$. In the presence of interactions, the behavior is qualitatively similar.

When analyzing the momentum distribution of the 2D gas, one has to take this so-called pre-superfluid enhancement of low momenta into account. For $T \leq T_c$, the non-Gaussian fraction N_q/N of the momentum distribution is expected to be roughly equal to the superfluid fraction N_s/N. At T_c however, the behavior of N_q/N deviates from that of N_s/N. Whereas N_s/N jumps to zero at T_c, as will be shown below, N_q/N smoothly decreases with temperature and stays finite for $T > T_c$. This behavior has been experimentally verified in several independent measurements [Cla09, Tun10, Hun11, Pli11].

The phase transition between the QLRO superfluid phase and the normal phase is driven by the vortex excitations. For $T > T_c$, free vortices exist and destroy the long range order. At T_c, vortices of opposite rotation form bound pairs. Their rotations thus annihilate on length scales greater than the pair size, which is on the order of the healing length ξ. Hence, only phonon excitations are relevant for the long-range behavior of the system and one obtains the above described slow algebraic decay of correlations.

This topological phase transition was first described by Berezinskii [Ber72] and Kosterlitz and Thouless [Kos73] and is thus called Berezinskii-Kosterlitz-Thouless (BKT) transition. It has been observed in superfluid Helium films [Bis78] as well as quasi-2D ultracold Bose gases [Had06, Krü07, Cla09, Des12].

To obtain more information about the phase transition, it is instructive to calculate the free energy $F = E - TS$ which is needed to create a vortex in the gas. Assuming a circularly symmetric gas with radius $R \to \infty$, it can be found to be [Had11]

$$F = \frac{1}{2k_B T}(n_s \lambda^2 - 4) \ln \left(\frac{R}{\xi} \right) \quad . \tag{2.49}$$

Again, only the superfluid density of the gas is used for this calculation. Since the thermal part of the gas has no long-range phase coherence, the vortex creates no rotation in it.

The free energy cost F of a vortex shows a change of sign at $n_s \lambda^2 = 4$. For large superfluid phase space densities $n_s \lambda^2 > 4$, F is positive. Thus, the creation of a vortex would require energy. For small superfluid phase space densities $n_s \lambda^2 < 4$ however, F is negative and the system can minimize its energy by the creation of free vortices. Since each vortex reduces the superfluid density n_s even further, the creation of more vortices becomes even more favorable. Thus, the superfluid density exhibits a sudden jump between $n_s = 4/\lambda_{dB}^2$ and $n_s = 0$, which one can associate with the critical temperature T_c [Nel77, Had11]. This is fundamentally different to Bose-Einstein condensation in 3D, where the superfluid fraction increases smoothly.

One can obtain an upper bound for T_c from $n_s = 4/\lambda_{dB}^2$ under the assumption that the whole sample becomes superfluid at the transition, i.e. $n_s = n_{2D}$. With $\lambda_{dB} = h/p = 2\pi\hbar/\sqrt{2mk_B T}$, this leads to $T_c = \pi^2 \hbar^2 n_{2D}/2mk_B$. By introducing the Fermi temperature (equation (2.34)) as a density scale, one can rewrite this upper bound for the critical temperature as $T_c \leq 0.125\, T_F$.

To obtain a better prediction for the critical temperature, one has to include the non-superfluid fraction of the gas into the analysis. With the help of quantum Monte Carlo calculations, one obtains the total phase space density at the critical temperature ρ_c [Pro01, Had11]:

$$\rho_c = (n\lambda_{dB}^2)_c = ln(C/\tilde{g}_{2D}) \quad , \tag{2.50}$$

where $C = 380 \pm 3$ and $\tilde{g}_{2D}$ is the dimensionless 2D coupling constant defined in equation (2.18). This relation is valid in the weak coupling limit ($\tilde{g}_{2D} \ll 1$).

In the presence of a trap, where size of the gas becomes finite and the density of states is modified, the condensation into a 2D BEC with TLRO is allowed for finite temperatures. One expects this transition to occur below T_c [Blo08]. Thus, when cooling the gas down, one will first observe the above described BKT transition into the QLRO superfluid phase at T_c as in the homogeneous case. The

BKT transition will first occur in the middle of the trap, where the density (and thus ρ) is the highest. As T is decreased further, the size of the superfluid region will grow. This behavior leads to a suppression of the sudden jump in superfluid density observed in the homogeneous system [Hol07]. At the same time, it also makes the distinction between QLRO and TLRO difficult, since the superfluid phase always has a finite size. It is therefore not clear whether it is possible to observe a clear transition between the QLRO and the TLRO regime.

2.3.4. Interacting Fermi Gases: the BEC-BCS Crossover

The existence of the effectively bosonic two-body bound state in a Fermi gas (see chapter 2.2.2) leads to the rich physics of the so-called BEC-BCS crossover. Here, the gas can be continuously transferred from a gas of bosonic molecules to one of unbound Fermions. After a brief discussion of the 3D BEC-BCS crossover, the properties of the 2D BEC-BCS crossover are reviewed below with a focus on the aspects relevant for this thesis. This ultimately leads to the phase diagram of the strongly interacting Fermi gas in the BEC-BCS crossover, which is explored experimentally in this thesis.

3D

For a Fermi gas with weakly repulsive mean field interactions, i.e. small positive scattering length a, the two-body bound state exists and is deeply bound. The resulting molecules consist of two fermions with half-integer spin and thus have an integer total spin. For sufficiently large E_B, the structure of the molecules is not resolved, and they behave like effective bosons. For $T \to 0$, these bosons condense into the motional ground state, and form a superfluid molecular Bose-Einstein condensate (BEC) as described in the previous chapter [Joc03, Gre03, Zwi03]. Hence, this limit is called the BEC limit.

Far on the other side of the resonance, where a is small and negative, no two-body bound state exists. The system thus consists of free fermions with a weak attractive mean field interaction. According to BCS theory [Bar57], two fermions of opposite momentum at the Fermi surface can form a bosonic Cooper pair [Bar57]. It is important to note that the Cooper pairs are not two-body bound states, but rather a many-body phenomenon which is caused by collective interactions of the particles close to the Fermi surface. The Cooper pairs condense into a BCS superfluid phase [Zwi05] with TLRO whose energy is lowered into the Fermi sphere by the pairing energy Δ. Consequently, this limit is called the BCS limit.

By adiabatically ramping the magnetic field across the Feshbach resonance, it is possible to smoothly transform the two limits of a BEC superfluid and a BCS superfluid into each other [Eag69, Leg80, Reg04, Bar04, Zwi04]. This is called the BEC-BCS crossover. It has been subject to intense theoretical and experimental studies and is treated in great detail in many books and review articles such as [Gio08, Ket08, Zwe11].

2D

In 2D, the BEC and BCS limit are reached for $\ln(k_F a_{2D}) \ll -1$ and $\ln(k_F a_{2D}) \gg 1$, respectively. Similar to the 3D case, a 2D Fermi gas on the BEC side of the crossover consists of deeply bound bosonic molecules. However, there is no Bose-Einstein condensation but a BKT transition into a superfluid state with QLRO for $T > 0$ in the homogeneous case, similar as in the 2D Bose gas (see chapter 2.3.3).

Although for $\ln(k_F a_{2D}) > 0$, the two-body bound state still exists, it is only loosely bound, and can be broken up when μ and $k_B T$ become on the order of its binding energy. Thus, the system becomes fermionic for sufficiently large $\ln(k_F a_{2D})$, in analogy to the 3D case.

The crossover point between bosonic and fermionic character can be defined as the point where the chemical potential μ crosses zero [Lev14]. This can be motivated by looking at the single-particle excitation spectrum [Zwi06, Lev14]. At zero temperature, it is given by

$$E(k) = \sqrt{\left(\frac{\hbar^2 k^2}{2m} - \mu\right)^2 + \Delta^2} \quad . \tag{2.51}$$

For $\mu > 0$, the minimum pairing gap Δ, which corresponds to the energy needed to excite a particle out of the condensate, lies at finite momentum k. Thus, all pairing occurs at this finite momentum, which can then be interpreted as the remnant of a Fermi surface in the strongly interacting regime. For $\mu < 0$, $E(k)$ has its minimum at $k = 0$, which resembles the bosonic case where no Fermi surface is present.

In mean-field theory, $\mu = 0$ corresponds to $\ln(k_F a_{2D}) = 0$[Lev14]. However, quantum Monte-Carlo calculations see the crossover point further on the fermionic side, at $\ln(k_F a_{2D}) \approx 0.5$ (see figure 2.6) [Ber11, Nga13, Lev14]. So far, experimental results have not given a conclusive answer [Som12].

In the fermionic limit with weak attractive interaction, the system can be described by loosely bound Cooper pairs in the framework of BCS theory as in the 3D case. Similar to the 3D case, Cooper pairing occurs for sufficiently low temperatures. Due to the 2D geometry, there is no condensation into a TLRO superfluid phase at finite temperatures, as already described for the bosonic case (see chapter 2.3.3). However, the formation of a QLRO superfluid phase with a finite pairing gap Δ is possible.

It is worth noting that in 2D, the crossover can be driven by both the interaction strength and the Fermi momentum k_F, which directly corresponds to the density of the gas. It is thus possible to access arbitrary points in the crossover by varying the density at a constant interaction strength. This is fundamentally different from the 3D case, where the crossover can only be driven by the interactions. One has to keep this in mind when doing experiments, especially with (inhomogeneously) trapped gases, where the density is influenced by the temperature as well as the interaction strength.

There have been many theoretical approaches to compute T_c as a function of the interaction parameter $\ln(k_F a_{2D})$. However, a complete description including the strongly interacting region has not been achieved so far, and one has to interpolate between the two weakly interacting limits to obtain a complete phase diagram.

In the weakly interacting Bose limit ($\ln(k_F a_{2D}) \ll -1$), the critical temperature is [Pet03, Pro01, Pro02]

$$\frac{T_c}{T_F} = \frac{1}{2}\left[\ln\frac{C}{4\pi} + \ln\Big(\ln(4\pi) - 2\ln(k_F a_{2D})\Big)\right]^{-1} \tag{2.52}$$

with the same $C = 380 \pm 3$ as in equation (2.50).

For $\ln(k_F a_{2D}) \gg 1$, the gas can be described by BCS theory and T_c is equivalent to the temperature where the BCS pairing gap becomes zero [Bot06, Lev14],

$$\frac{T_{c,\mathrm{BCS}}}{T_F} = \frac{2e^{\gamma}}{\pi k_F a_{2D}} \tag{2.53}$$

with the Euler constant $\gamma \approx 0.577$. This formula does not take into account particle-hole fluctuations around the Fermi surface. Introducing them into the system with the help of the so-called Gor'kov-Melik-Barkhudarov (GMB) correction leads to [Pet03]

$$\frac{T_c}{T_F} = \frac{2e^{\gamma-1}}{\pi k_F a_{2D}} \quad . \tag{2.54}$$

By interpolating between the solutions for T_c across $\ln(k_F a_{2D}) = 0$, one can draw an approximate phase diagram of the 2D Fermi gas in the BEC-BCS crossover (Figure 2.6). Since both solutions for T_c increase for $\ln(k_F a_{2D}) \to 0$, one expects a maximum in the vicinity of the crossover point.

Increased Critical Temperature in Quasi-2D

In a recent theoretical work, the critical temperature is calculated in a quasi-2D geometry in the BCS limit [Fis14]. The gas is strongly confined in axial direction

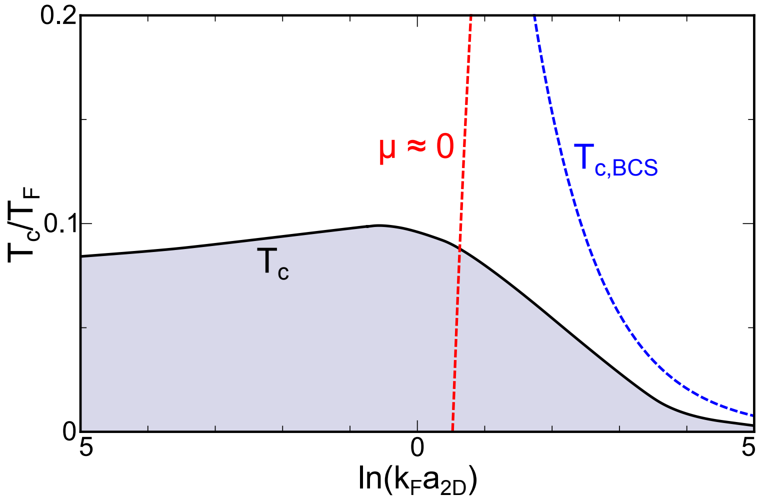

Figure 2.6.: Schematic phase diagram of the 2D Fermi gas in the BEC-BCS crossover. The gray area represents the superfluid QLRO phase. The transition temperature T_c to the white normal phase is given by equation (2.52) for $\ln(k_F a_{2D}) \ll -1$ and by equation (2.54) for $\ln(k_F a_{2D}) \gg 1$. Across $\ln(k_F a_{2D}) = 0$, T_c is interpolated. The blue dashed line shows the critical temperature obtained from BCS theory (equation (2.53)). The red dashed line corresponds to the crossover point, which is given by $\mu = 0$. Taken from [Lev14].

but homogeneous in radial direction. Using BCS theory and assuming infinitely many harmonic axial trap levels, it is shown that when $E_F/\hbar\omega_z$ is increased, T_c/T_F also increases significantly. The increase continues in the transition regime between quasi-2D and 3D, where a small number of axial trap levels is populated. This is interesting as it might help explain the still not well understood high critical temperatures which are measured in the quasi-2D electron gas in high-T_c superconductors.

3. Experimental Setup

In this chapter, the experimental setup which was planned and built during this thesis is described. In order to minimize downtime and achieve high control over the sample, we kept the design as basic as possible and focused on reliability and state-of-the-art technology in each component.

All experiments are conducted in an ultra-high vacuum chamber, which we designed to provide as much optical access to the sample as possible. Fermionic ^{6}Li atoms are evaporated in an oven and are collimated into an atom beam. We slow atoms from the beam from approximately $1500\,\mathrm{m/s}$ to $50\,\mathrm{m/s}$ with the help of a Zeeman slower and subsequently capture them in a magneto-optical trap (MOT). There, we cool a gas of approximately 10^8 atoms down to several $100\,\mu\mathrm{K}$. In the next step, we transfer it into an optical dipole trap. There, we evaporatively cool the atomic gas of states $|1\rangle$ and $|2\rangle$ into quantum degeneracy at several $10\,\mathrm{nK}$. We transfer the resulting BEC of approximately 10^5 diatomic molecules into a single layer of a standing-wave optical dipole trap. It provides a pancake-shaped trapping potential with a large aspect ratio which enables us to study the gas in the quasi-2D regime. In order to manipulate the atoms, we are able to apply homogeneous magnetic fields as well as magnetic field gradients. After preparing the sample with the desired parameters, we destructively detect its density distribution by means of absorption imaging. In this technique, the sample casts a shadow in a flash of resonant light. We record this shadow on a CCD camera. The experiment cycle takes approximately 10 seconds, and we repeat it several times for each set of parameters to obtain sufficient statistics.

Since most parts of the apparatus needed for the above mentioned steps have been previously described in various Bachelor- and Master theses, this chapter only briefly describes the setup. For more detailed descriptions and characterizations, the reader is referred to the respective theses.

3.1. Vacuum Chamber

In order to conduct experiments with ultracold gases, an excellent isolation from the environment is necessary. Since the temperature of the sample and the depth of the confining trap is usually on the order of $100\,\mathrm{nK}$, collisions with a thermal background gas would quickly destroy the sample. Hence, the experiments are conducted in an ultra-high vacuum environment to minimize these collisions. At the same time, it is crucial to have good optical access to the sample, both for the application of optical trapping potentials and for imaging. We thus use a spherical octagon as main chamber, which allows for full optical access on four axes, through six horizontal viewports with a numerical aperture of NA ≈ 0.15, and two vertical reentrant viewports with NA ≈ 0.88 (see figure 3.1).

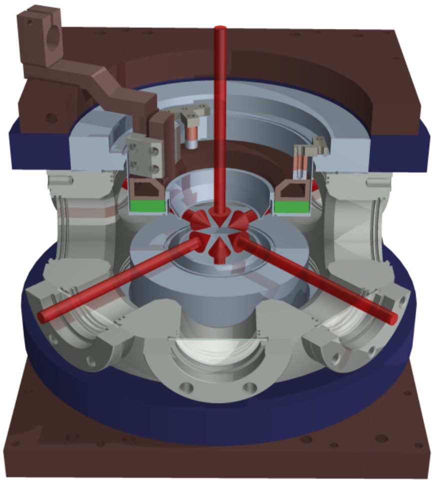

Figure 3.1.: Main chamber with MOT beams (red arrows), MOT coils (blue), and offset field coils (green), and the respective water cooled copper heat sinks (brown). In addition to the Zeeman slower axis, optical access is possible in three horizontal axes and one vertical axis. Taken from [Wen13].

The complete vacuum chamber is shown in figure 3.2. It is pumped by titanium sublimators and ion pumps, which do not create mechanical vibrations. The pressure is approximately $1 \cdot 10^{-11}$ mbar at the vacuum gauge close to the window of the Zeeman slower beam. It should be considerably lower in the main chamber which is coated with a non-evaporable getter coating (NEG). This coating provides additional pumping speed at the exact location where low pressure is crucial. More information on the vacuum setup can be found in [Rie10].

The optics for trapping and imaging in the horizontal axes are mounted on a U-shaped optical breadboard, which encloses the vacuum chamber 10 cm below the optical axes. In order to minimize vibrations and warping, it is machined from 25 mm cast aluminum and mounted on the optical table with approximately 30 aluminum posts with a diameter of 38 mm. The optical setup on the breadboard is shown in figure 3.3.

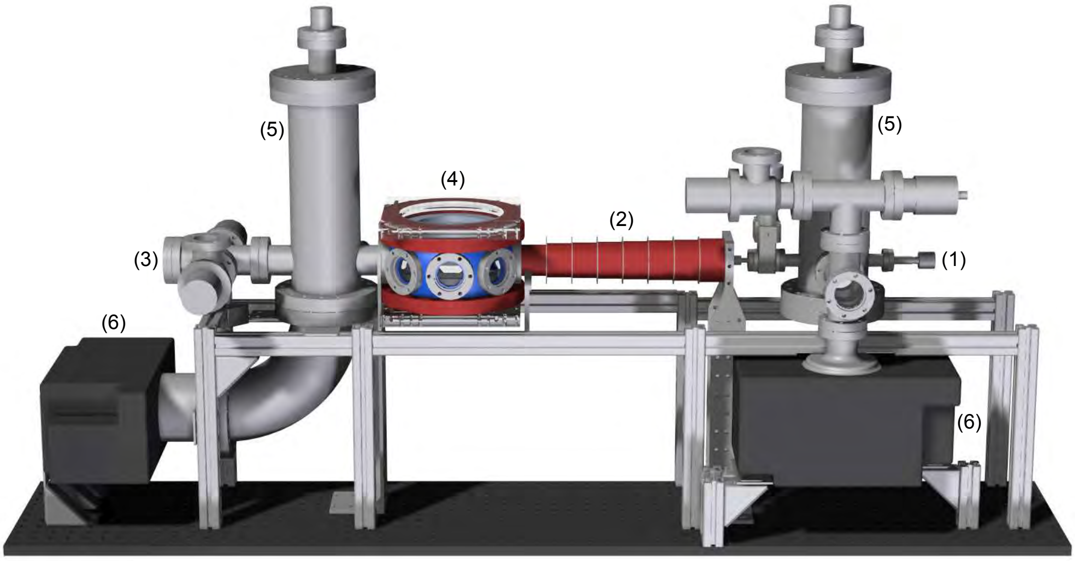

Figure 3.2.: Vacuum chamber. ^{6}Li atoms are evaporated in the oven (1). The resulting atom beam is collimated by an aperture and slowed down in the Zeeman slower (2) by a resonant laser beam entering the chamber through the window (3). The atoms are then trapped in the main chamber (4). The vacuum is maintained by titanium sublimators in the two pumping towers (5), and by two ion pumps (6). Additionally, there is a non-evaporable getter coating (NEG) in the main chamber. The Zeeman slower pipe also acts as a differential pumping stage between the main section and the oven section, where the pressure is higher. Taken from [Rie10].

3.2. Magneto-Optical Trap and Zeeman Slower

At the beginning of each experimental cycle, we capture and precool ^{6}Li atoms provided by an atom beam from the 350 °C oven with the combination of a Zeeman slower and a magneto-optical trap (MOT).

The atoms leave the oven with a longitudinal velocity of approximately 1500 m/s. In the Zeeman slower, they are decelerated by the subsequent absorption and spontaneous emission of photons from a resonant laser beam which is directed against their propagation direction. The deceleration over the length of the Zeeman slower tube leads to a spatially varying Doppler shift of their resonance frequency. To compensate for this Doppler shift, the resonance frequency is Zeeman shifted by a spatially varying magnetic field along the propagation direction [Met02]. We use

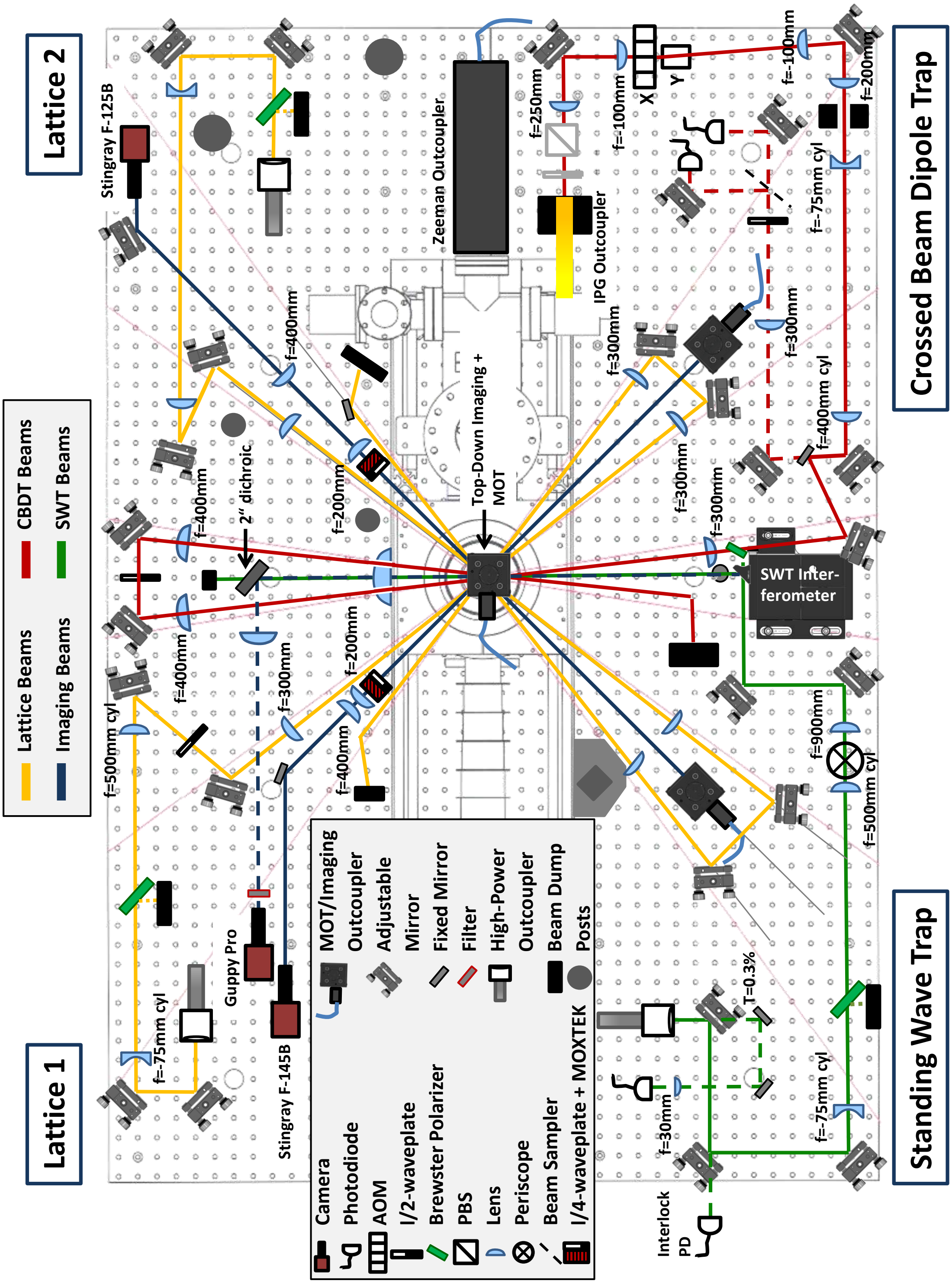

Figure 3.3.: Optical setup around the main chamber. The imaging beams as well as the beams for crossed beam optical dipole trap (CBODT), the standing wave trap (SWT) and the 2D optical lattice are shown. The MOT beams are omitted for clarity. Adapted from [Nei13].

a decreasing field geometry, so that the anti-Helmholtz field of the MOT coils can provide the Zeeman slower field on the last centimeters. At the end of the Zeeman slower, a large fraction of the atom beam has been slowed down to a velocity of approximately 50 m/s and can thus be captured by the MOT.

In the MOT, the atoms are trapped and cooled by the combination of three slightly red-detuned pairs of retroreflected laser beams and the zero-crossing of an anti-Helmholtz magnetic field [Met02]. This combination provides both a restoring force, which keeps the atoms in the trap, and a damping force, which slows down the motion of the atoms and thus cools them. Due to the continuous scattering of atoms with resonant photons, the minimum achievable temperature in the MOT is limited by the so-called Doppler temperature, which is in the case of ^{6}Li given by approximately 140 μK.

The three retroreflected pairs of 11 mm diameter MOT beams and the MOT coils which create the anti-Helmholtz field can be seen in figure 3.1. While operating the MOT, we keep the magnetic field gradient provided by the anti-Helmholtz field at approximately 30 G/cm, which corresponds to a current of approximately 32 A in the MOT coils.

The Zeeman slower and the MOT use the ^{6}Li D2 line, which corresponds to the transition between the $2\,^2S_{1/2}$ ground state and the $2\,^2P_{3/2}$ excited state and lies at approximately 671 nm. Whereas the hyperfine splitting of the excited state cannot be resolved, that of the ground state is 228.2 MHz wide. This makes it necessary to use two laser frequencies labeled cooler and repumper for the Zeeman slower and the MOT. In this way, both transitions are driven and atoms do not accumulate in an unaddressed dark state.

The light is provided by a diode laser with a tapered amplifier (Toptica TA pro), which is beat-offset locked [Sch99] to a separate spectroscopy setup. The beam is split up into a cooler and a repumper fraction, which are shifted by ± 114.1 MHz by two acousto-optic modulators (AOMs). The detuning of both fractions is then adjusted by the the beat-offset lock. The MOT- and Zeeman slower beams are transferred to the breadboard around the vacuum chamber by glass fibers. The total laser power in each beam after the fiber is approximately $10 - 20$ mW for the MOT beams, and $30 - 60$ mW in the Zeeman slower beam, depending on the life cycle of the tapered amplifier chip.

The combination of Zeeman slower and MOT leads to loading rates of up to $3 \cdot 10^8$ atoms/s at moderate oven temperatures of 350 °C, which allow for an oven lifetime of several years. Thus, after a loading time of only 1 s,[1] the MOT provides a sufficient number of atoms at a temperature of several 100 μK which can then be

---

[1] Depending on the life cycle of the tapered amplifier chip and thus the available laser power, we load the MOT for to up to 3 s.

transferred into the crossed beam optical dipole trap (CBODT) for further cooling. More information on the setup and performance of Zeeman Slower and MOT can be found in [Rie10] and [Sim10].

3.3. Optical Dipole Traps

After the initial trapping and precooling of the gas in our MOT, the further cooling steps and all the experiments are performed in optical dipole traps (ODT). They are realized by focused non-resonant laser beams and provide a conservative potential which is proportional to the laser intensity. This makes it possible to realize trapping potentials with various shapes, especially when interference effects are used. Furthermore, the optical dipole potential is independent of additional magnetic offset fields or gradients. Optical dipole traps thus have a great advantage over magnetic traps, where it is not possible to apply arbitrary additional magnetic fields.

In this chapter, our different optical dipole traps are described after a brief review of the working principle of an ODT.

3.3.1. Working Principle

The optical dipole potential that an atom experiences in a light field can be intuitively understood in a classical picture as explained in [Gri00]. In this picture, the oscillating electric field of the laser beam induces a dipole moment in the atom. The dipole moment oscillates in phase with the field for laser frequencies ω_L smaller than the atom's resonance frequency ω_0, and out of phase for $\omega_L > \omega_0$. Thus, for a red-detuned laser beam ($\omega_L < \omega_0$) the dipole potential is attractive and the atom is pulled towards the highest intensity. For a blue detuned beam ($\omega_L > \omega_0$), the potential is repulsive and the atom is pushed away from the highest intensity.

For large detuning and negligible saturation, the dipole potential and the scattering rate of photons with the trapped atoms can be written as

$$U_{\mathrm{dip}}(\mathbf{r}) = -\frac{3\pi c^2}{2\omega_0^3}\left(\frac{\Gamma}{\omega_0-\omega_L}+\frac{\Gamma}{\omega_0+\omega_L}\right) I(\mathbf{r}) \quad . \tag{3.1}$$

and

$$\Gamma_{\mathrm{sc}}(\mathbf{r}) = \frac{3\pi c^2}{2\hbar\omega_0^3}\left(\frac{\omega_L}{\omega_0}\right)^3\left(\frac{\Gamma}{\omega_0-\omega_L}+\frac{\Gamma}{\omega_0+\omega_L}\right)^2 I(\mathbf{r}) \quad . \tag{3.2}$$

Here, the damping rate Γ is given by the line width of the spontaneous transition,

c is the speed of light, and $I(\mathbf{r})$ is the laser intensity.

Whereas both U_{dip} and Γ_{sc} depend linearly on I, the dependence on the detuning $\omega_0 - \omega_L$ is linear for U_{dip} and quadratic for Γ_{sc}. One can thus minimize the scattering rate for a given potential depth by choosing a large detuning. Since every scattering process heats the sample, this is desirable. At the same time, a large detuning also makes high laser intensities necessary to achieve sufficiently deep traps.

In our experiments, we use red-detuned (and thus attractive) optical dipole traps at a wavelength around 1064 nm, which is widely available. This relatively large detuning from the transition at 671 nm leads to low scattering rates. At the same time, the necessary laser powers of up to 200 W are still experimentally feasible.

3.3.2. 3D Crossed Beam Optical Dipole Trap

After the precooling stage in the magneto-optical trap, we transfer the sample into a crossed beam optical dipole trap (CBODT), where we then evaporatively cool it into the quantum degenerate regime. Figure 3.3 shows the beam path of the CBODT (red line). The focused beam intersects with its own reflection under an angle of 12 ° in the middle of the main chamber. In order to avoid interference effects, the polarization of the reflected beam is rotated by 90 ° with the help of a waveplate. To facilitate the transfer into a single layer of the quasi-2D standing wave trap (see chapter 3.3.3), we use elliptically focused beams for the CBODT. The foci of the beam have an aspect ratio of approximately $1:5.3$ which leads to a surfboard shaped trap with an aspect ratio of $1/\omega_x^{\text{CBODT}} : 1/\omega_y^{\text{CBODT}} : 1/\omega_z^{\text{CBODT}} \approx 8.3 : 44 : 1$, which we determine from the harmonic trapping frequencies ω_i^{CBODT} in the respective direction. To further optimize the transfer, we can modulate the trap position in horizontal and vertical direction with the help of two crossed AOMs in the beam path, and thus create a time-averaged potential. The transfer from the CBODT into the quasi-2D trap is described in chapter 4.2.

The 1068 nm laser beam is produced by an IPG Photonics YLR-200-LP Ytterbium fiber laser, which yields up to 200 W. During the transfer from the MOT into the CBODT, we use the full power of the laser, which leads to a trap depth of more than 1.5mK. This is deep enough to capture the precooled atoms which have a temperature of several 100 μK.

Directly after the transfer, we ramp the laser power down to 40 W to reduce thermal lensing. We then use the AOMs to attenuate the beam and thus further lower the trap depth during forced evaporation. We control the laser power with a feedback loop which controls the AOMs and regulates on the signal of two photodiodes. They are placed behind a dielectric mirror in the CBODT beam path and pick up the small fraction of the beam which is transmitted through the mirror. We use two photodiodes since we tune the laser power by approximately four orders of magnitude. One of them gets a small amount of the transmitted light and is used at high powers, whereas the other one gets more light and is used at low powers. Thus we avoid thermal effects on the photodiodes at high laser powers and extend the dynamic range of the setup while keeping the signal to noise ratio sufficiently high. More information on the crossed beam optical dipole trap can be found in [Boh12].

3.3.3. 2D Standing Wave Trap

In order to reach the quasi-2D regime, we transfer the quantum degenerate sample prepared in the CBODT into a single pancake shaped interference maximum of a standing-wave optical dipole trap (SWT).

The Quasi-2D Regime

The gas is in the quasi-2D regime when excitations in one dimension are frozen out. This can be achieved with the help of a strong confinement in this dimension which shifts the first excited state to an energy which is higher than the energy scale of the sample. For a quantum gas in a harmonic trap, this can be realized by a large aspect ratio $\omega_x, \omega_y \ll \omega_z$, where $\omega_{x,y,z}$ is the trapping frequency in the respective direction. The quasi-2D regime is entered when both $\mu < \hbar\omega_z$ and $k_B T < \hbar\omega_z$ are fulfilled, where μ is the chemical potential and $k_B T$ is the thermal energy of the gas. Figure 3.4 shows a quasi-2D ideal Fermi gas, where $\mu = E_F$, at zero temperature.

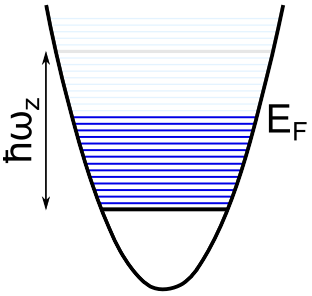

Figure 3.4.: Harmonically trapped Fermi gas at $T = 0$ in the quasi-2D regime in a radially symmetric trap. Occupied radial (axial) levels are depicted blue (black). Unoccupied levels are grayed out. The energy of the highest populated level is below that of the first axially excited level ($E_F < \hbar\omega_z$), and thus the system is kinematically two-dimensional.

In this limit, the atoms continuously fill up the trap levels starting from the lowest energy. The number of atoms which fit into the trap without populating the first excited z-level can thus be found by counting the trap levels. The criterion for a quasi-2D sample is

$$n_x \hbar\omega_x + n_y \hbar\omega_z < \hbar\omega_z \quad , \tag{3.3}$$

where $n_{x,y}$ is the number of populated levels in x and y direction, respectively. This leads to the maximum number of populated levels N_{crit}, which is at the same time the critical number of atoms per spin state:

$$N_{crit} = \frac{1}{2} n_{x,max} n_{y,max} = \frac{1}{2} \frac{\omega_z^2}{\omega_x \omega_y} \quad . \tag{3.4}$$

Although this calculation does not take into account finite temperatures, interactions, and anharmonicities, the observed strong dependence on the aspect ratio always holds. In order to realize a quasi-2D quantum gas in a trap, it is thus crucial to have a trap with the maximum feasible aspect ratio.

Experimental Realization

In our setup, we use the standing wave interference pattern of two intersecting laser beams as a trap for the quasi-2D gas. This approach has the advantage that it is possible to realize very large aspect ratios. However, there is also a disadvantage: the standing wave creates a whole stack of traps rather than just one. Thus, one has to make sure that tunneling between the layers is negligible. In addition, it is challenging to load the sample into just one of the layers, as will be discussed in chapter 4.2.

The standing wave trap (SWT) consists of two 1064 nm laser beams which intersect under an angle of approximately 14 ° in the vertical plane (green line in figure 3.3). They produce a vertical interference pattern with a wavelength of approximately 4.4 μm. At a typical trap depth of approximately 500 nK, the harmonic oscillator length in vertical direction is $\ell_z \approx 550\,\mathrm{nm}$, and tunneling between the layers is negligible. In order to achieve a round potential in the horizontal plane, we elliptically focus the beams with an aspect ratio of 1 : 8.[2] The waists in the focal plane are $w_0^{vert} \approx 75\,\mu\mathrm{m}$ and $w_0^{hor} \approx 600\,\mu\mathrm{m}$. This leads to harmonic trapping

---

[2] The ellipticity has two additional benefits: it reduces the total laser power at a given trap depth, and leads to bigger waists on the optics. This reduces thermal lensing effects.

frequencies of

$$\begin{aligned}\omega_x &= 2\pi(14.10 \pm 0.02)\mathrm{Hz}\\ \omega_y &= 2\pi(14.02 \pm 0.03)\mathrm{Hz}\\ \omega_z &= 2\pi(5.53 \pm 0.03)\mathrm{kHz}\end{aligned}$$

at a trap depth of approximately 500 nK, which is used for the presented experiments. The SWT thus has an aspect ratio of 392 : 394 : 1 and a cylindrical symmetry of 99.5%. According to equation (3.4), it should be possible to prepare samples of up to $N_{crit} \approx 77\,000$ atoms per spin state in the quasi-2D regime. However, this number is only a coarse estimate, since it neglects the effects of finite temperature, interactions, and anharmonicities in the radial potential. Additionally, the total radial trapping potential has a small contribution of an additional magnetic potential, which will be described in chapter 3.4. Thus, we have to measure N_{crit} to make sure our experiments are conducted in the quasi-2D limit. This measurement will be explained in chapter 4.3.

In order to obtain a good interferometric stability of the SWT, we carefully designed the mechanical setup. The elliptical beam is created by a cylindrical telescope and then focused by a $f = 900$ mm lens (see figure 3.3). It then enters the interferometer setup depicted in figure 3.5. There, it is split up by a non-polarizing 50 : 50 beam splitter cube and then reflected into the experiment chamber by two mirrors. The beam path is kept symmetric after the beam splitter to avoid drifts of the interference pattern due to changes in air pressure. A mount for a waveplate is included in the setup. With the help of a $\lambda/2$ waveplate, the polarization of the upper beam can be rotated by 90 °. Thus, the interference pattern can be removed from the intersection of the beams. This is useful for adjusting the height of the intersection to the position of the CBODT.

All components of the interferometer are mounted onto a solid 50 mm aluminum block for mechanical and thermal stability. The setup is further stabilized by the solid front and back covers. During our experiments, it is closed by an aluminum sheet lid (not shown in the figure) to reduce turbulent air flow. In addition, also the beams outside the interferometer are protected from air flow by aluminum tubes.

To measure the stability of the interference pattern under realistic conditions we loaded atoms into several pancakes and measured their axial position (method see chapter 4.2.1). The observed drift of the interference pattern was smaller than $0.5\,\mu$m which corresponds to a phase drift $< \lambda/8$ over 6 days. Thus, the passive stability is sufficient and no active stabilization is necessary.

The light for the SWT is provided by a 50 W Nufern SUB-1174-22 fiber amplifier

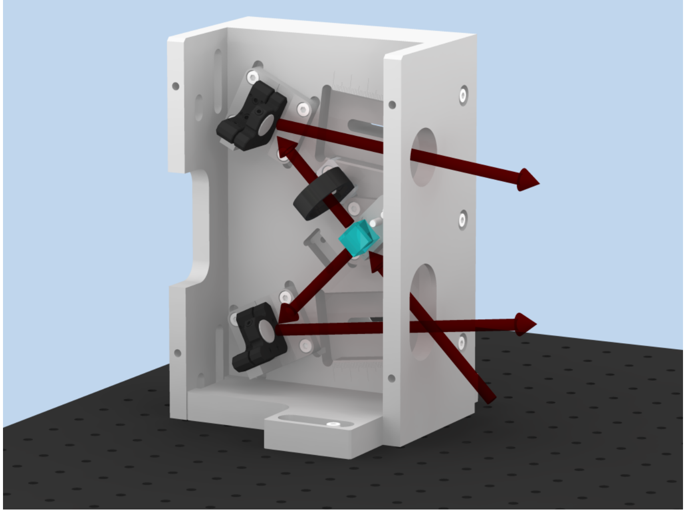

Figure 3.5.: Mechanical setup of the standing wave trap interferometer. The focused laser beam (dark red) enters the interferometer setup under an angle of 45 ° from the front. It is split up by a non-polarizing 1/2 inch beam splitter cube. The two resulting beams are reflected into the chamber under an angle of ±7 ° by two 1/2 inch mirrors. There is a mount for an optional waveplate in the upper beam path, which can be used to rotate the polarization and turn off the interference pattern. Taken from [Wen13].

which is seeded by an Innolight Mephisto-S 500 NE solid state laser at 1064 nm. As in the case of the CBODT, the power is regulated with an AOM controlled by a feedback loop. It is then coupled into a OZ optics high power fiber to transfer it to the breadboard at the experiment chamber. For the trap depth of approximately 500 nK used in our experiments, we use approximately 3 W after the fiber.

More details about the design of the interferometer can be found in [Boh12]. The setup and performance of the SWT are described in detail in [Nei13].

3.3.4. Optical Lattice

For future experiments, we already set up a 2D optical lattice in our apparatus. Until now, it was only used to calibrate the imaging magnification by Kapitza-Dirac diffraction [Kap33, Fre01] of atoms on the lattice potential (see chapter 3.5).

The optical lattice consists of two separate 1D lattices which intersect under an angle of 90 °. The optical setup is shown in figure 3.3 (yellow beam path).

Unlike in most other optical lattice setups, the beams are not retroreflected but intersect with their own reflection under a small angle of approximately 12 °. This is necessary for the high required laser power of several Watts. A retroreflected beam would hit the fiber with which the light is transferred to the main breadboard and could melt the fiber tip due to its high power.

The light is provided by the Nufern fiber amplifier also used for the SWT and has a wavelength of 1064 nm. Together with the angle of the lattice beams, this leads to a lattice spacing of 536 nm. As in the other optical dipole traps, the intensity can be tuned with an AOM and is controlled by a feedback loop which uses the signal of a photodiode behind a mirror in the beam path.

In order to avoid interference between the two lattice axes, their polarizations are rotated by 90 ° with respect to each other. The polarization of lattice beam 2 is horizontal and thus the same as that of the SWT. To avoid interference here, the frequencies of the two beams are detuned from each other by 200 MHz with the help of the intensity control AOMs.

More information about the lattice setup can be found in [Bec13].

3.4. Magnetic Fields

Magnetic fields are an important tool to manipulate our sample. They have two important effects on the ultracold gas:

- As described in chapter 2.2.2, the scattering length a and thus the interparticle interaction strength in the gas can be tuned with the help of a magnetic Feshbach resonance. We do this by applying a homogeneous magnetic offset field. At the same time, this field also sets the quantization axis to the vertical z-direction.
- Due to their magnetic moment μ, atoms in a magnetic field B along the quantization axis experience a magnetic potential $U_{mag}(\mathbf{r}) = -\mu B_z(\mathbf{r})$. Magnetic field gradients thus result in a force on the atoms.

We can apply magnetic offset fields and gradients with two pairs of coils in our setup, the offset field coils (green in figure 3.1) and the MOT coils (blue in figure 3.1). Both coil pairs have an (anti-) Helmholtz geometry along the vertical axis of the main chamber.

3.4.1. Offset Field Coils

The offset field coils consist of 30 windings of 0.5×7.5 mm Kapton coated wire with an average radius of 44 mm. They are mounted in the reentrant vertical viewports of the main chamber in an approximate Helmholtz configuration (green in figure 3.1). To avoid overheating, the coils are glued onto custom-designed water cooled copper heat sinks. For a better heat conductance between the coil and the heat sink, we removed the Kapton coating on one side of the coil with a lathe, and glued the resulting flat surface onto the heat sink with a thermally conducting but electrically insulating diamond filled epoxy [Zür09].

The coils can provide a homogeneous magnetic field up to $B = 1500\,\mathrm{G}$ at the position of the trapped sample at a current of 220 A. This allows us to use the broad Feshbach resonance between state $|1\rangle$ and $|2\rangle$ at $B_0 = 832.2\,\mathrm{G}$ (see figure 2.3). The inductance of the coils allows for a maximum ramping speed of $dB/dt \approx -2.4\,\mathrm{G}/\mu\mathrm{s}$, which can be achieved by suddenly switching the current off.

Since the coils are mounted slightly further apart than Helmholtz configuration, the magnetic field has a saddle point. A simulation of the axial magnetic field is shown in figure 3.6. In axial direction, the field has its maxima approximately 10 mm above and below the center. For the highfield seeking atoms, this leads to a weak anti-confining potential along the axial direction. It is on the order of $2\pi \times 20\,\mathrm{Hz}$ and thus negligible compared to the confinement of the SWT, $\omega_z \approx 2\pi \times 5.5\,\mathrm{kHz}$.

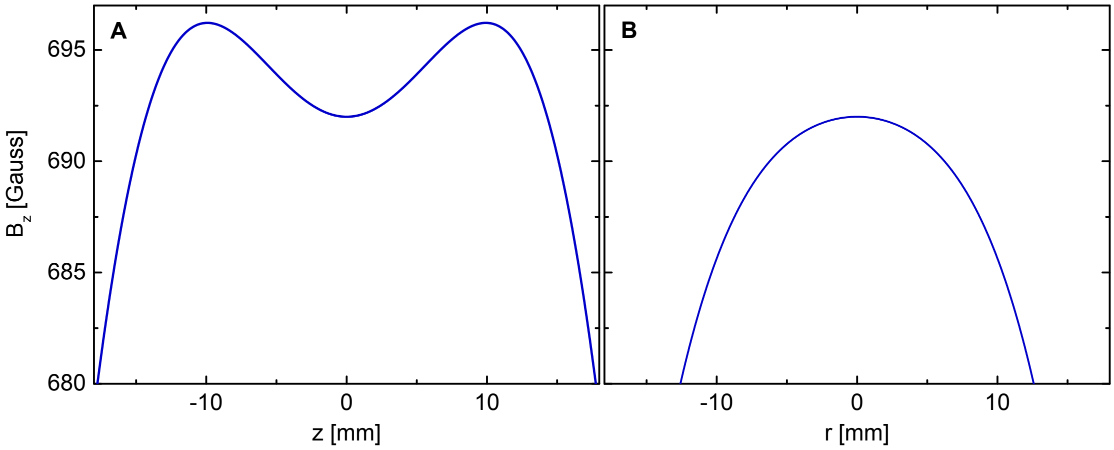

Figure 3.6.: Offset field in axial direction as a function of axial (A) and radial (B) position. The data is obtained from a numerical simulation of our offset field coils at an offset field of $B = 692\,\mathrm{G}$. Due to the imperfect Helmholtz configuration of the coils, the magnetic field has a saddle point. For our highfield-seeking atoms, it acts as an anti-confining (confining) potential in axial (radial) direction.

In radial direction, the saddle leads to a weak confining potential which is almost perfectly harmonic even for large radii of several mm. We measured its trapping frequency to be $\omega_{r,\mathrm{mag}} \approx 0.39\,\mathrm{Hz}\sqrt{B[G]}$, which corresponds to $2\pi \times (10.2 \pm 0.03)$ Hz at $B = 700\,\mathrm{G}$. This radial confinement has two desired effects: it improves the cylindrical symmetry of the standing wave trap, and enables us to perform a matter wave focusing technique. This technique allows us to measure the radial momentum distribution of our gas and will be described in chapter 4.6. In order to make use of the radial magnetic confinement and to minimize vertical forces on the sample, we carefully align the optical dipole traps to the magnetic saddle point.

The combined trapping frequencies of the SWT and the magnetic saddle point potential are

$$\begin{aligned}\omega_x &= 2\pi(17.40 \pm 0.06)\mathrm{Hz}\\ \omega_y &= 2\pi(17.34 \pm 0.06)\mathrm{Hz}\\ \omega_z &= 2\pi(5.53 \pm 0.03)\mathrm{kHz}\end{aligned}$$

at $B = 700\,\mathrm{G}$ and a trap depth of approximately 500 nK.

We control the current in the offset field coils by a digital PID feedback loop which measures the current with a current transducer. When the field has to be constant with a high precision, we use an amplifier circuit to enhance the precision of the 16 bit input of the controller. A differential amplifier amplifies the difference between the signal from the current transducer and a high precision reference voltage. The result is then used to obtain the error signal for the PID loop. This enables us to obtain a magnetic field stability of approximately 1 mG at an offset field of $B = 800\,\mathrm{G}$. This corresponds to a relative stability of $1.25 \cdot 10^{-6}$. More information on the magnetic field stabilization can be found in [Pre14].

By inverting the current through the upper coil with the help of an H-Bridge circuit, we can change the configuration of the offset field coils to an anti-Helmholtz configuration. Thus, we can also use them to create magnetic field gradients. This is useful during the transfer from the MOT to the CBODT: The zero point of the anti-Helmholtz MOT field is slightly displaced from the saddle point of the offset field coils, to which the CBODT is adjusted. Shortly before the transfer, we thus turn the MOT coils off and create the anti-Helmholtz field with the offset field coils instead. In this way, we shift the zero point of the MOT field and thus the trapped atoms to the position of the CBODT.

3.4.2. MOT Coils

The MOT coils consist of four axially stacked layers of 25 windings of 1×5 mm Kapton coated wire. They are mounted on the top and bottom of the main chamber (blue in figure 3.1) in an approximate anti-Helmholtz configuration and have water cooled copper heat sinks. They can provide magnetic field gradients up to approximately 85 G/cm at 70 A. By inverting the current, we can also invert the direction of the magnetic field gradient. During the different phases of the experimental sequence, we use the gradient for the magneto-optical trap, to compensate gravity, to pull atoms up or down, and for the tomographic measurement described in chapter 4.2.1.

Similar to the current in the offset field coils, we measure the current through the MOT coils with a current transducer and use it as an error signal for a digital PID feedback loop. This allows us to stabilize the gradient to a relative precision of approximately 10^{-3}.

3.5. Absorption Imaging

To obtain information about our sample, we rely on absorption imaging. In this method, a pulse of resonant light is shined on the atom cloud and its shadow is recorded on a camera.

In our setup, we are able to perform absorption imaging in all four optical axes of the main chamber. The imaging beams (dark gray) and the corresponding optics and cameras are shown in figure 3.3. For the experiments presented here, we mainly use the vertical imaging axis, which images the radial plane of the quasi-2D sample. For the tomographic measurement of the atom distribution over the layers of the SWT (see chapter 4.2) and the measurement of the axial momentum of the sample (see chapter 4.3), we use the horizontal axis of lattice beam 1.

In both axes, we use AVT Stingray F-145B FireWire cameras. They have a monochrome chip with 1388 × 1038 6.45 μm square pixels, a dynamic range of 14 bit, and a specified quantum efficiency of approximately 44 % at the used wavelength of 671 nm. In both axes, we obtain a magnification of approximately 2 with the help of telescopes in the imaging axis ($\mathrm{mag}_{vert} = 1.98 \pm 0.12$, $\mathrm{mag}_{hor} = 2.04 \pm 0.01$).

We calibrate the magnification by means of Kapitza-Dirac diffraction [Kap33, Fre01] of atoms on the lattice potential. Similar to light diffracted on a grating, the atoms absorb momenta which are integer units of the lattice wave vector k_{lat}. By measuring their position after a defined time-of-flight, we can obtain their momentum distribution and thus k_{lat}. Since we know the lattice spacing (see chapter 3.3.4), we can thus calibrate the imaging magnification. The calibration procedure is described in [Bec13].

The imaging beam is provided by a Toptica DL Pro laser which is beat-offset locked to the same 671 nm ^{6}Li D2 transition spectroscopy setup as the MOT laser. As the transition frequency tunes with the magnetic offset field B, we tune the offset to adjust the laser frequency for the respective field. By quickly switching the beam on and off with an an AOM, we create imaging pulses with durations of approximately 10 μs.

4. Creating and Probing a 2D Fermi Gas

This chapter explains how we create and probe a quasi-2D Fermi Gas of ultracold atoms in the strongly interacting limit. Parts of its content have been published in [Mur14b, Rie14].

The chapter starts by describing the creation of a molecular BEC, which is the basis for all described experiments. In the next step, we are able to transfer the molecular BEC into a single layer of the large aspect ratio standing wave trap (SWT). The necessary techniques are described in chapter 4.2. In addition, the tomographic measurement technique we developed to obtain the distribution of the sample over the layers of the SWT is introduced. After the transfer, we ensure that the sample reaches the quasi-2D regime by probing its axial momentum distribution and adjusting the number of atoms. This is described in chapter 4.3. The final step of the preparation is the tuning of the interaction strength and temperature, which enables us to map out the phase diagram of the system. It is described in chapter 4.4.

We probe the sample by means of absorption imaging. Chapter 4.5 describes the careful calibration of the imaging parameters which is necessary in order to extract quantitative information. In addition to the in-situ density distribution of the sample, we also measure its pair momentum distribution. For this, we use a matter-wave focusing technique, which is described and characterized in chapter 4.6.

4.1. The Starting Point: Creation of a Molecular BEC

The starting point for our experiments is always a Bose-Einstein Condensate (BEC) of molecules, which we create in the crossed beam optical dipole trap (CBODT) described in chapter 3.3. Figure 4.1 shows a simplified sketch of the experimental sequence.

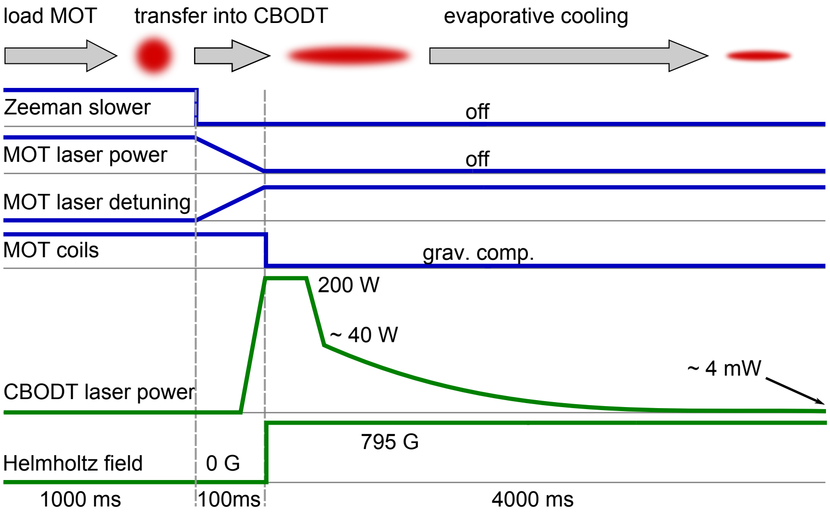

Figure 4.1.: Preparation of a molecular BEC. The sequence can be divided into three phases: loading of the MOT, transferring the atoms into the CBODT, and evaporative cooling in the CBODT. Only the most important experimental parameters are shown and the sketch is not to scale. Adapted from [Nei13].

In the first phase, we load the MOT for approximately 1 s.[1] During this time, the Zeeman slower light and magnetic field are on. The MOT beams are running on maximum power at a large red-detuning of approximately -40 MHz. This leads to a large capture radius as well as a low atom density in the MOT, which reduces the rate of two-body losses. The MOT-coils provide the anti-Helmholtz MOT field with a gradient of approximately 30 G/cm. We thus obtain a gas of approximately 10^8 atoms at a temperature of a few 100 μK.

In the subsequent phase, we transfer the precooled atoms into the CBODT. At the beginning of this phase, we turn the Zeeman slower off. To compress the MOT, we reduce the detuning to a few MHz, while at the same time reducing the laser power to minimize photon scattering and thus the temperature. When the MOT is sufficiently compressed, we turn on the CBODT at its maximum depth, which is more than 1.5 mK. We then turn off the MOT beams and the MOT field. By turning the repumper fraction of the MOT beams off a few milliseconds faster than the cooler fraction, we pump all atoms in the $F = 1/2$ hyperfine state of the $2\,^2S_{1/2}$ ground state. In the presence of a magnetic offset field, we thus obtain a mixture of atoms in the Zeeman sublevels $|1\rangle$ and $|2\rangle$.

---

[1] Depending on the life cycle of the MOT laser tapered amplifier chip and thus the available laser power, we load the MOT for up to 3 s.

After the transfer, we evaporatively cool the gas into quantum degeneracy in the CBODT. We compensate gravity by applying a small gradient with the MOT coils and apply a magnetic offset field of $B = 795\,\mathrm{G}$. Then we perform forced evaporative cooling [Met02] by continuously decreasing the CBODT laser power and thus the trap depth. The magnetic offset field leads to a strongly repulsive mean field interaction and thus a fast thermalization. At sufficiently low temperatures, the atoms form diatomic molecules. At even lower temperatures, these molecules condense into a molecular BEC.

At the end of the evaporation ramp, we thus obtain a practically pure BEC of approximately 100 000 diatomic molecules consisting of atoms in states $|1\rangle$ and $|2\rangle$ at a temperature of some $10\,\mathrm{nK}$. The preparation sequence takes approximately $5\,\mathrm{s}$, which allows for large repetition rates of our experiments.

4.2. Loading a Single Layer

In the next step, we transfer the sample into the standing wave trap (SWT) described in chapter 3.3.3. For our experiments, it is crucial to transfer the gas into one single layer, and to minimize the fraction in the neighboring layers. This is challenging due to the small distance between the layers.

It is impossible to optically resolve atoms in the individual layers with the help of Gaussian beam optics. This is due to the combination of their small distance of $4.4\,\mu\mathrm{m}$ with their radial extension of approximately $200\,\mu\mathrm{m}$. The depth of focus as a function of the resolution in the focal plane w_0 is on the order of the Rayleigh range $z_R = \pi w_0^2/\lambda$. For our wavelength $\lambda \approx 671\,\mathrm{nm}$ and a resolution of $2\,\mu\mathrm{m}$, the depth of focus is on the order of $z_R \approx 20\,\mu\mathrm{m}$, which is an order of magnitude too small compared to the extension of the sample.

In order to measure the distribution of the atoms over the SWT layers, we thus developed a tomographic measurement which is described below. With this diagnostic tool at hand, we were able to optimize the transfer and thus load more than 89 % of the sample into a single layer, which is sufficient for our experiments. The transfer is described after the tomographic measurement in chapter 4.2.2.

4.2.1. RF-Tomography

For the tomographic measurement of the atom distribution over the SWT layers, we utilize the transition into the third Zeeman sublevel labeled $|3\rangle$ (see figure 2.2). Atoms can be transferred from state $|2\rangle$ to $|3\rangle$ by the application of a radio-frequency (RF) pulse. The transition frequency $\nu_{|2\rangle|3\rangle}$ depends on the magnetic offset field [Bre31]. We make $\nu_{|2\rangle|3\rangle}$ dependent on the axial coordinate z by applying a magnetic field gradient along this axis. We then drive the RF transition and measure the number and position of the transferred atoms with state selective absorption imaging. Scanning $\nu_{|2\rangle|3\rangle}$ then enables us to resolve the individual layers. Figure 4.2 visualizes the concept of a single measurement.

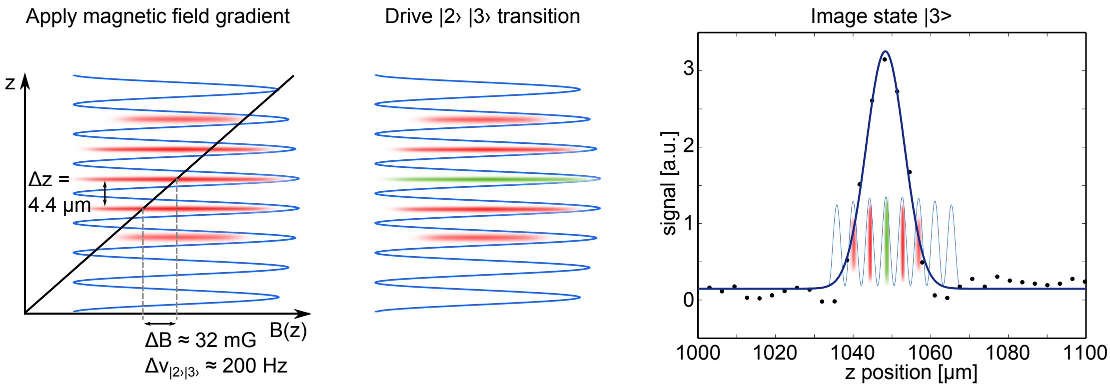

Figure 4.2.: Conceptual sketch of the tomographic measurement. The transition frequency $\nu_{|2\rangle|3\rangle}$ between states $|2\rangle$ and $|3\rangle$ is made position dependent by the application of a magnetic field gradient. Then, the $|2\rangle \rightarrow |3\rangle$ transition is driven. Fitting the obtained density distribution of atoms in state $|3\rangle$ with a Gaussian allows to determine the atom number and their position. Adapted from [Nei13].

For the tomographic measurement, we first transfer a molecular BEC consisting of atoms in states $|1\rangle$ and $|2\rangle$ from the CBODT into the SWT. We do this by ramping the depth of the SWT to approximately 500 nK over approximately 500 ms and simultaneously ramping the CBODT off. To exclude interaction effects, we remove all atoms in state $|1\rangle$ from the sample with the help of an imaging pulse resonant with these atoms. To minimize interactions between atoms during this process, we first ramp the magnetic offset field to $B = 1000\,\mathrm{G}$, where the sample consists of weakly interacting unbound atoms at our temperatures. We still observe heating of the remaining atoms, but it is small compared to the trap depth and therefore should not change the distribution over the layers.

We then apply a strong additional magnetic field gradient of approximately 70 G/cm along the z-axis with the MOT coils and drive the transition to state $|3\rangle$. To ensure that not too many atoms are lost due to the gradient, we have to increase the depth of the SWT to the maximum feasible value,[2] which is approximately

---

[2] This trap depth corresponds to the largest laser power which we can currently transmit through the high-power optical fiber (see chapter 3.3.3) without dropping to a coupling efficiency below 60 % at any point during the necessary several 100 repetitions of the measurement. At lower

$1\,\mu$K.

Subsequently, we take a state-selective absorption image of the transferred atoms along the horizontal imaging axis. By recording the number of transferred atoms as a function of $\nu_{|2\rangle|3\rangle}$, we can thus measure the distribution of atoms between the layers. Figure 4.5 in chapter 4.2.2 shows the result of such a measurement.

The tomographic measurement of the atom distribution over the SWT is described in detail in [Nei13].

Magnetic Field Stability and Frequency Resolution

At the offset field used for the tomographic measurement, the transition frequency is $\nu_{|2\rangle|3\rangle} \approx 80.959\,\mathrm{MHz}$ with a magnetic field dependence of $d\nu_{|2\rangle|3\rangle}/dB \approx 6.3\,\mathrm{Hz/mG}$ [Bre31]. With the gradient, this leads to a spatial dependence of $d\nu_{|2\rangle|3\rangle}/dz \approx 45\,\mathrm{Hz}/\mu\mathrm{m}$. This corresponds to a splitting of $\Delta\nu_{|2\rangle|3\rangle} \approx 200\,\mathrm{Hz}$ between the SWT layers.

To achieve a good signal-to-noise ratio in the tomographic measurement, we average over several individual frequency scans. To avoid frequency shifts during the measurement, we thus have to keep the total magnetic field constant to a high precision during the measuring time. We therefore use the differential offset amplifier circuit described in chapter 3.4.1 for the offset field, which leads to a long-term stability of approximately $1\,\mathrm{mG}$. The long-term stability of the gradient is approximately 10^{-3} (see chapter 3.4.2), which leads to a stability better than $0.01\,\mathrm{mG}/\mu\mathrm{m}$. The total long-term magnetic field stability is thus slightly worse than $1\,\mathrm{mG}$ in the vicinity of the magnetic saddle point, which leads to a long-term frequency stability of approximately $10\,\mathrm{Hz}$.

The frequency resolution is determined by the width of the RF transition, which we experimentally determine to be approximately $80\,\mathrm{Hz}$. It is influenced by magnetic field inhomogeneities over the sample and by short-term fluctuations of the magnetic field. By choosing a sufficiently long pulse time for the RF pulse ($20\,\mathrm{ms}$), we make sure that it is not Fourier limited.

4.2.2. Optimizing the Transfer

With the above described tomographic method as a diagnostic tool, we were able to optimize the transfer of the sample from the CBODT to the SWT. There are three main quantities which influence the transfer efficiency, i.e. the fraction of atoms that can be transferred into the central layer: the aspect ratio of the CBODT, the

---

coupling efficiencies, the fraction of the light which is not transmitted might heat and damage the fiber tip.

vertical extension of the sample, and the relative position of the CBODT and the central SWT layer.

The aspect ratio of the CBODT is approximately $8.3 : 44 : 1$ (see chapter 3.3), whereas that of an SWT layer is approximately $392 : 394 : 1$ (see chapter 3.3). This leads to a bad overlap of the traps both in vertical and horizontal direction. In the vertical z-direction, the sample in the CBODT is too wide to fit into a single layer of the SWT. In the horizontal plane, the CBODT is elliptical with an aspect ratio of $8.3 : 44 \approx 5.3$, whereas the SWT is almost perfectly circular. During the transfer, the sample thus expands in the x-direction, which can lead to the excitation of a breathing mode and thus heating of the sample.

To resolve these two issues, we use the horizontal AOM in the CBODT beam path to create a time-averaged potential for the atoms [Fri00, Rud01]. By modulating the frequency and thus the diffraction angle of the AOM, we scan the x-position of the CBODT. The AOM operates at a frequency of $\nu_{\mathrm{AOM}} \approx 110\,\mathrm{MHz}$, which we modulate with a frequency of $\nu_{\mathrm{mod}} = 100\,\mathrm{kHz}$. The shape of the modulation function is triangular, and its amplitude corresponds to $15\,\mathrm{MHz}$. Since ν_{mod} is substantially greater than all involved trapping frequencies, the atoms experience a quasi-static time-averaged potential. We optimized frequency, amplitude and functional shape of the modulation function for an optimum roundness of the time-averaged potential.

The influence of the modulation on the shape of the CBODT can be seen in figure 4.3, which shows the shape of the original CBODT (A), the modulated CBODT (B), and the SWT (C) in the horizontal plane. Due to the modulation, the aspect ratio in the horizontal plane is reduced to approximately 1.5. The modulated CBODT thus overlaps a lot better with the similarly sized circular SWT. Note that due to the anharmonicity of the modulated trap, it is impossible to measure trapping frequencies to determine the aspect ratio. The given number is extracted from the width of a Gaussian fit to the data.

Since we cannot image the sample in the horizontal direction with sufficient resolution, it is difficult to make a quantitative statement about the vertical extension of the sample in the modulated trap. However, both the shape in the horizontal plane and the column density, which is reduced by a factor of 5, indicate a significant reduction of the vertical extension. This is further confirmed by the increased transfer efficiency.

The vertical extension of the sample can trivially be further reduced by decreasing the particle number. However, for a given atom number we can still make the sample smaller by compressing it. We thus slowly increase the trap depth by a factor of 90 after the evaporation.

Another crucial factor in the size of the sample is its quantum statistics. A Fermi gas will occupy energy levels up to the Fermi energy E_F, which corresponds to the

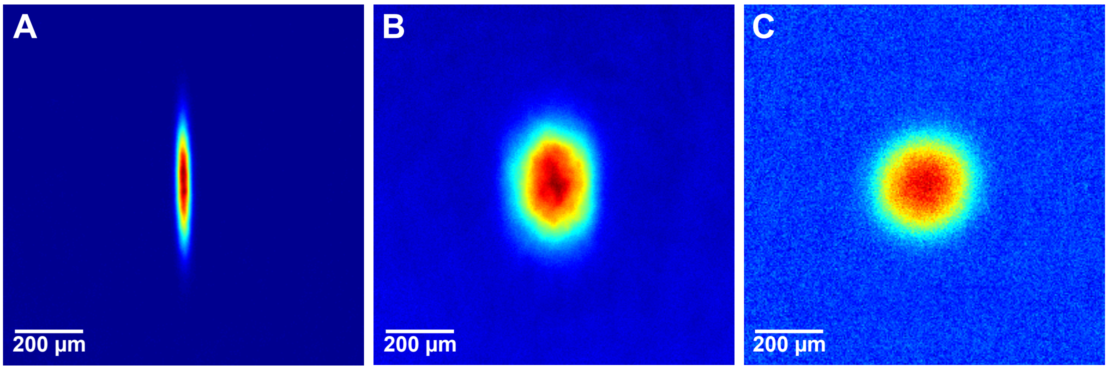

Figure 4.3.: A molecular BEC at 795 G in the CBODT (A), the modulated CBODT (B), and the SWT (C) viewed in the vertical axis. Due to the modulation, the spatial overlap in the horizontal plane between the CBODT and the SWT becomes significantly better. At the same time, the vertical extension of the sample becomes smaller which facilitates the transfer into a single layer.
The color scale denotes the column atom density. Note that it is different for each image. The column density in (A) is approximately 5 times larger than in (B) and (C). Each image is the average of approximately 80 (A), 170 (B), and 30 (C) realizations.

Fermi radius $r_F = \sqrt{\frac{2E_F}{m\omega^2}}$ in a harmonic trap with trapping frequency ω. A Bose gas, on the other hand, has no degeneracy pressure and will thus be denser and smaller at the same temperature. It is therefore important to transfer a molecular BEC instead of a Fermi gas. Additionally, repulsive interactions in the sample will lead to a higher mean energy and thus to a larger extension.

We thus transfer a molecular BEC at the lowest attainable temperature at a magnetic offset field of 730 G, where $a \approx 2500 a_0$. Here, the repulsive interactions are more than a factor of 3 weaker than at 795 G, where we perform the evaporation, but the gas is still stable.

The relative position between the CBODT and the central layer of the SWT determines whether we load the sample into just one layer, or split it up between two adjacent layers. We adjust the vertical position of the atoms in the CBODT to the central SWT layer by pulling them up or down with a magnetic field gradient during the transfer. To apply the gradient, we use the MOT coils. Using gradients up to ±6 G/cm, we can move the sample by approximately one layer without significant heating or loss of atoms.

Paying attention to these three points, we optimized the transfer sequence. A sketch of the sequence is shown and described in figure 4.4.

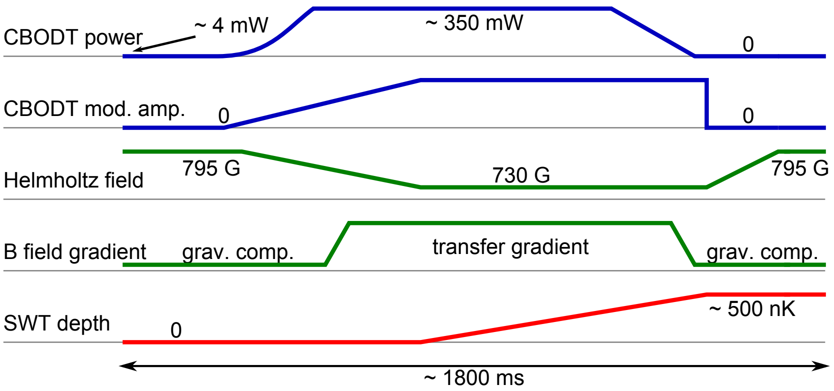

Figure 4.4.: Sketch of the experimental sequence during the transfer. We ramp up the CBODT power to compress the sample while simultaneously ramping on the modulation for the time-averaged potential. At the same time, we adiabatically decrease the magnetic offset field to 730 G to reduce the repulsive mean-field interaction and thus the size of the sample. We adjust the position of the atoms to an interference maximum of the SWT by applying a magnetic field gradient with the MOT coils, which shifts the atoms up or down. Then, we adiabatically ramp on the SWT until we reach its final depth of approximately 500 nK, while simultaneously ramping the CBODT off. After the transfer, we return to an offset field of 795 G and a magnetic field gradient which compensates gravity.

With the help of the optimized transfer sequence, we can load at least approximately 89 % of our BEC of approximately 100 000 molecules into a single layer of the SWT. Figure 4.5 shows the distribution over the layers obtained by means of the above described tomographic measurement. The data points show the number of atoms transferred to state $|3\rangle$ as a function of the transition frequency, which corresponds to the z-position. One can clearly observe the central layer at $\nu_{|2\rangle|3\rangle} \approx 80.9591\,\mathrm{MHz}$. The small maxima at approximately 81.9589 MHz and 81.9593 MHz correspond to the neighboring layers. By fitting the distribution with the sum of three Gaussian profiles of the same width and distance, we estimate the fraction of the sample in the non-central peaks to be 11 %.

However, we think that this number overestimates the fraction of the sample in the non-central layers. During the tomographic measurement, we apply a large magnetic field gradient. This leads to a tilt of the trapping potential, and to the loss of approximately 25 % of the atoms. Since the filling of the central layer is much higher than that of its neighbors at a very similar trap depth, we assume

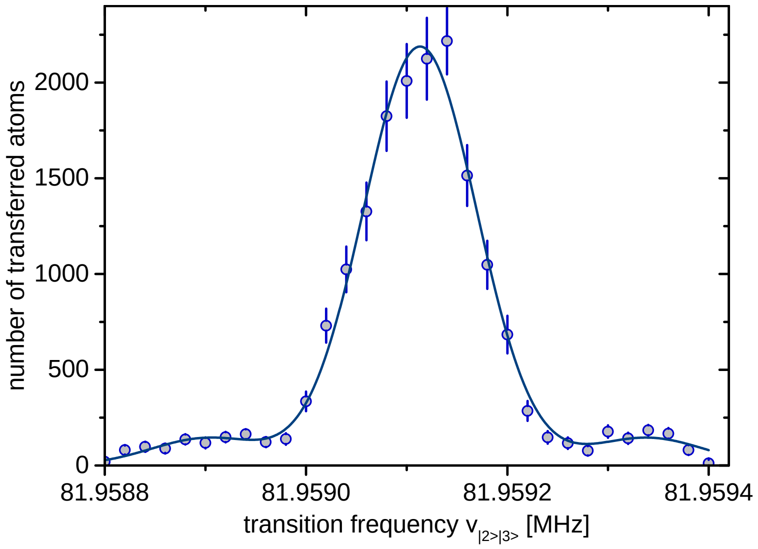

Figure 4.5.: Tomographic measurement of the atom distribution over the SWT layers. The data points represent the number of atoms transferred into state $|3\rangle$ as a function of transition frequency and thus position in z-direction. To avoid broadening, we drive the transition with a low intensity, which leads to a small transferred atom number. The central layer at $\nu^c_{|2\rangle|3\rangle} \approx 80.9591\,\mathrm{MHz}$ as well as its two neighbors at $\nu^c_{|2\rangle|3\rangle} \pm 200\,\mathrm{Hz}$ are shown. The solid line is the sum of three Gaussian profiles of the same width and distance, which is fitted to the data. From the fit, we obtain a fraction of 89 % of the sample in the central peak.

that a greater fraction is lost from the central layer than from the non-central ones. Additionally, the raw signal in the non-central layers is close to the detection limit, which leads to false-positive results when an atom density is fitted to the noise.

Due to the small number of atoms in the non-central layers, their phase space density is low and their distribution should hence be thermal. Under this assumption, we estimate their influence on the measured Fermi temperatures to be on the order of a few percent. The measured temperature and condensate fraction should not be affected. A detailed analysis of all systematic uncertainties can be found in chapter A.3 in the appendix.

4.3. Entering the Quasi-2D Regime

After transferring our sample into a single layer of the standing wave trap (SWT), we have to make sure that the sample is in the quasi-2D regime. In this regime, excitations in axial direction are frozen out, i.e. $\mu, k_B T < \hbar\omega_z$, and the system can be described by 2D theory [Pet00, Mar10]. For a sufficiently cold sample, the quasi-2D regime can be reached by keeping the number of particles below the critical number N_{crit}, at which the first axially excited level becomes populated (see chapter 3.3.3). This chapter explains how we control the particle number, and how we measure whether the sample is quasi-2D.

In our experiments, we always transfer the same number of particles (i.e. 100 000 diatomic molecules) into the SWT. Only then, we spill unwanted atoms and thus set the atom number for the experiment. Although it makes the transfer slightly more complicated, this has an important advantage: after being heated during the transfer, the sample is cooled again by the spilling process, which at the same time acts as forced evaporative cooling. Thus, we can access significantly colder temperatures.

We spill the spare atoms by lowering the depth of the SWT from approximately 500 nK to approximately 350 nK and simultaneously applying a strong magnetic field gradient of approximately 35 G/cm along the z-axis. Thus, atoms leaving the central layer are quickly pulled away rather than populating the empty non-central layers.

To find out whether excitations in axial direction are frozen out, we measure the axial momentum distribution of the sample in time-of-flight, similar to the measurement described in [Dyk11]. We ramp the sample across the BEC-BCS crossover to 1400 G into the weakly interacting Fermi regime. There, we suddenly turn off the SWT and let the sample evolve for 3 ms. Then we measure its axial extension by fitting the obtained axial momentum distribution with a Gaussian. By tuning the trap depth during the spilling process, we can tune the atom number. We thus obtain the axial extension after time-of-flight as a function of the atom number as shown in figure 4.6.

In the non-interacting limit, an atom in the axial ground state can be described by a Gaussian wave function. The evolution of each of these wave functions is then described by Gaussian dispersion. In particular, one expects the width of the density distribution after the time-of-flight to be constant with respect to the atom number. The width of the dispersing density distribution as a function of time can be found by performing a time evolution of the original Gaussian wave packet [Abe04]. A detailed derivation can also be found in [Pre14]. In our case,

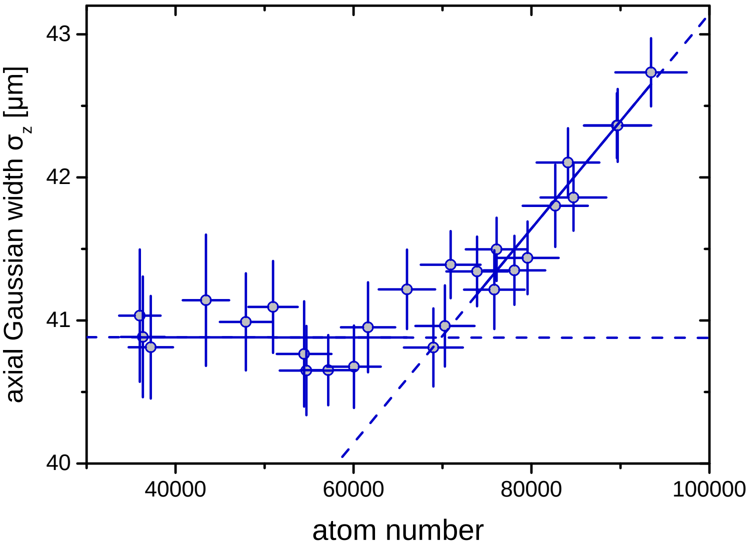

Figure 4.6.: Axial Gaussian width of the gas after 3 ms time-of-flight. Two regimes can be distinguished: for $N < N_{crit}$, all atoms are in the axial ground state of the trap. The obtained width after time-of-flight is thus independent of the atom number. For $N \geq N_{crit}$, the first axially excited trap level becomes available. Its population and thus the fraction of axially excited atoms grows with atom number, which leads to an increase of the effective Gaussian width after time-of-flight. We linearly fit both regimes, and determine $N_{crit} \approx 69\,000$ from the intersection of the fits. Each data point is the average of several individual measurements, error bars denote the standard error of the mean (SEM). The solid part of the linear fits indicates the fit range.

the Gaussian width σ_z is given as

$$\sigma_z = \sqrt{\frac{\hbar}{2m_{Li}}\left(\frac{1}{\omega_z} + \omega_z t^2\right)} \underset{t=3\,ms}{\approx} 42.2\,\mu\text{m} \quad . \tag{4.1}$$

In our measurement, we obtain a plateau at $\sigma_z \approx 40.9\,\mu$m for low atom numbers. This is a clear signature for the absence of axial excitations. We attribute the deviation of the measured Gaussian width from the theoretical value to the weak attractive interactions in the sample.

When the atom number is increased, the first axially excited trap level becomes populated. Atoms in this level have additional momentum in the axial direction. As their number grows, their contribution to the distribution after time-of-flight becomes more important. Thus, the fitted Gaussian width of the distribution increases with atom number.

Both the plateau and the increase in σ_z in figure 4.6 are well described by a linear behavior. We can thus extract the critical atom number N_{crit}, where atoms begin to populate the first axially excited level, from the intersection of linear fits to the two regimes. This yields $N_{crit} \approx 69\,000$. For our measurements, we thus keep the atom number below 65 000 atoms per spin state. While being large enough for a good signal-to-noise ratio, this atom number is smaller than N_{crit}, and we should thus obtain a quasi-2D sample.

The described measurement is only possible in the weakly interacting fermionic limit since stronger interactions and the formation of a BEC inhibit the independent evolution of the atoms in time-of-flight. Thus, we cannot repeat the measurement for the other interaction strengths where we take data. Still, the measurement at 1400 G gives a valid upper bound for the occupation of axially excited states: all other measurements are performed closer to the BEC limit, where the atoms occupy lower energy states due to their interactions and the formation of molecules.

However, to map out the phase diagram of the system we also have to access higher temperatures. They blur out the kink which we use to determine N_{crit} and thus make the described measurement unfeasible. At the same time, the number of axially excited atoms grows with T. Although the axial trap frequency corresponds to a temperature of $T_{\omega_z} = \hbar\omega_z/k_B \approx 265\,\mathrm{nK}$ which is higher than the highest temperatures we use, the combination of thermal energy and a large number of atoms occupying low energy states can lead to the population of axially excited states. It is thus important to have a measure for the amount of axial excitations at higher temperatures.

We obtain a measure for the fraction of excited atoms from the radial extension of each sample. For this, we assume a constant trap shape and the equal occupation of all motional degrees of freedom in the sample. The Fermi radius r_F^{1400G} of the sample at 1400 G with the critical atom number N_{crit} then represents the threshold for occupation of axially excited trap levels. Only atoms outside r_F^{1400G} have sufficiently high energies to occupy the axially excited level. We can thus get an estimate for the fraction of atoms with sufficient energy to populate an axially excited state for all magnetic fields and temperatures. For this, we integrate the atom density outside r_F and normalize it to the whole sample. Since the radial plane consists of two spatial dimensions and we assume equipartition, we have to divide this number by 2 to obtain the fraction of atoms in an axially excited state.

As expected, the number of axial excitations is negligible for the lowest investigated temperatures. For $T/T_F \leq 0.2$, the excited fraction is smaller than 1 % for all investigated interaction strengths. Only for the hottest samples on the Fermi side of the resonance ($T/T_F \gtrsim 0.3$, $\ln(k_F a_{2D}) > 3$) it becomes greater than 1.5 %.

This estimation does not take into account that the radially confining potential of the magnetic saddle point becomes weaker with decreasing magnetic offset field. At the lowest investigated offset field (692 G), the total radial trapping frequency is thus approximately 16 % smaller than at 1400 G, where the reference measurement is done. This leads to an increase of the Fermi radius of up to 8 %, and thus to an overestimation of the measured axially excited fraction.

In conclusion, we are able to prepare a quasi-2D system of approximately 65 000 atoms per spin state. Only for high temperatures, excitations in the third dimension become available for a small percentage of the sample. As expected, this effect is greater on the BCS side. Although small, it must not be neglected in the interpretation of our data. This is especially true in the light of recent theoretical work, which predicts an increase of the critical temperature due to an influence of the third dimension [Fis14] (see also chapter 2.3.4).

4.4. Accessing the Phase Diagram: Tuning Temperature and Interaction Strength

In order to map out the phase diagram of our quasi-2D strongly interacting Fermi gas, we have to tune two variables, the temperature and the interaction strength.

We always start our experiments by preparing the same quasi-2D sample at an offset field of 795 G and the lowest achievable temperature of approximately 55 nK to ensure reproducibility. Only then we change the temperature and interaction strength.

To change the temperature, we perform a controlled heating procedure. For the lowest three temperatures, we heat the gas by simply holding it in the trap for 0, 500, and 1000 ms. During this hold time, technical noise heats the gas by up to 20 nK. To access higher temperatures, we hold the gas in the trap for 1000 ms and additionally perform controlled parametric heating. For this parametric heating, we sinusoidally modulate the trap depth for 650 ms during the hold time. By varying the modulation amplitude between 0 and approximately 14 % of the trap depth in 19 steps, we can set the temperature.

To ensure that we always introduce the same amount of thermal energy and that the gas thermalizes quickly, we always perform the heating procedure at a magnetic offset field of 795 G, where the mean-field interactions are strong and repulsive.

After allowing the sample to equilibrate for 300 ms after the heating procedure, we ramp the magnetic offset field to ten different values between 692 G and 982 G in the vicinity of the broad Feshbach resonance at 832.2 G (see chapter 2.2.2).

Thus, also the 3D scattering length a and the dimensionless inverse 2D interaction strength ℓ_z/a change between $\ell_z/a \approx 7.12$ and $\ell_z/a \approx -2.35$. Throughout the whole experiment, we keep ℓ_z constant.

We perform all magnetic offset field ramps at a speed of $dB/dt \approx 1.9\,\mathrm{G/ms}$ and wait at the desired offset field for additional 20 ms before probing the gas. We ensure that the ramps are adiabatic by comparing the temperature of a sample which we ramped from $B = 732\,\mathrm{G}$ across the Feshbach resonance to $B = 900\,\mathrm{G}$ to that of a sample which we held at $B = 732\,\mathrm{G}$ for the same time. The temperatures of both samples agree well within their uncertainties.

4.5. Absorption Imaging

As mentioned in chapter 3.5, we use absorption imaging to probe our sample. The column density distribution is extracted from the shadow that the atom cloud casts in a pulse of resonant light. Whereas it is relatively simple to obtain qualitative information from absorption imaging, the extraction of quantitative information such as the 2D atom density or the atom number is delicate. This chapter therefore briefly reviews the principle of absorption imaging and the calibrations we make to obtain reliable atom densities. All calibrations are done for the vertical imaging axis, which we use to probe the radial density distribution.

4.5.1. Principle

A laser beam traveling through an atom cloud along the z-direction is attenuated as

$$\mathrm{d}I(\mathbf{r}) = -n(\mathbf{r})\,\sigma^*(I)\,I(\mathbf{r})\,\mathrm{d}z \quad , \tag{4.2}$$

where $I(\mathbf{r})$ is the intensity of the beam, n is the atom density, and $\sigma^*(I) = \frac{\sigma_0^*}{1+I/I_{sat}^*}$ is the effective absorption cross section with the effective saturation intensity I_{sat}^*. Integrating equation (4.2) through the whole cloud along the propagation direction yields

$$\begin{aligned} n_{2D}(x,y)\,\sigma_0^* &= -\ln\frac{I_t(x,y)}{I_0(x,y)} + \frac{I_0(x,y) - I_t(x,y)}{I_{sat}^*} && (4.3)\\ &= OD(x,y) + \frac{I_0(x,y)}{I_{sat}^*}(1 - e^{-OD(x,y)}) \quad , && (4.4)\end{aligned}$$

where n_{2D} is the atomic column density, $OD = -\ln\frac{I_t}{I_0}$ is the so-called optical density, and I_t and I_0 are the transmitted and the original intensity.

Experimentally, one takes three images in close succession to obtain the column density. The first image, called the absorption image, is taken with an imaging pulse and the atoms present, and yields $I_t(x,y)$. The second image is called the reference image. It is taken after discarding the atoms, typically using the same imaging pulse settings and yields $I_0(x,y)$. The third image is the so-called dark image. It is taken without an imaging pulse and subtracted from both other images to reduce the influence of stray light and camera noise.

Since the imaging pulse transfers momentum onto the atoms, absorption imaging is a destructive measurement. Thus, one has to prepare a new sample for each data point one wants to take.

4.5.2. Calibration

In the limit of low intensity ($I_0 \ll I^*_{sat}$), the cross section σ^*_0 is constant through the whole cloud and one can neglect the second term in equation (4.4). In this case, to obtain the 2D density n_{2D} of the sample, one only has to calibrate σ^*_0. In our case, σ^*_0 can be set to the literature value σ_0 in good approximation. We confirm this by comparing the saturation intensity I^*_{sat} obtained from our intensity calibration (see below) to the literature value. However, to improve the signal-to-noise ratio, it is helpful to use higher imaging intensities. For our experiments, we use $I_0 \approx I^*_{sat}$, and thus have to consider the second term in equation (4.4). Hence, we also have to calibrate $I_0(x,y)/I^*_{sat}$. Since the profile of our imaging beam is homogeneous at the position of the atoms to a good approximation, it is sufficient to calibrate I_0/I^*_{sat} independent of the position in the image.

For the calibration, we take images of a purely atomic sample at 1400 G with our regular imaging settings and with a 10 dB attenuated imaging pulse intensity. Assuming that the density distribution in the sample does not change over time, we evaluate the images according to equation (4.4). Doing this, we calibrate I_0/I^*_{sat} such that we obtain the same atomic density for both imaging intensities. Averaging over several sets consisting of approximately 100 realizations of this measurement leads to $I_0/I^*_{sat} = 0.97^{+0.13}_{-0.08}$. The errors are estimated by the minimum and maximum values obtained from the individual sets.

On the BEC-side of the Feshbach resonance, where the sample consists of diatomic molecules, the absorption cross section of the sample is reduced. We compensate for the reduced cross section with a calibration factor, which we obtain from imaging a sample with a defined atom number at different offset fields. The mean correction factor of approximately 50 realizations is given in table 4.1 for all magnetic offset fields used in our experiments. The errors are the standard errors of the mean.

Offset Field B [Gauss]	692	732	782	≥ 812
Calibration Factor	$1.33\,^{+0.10}_{-0.07}$	$1.37\,^{+0.11}_{-0.09}$	$1.06\,^{+0.06}_{-0.05}$	1

Table 4.1.: Correction factor for the reduced molecular absorption cross section for all investigated magnetic fields.

4.5.3. Improving the Image Quality

By taking the absorption image and the reference image as quickly after each other as possible, static interference fringes on the imaging beam are canceled from the recorded optical densities OD. However, there is always a finite time between the images. During this time, the fringes can move slightly, especially in the presence of mechanical vibrations, which we introduce by magnetic field ramps in some measurements (see chapter 4.6.3). These dynamic fringes are thus present in our data. We minimize them with the help of the fringe removal algorithm presented in [Ock10]. The algorithm constructs a basis set of background images from images with no atoms present, which we take in turns with the actual images. The background of each actual image is then fitted with this basis set in a region of interest which excludes the atom cloud. By subtracting the thus obtained background from the full image, fluctuations are reduced and the background becomes flatter.

In order to obtain a bigger signal and thus to enhance the signal-to-noise ratio, we increase the duration of the imaging pulse in the reference picture by a factor of 10. This leads to a constant offset of $\ln(10)$ in the optical density OD in equation (4.4). By using the above mentioned fringe removal algorithm, we automatically correct for this offset in our data.

4.5.4. Doppler Shift

During the $8\,\mu$s imaging pulse, the atoms are accelerated by the light force. Assuming saturated scattering, each atom scatters on average with approximately 70 photons. This leads to a random walk motion of the atoms on length scales of approximately $3\,\mu$m in radial direction, which is slightly less than our imaging resolution and can thus be neglected. However, the atoms also experience an acceleration along the imaging axis, and thus a Doppler shift. This Doppler shift linearly increases the effective atomic resonance frequency during the imaging pulse. At the end of the pulse, the detuning is approximately 10 MHz

We compensate for the Doppler shift by a sweep of the laser frequency. For this sweep, we modulate the current through the laser diode with a linear ramp over the duration of the imaging pulse. We fine-tune the amplitude of the ramp by experimentally maximizing the detected atom density.

4.6. Probing the Pair Momentum Distribution

In addition to the density distribution of the trapped gas, which we obtain by in-situ absorption imaging, we are also interested in its momentum distribution. The momentum distribution contains information which is complementary to that contained in the spatial density distribution. In particular, the existence of a condensate can hardly be detected in the density distribution in the presence of strong interactions. In the momentum distribution however, such a long range coherent phase manifests itself as an enhanced occupation of low momenta in the momentum distribution, independent of interactions (see chapter 2.3.3).

This chapter explains how we obtain the momentum distribution of the gas with the help of a matter-wave focusing technique. In contrast to free time-of-flight evolution, we focus the evolving gas with the help of a radial harmonic potential. After a quarter of the oscillation period, we obtain the radial momentum distribution. In addition, we perform a rapid magnetic field ramp which projects atom pairs into deeply bound molecules. Hence, the relative momenta of the atoms in a pair are removed from the detected momentum distribution. We thus obtain the pair momentum distribution, which enables us to detect bosonic and fermionic condensates in a consistent way.

4.6.1. The T/4 Technique

The standard technique to obtain information about the momentum distribution of an ultracold gas is time-of-flight evolution. In this method, the gas is released from the trap and allowed to evolve freely for a specified time t before an image of its density distribution is taken. After the free evolution, the initial momentum $\mathbf{p}$ of each particle in the gas is mapped onto a spatial position $\mathbf{x}$ according to

$$\mathbf{x}(\mathbf{p}, t) = \mathbf{x}_0 + \frac{\mathbf{p}}{m} t \quad , \tag{4.5}$$

where $\mathbf{x}_0$ is the initial position and m is the mass of the particle. This is depicted for the 1D case in figure 4.7. For $\frac{\mathbf{p}}{m} t \gg \mathbf{x}_0$, the final position is dominated by the momentum of the particle. However, in our system this is only the case for unfeasibly long t, especially for low-momentum particles. Thus, in our system it is impossible to obtain the undistorted momentum distribution of a many-body sample with this method.

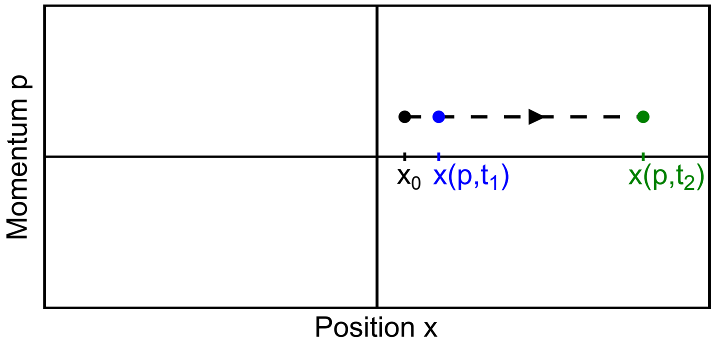

Figure 4.7.: Phase space evolution of a particle in free time-of-flight. For short evolution times t_1 (blue), the final position of the particle is heavily influenced by its initial position x_0. For sufficiently long times t_2 (green), the position after time-of-flight is much larger than x_0, and can be used as a measure for the initial momentum. However, for finite t there will always be a residual influence of x_0. Free time-of-flight evolution will thus always only yield an approximation of the momentum distribution of a many-body system.

In order to overcome this issue and still obtain the momentum distribution of our sample, we use a matter-wave focusing technique which we describe in [Mur14b].[3] Instead of a letting the gas evolve freely during the time-of-flight, we let it evolve in a weak harmonic potential U_{ev} with trapping frequency ω_{ev}. The phase space evolution during this process is depicted in figure 4.8. Each particle in the gas performs a harmonic oscillation in the potential. At an evolution time of a quarter period $t = T/4 = 2\pi/4\omega_{\mathrm{ev}}$, the initial momentum is hence completely transformed into a position according to $x(t = T/4) = \frac{p(t=0)}{m\omega_{\mathrm{ev}}}$. The density distribution at $t = T/4$ is thus a one-to-one mapping of the initial momentum distribution. In order to avoid distortions of the obtained momentum distribution, it is crucial that the particles do not interact during the time-of-flight but evolve ballistically.

We show in [Mur14b] that this technique does not only work in the simple intuitive picture of classical particles. It can also be described in terms of quantum field operators. Thus, also information about the phase of the quantum gas is conserved in the mapping process and can be extracted from the obtained momentum distribution.

---

[3] A similar technique was applied to a weakly interacting Bose gas in [Tun10].

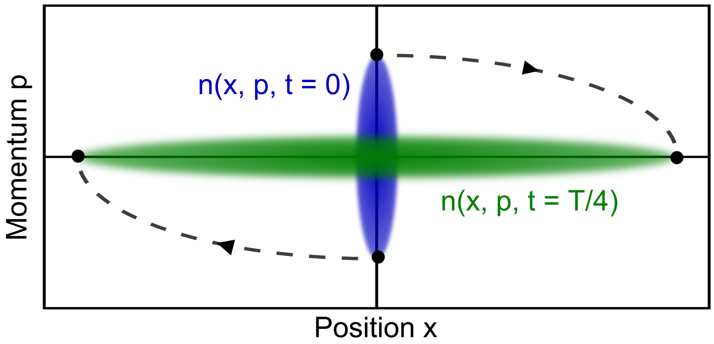

Figure 4.8.: Phase space evolution of a gas in a harmonic potential. After an evolution time of $t = T/4 = 2\pi/4\omega_{\text{ev}}$, the phase space distribution is rotated by $\pi/2$ and the initial momentum distribution is mapped onto the spatial distribution.

The $T/4$ technique is the matter-wave analog to optical focusing, where the focal plane of parallel beams can be shifted from infinity to a finite distance with the help of a lens. In this picture, U_{ev} corresponds to a long gradient index lens [Sal07] with a parabolic index profile in which the beams travel until they reach their focal plane.

4.6.2. Experimental Realization

We use the radial weakly confining harmonic potential of the magnetic offset field saddle point (see chapter 3.4.1) as evolution potential U_{ev}. This allows us to obtain the momentum distribution of our sample in the radial plane. Unlike a typical optical potential, this magnetic potential is very smooth and harmonic to a very good approximation up to radii of several millimeters. Thus, it only has minimal aberrations.

Before we probe the gas, it is trapped in a combination of the magnetic potential and the optical potential of the SWT. To perform the $T/4$ technique, we instantaneously turn off the SWT and let the gas evolve in the magnetic potential (see figure 4.9). For the evolution, we use a magnetic offset field of 692 G, which leads to a trapping frequency $\omega_{\text{ev}} = \omega_{r,\text{mag}} = 2\pi(10.2 \pm 0.1)\,\text{Hz}$. We thus choose an evolution time $t = 25\,\text{ms}$.

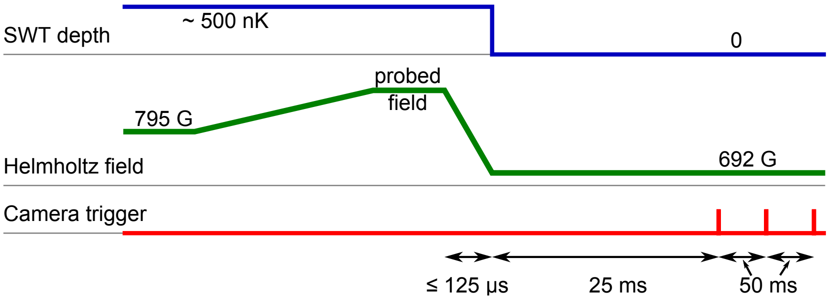

Figure 4.9.: Sketch of the experimental sequence during the pair momentum distribution imaging. We adjust the interactions in the quasi-2D Gas to the desired value with the help of the magnetic offset field (see chapter 4.4). Just before releasing the sample from the trap, we rapidly ramp the magnetic offset field to the smallest accessible interaction strength on the BEC side of the resonance. In this way, we minimize interactions after the release and project atom pairs into deeply bound molecules. We then let the gas evolve in the harmonic magnetic potential provided by the saddle point of the offset field for an evolution time of $t = T/4 = 25\,\mathrm{ms}$. After this time, the initial pair momentum distribution is completely mapped onto the spatial distribution. Finally, we take an absorption image (see chapter 3.5) of the obtained distribution.

4.6.3. Quenching Interactions and Pair Projection: the Rapid Ramp Technique

In order to avoid redistribution of momentum during the time-of-flight evolution, which would alter the obtained momentum distribution, we have to minimize interactions during the evolution. Partially, this is taken care of automatically by the rapid expansion of the gas in axial direction after the release from the SWT. This expansion is due to the large axial trapping frequency. The axial Gaussian width σ_z of the sample as a function of time is shown in figure 4.10. In less than 5 ms, σ_z increases by almost two orders of magnitude. Consequently, the density of the sample decreases by a similar factor and collisions between the atoms become negligible.

This feature of the quasi-2D gas effectively quenches interactions after the first milliseconds of time-of-flight evolution. However, during and shortly after the release the density is still high and collisions are present. Especially for strongly interacting gases where the scattering amplitude is large, this can still distort the obtained momentum distribution.

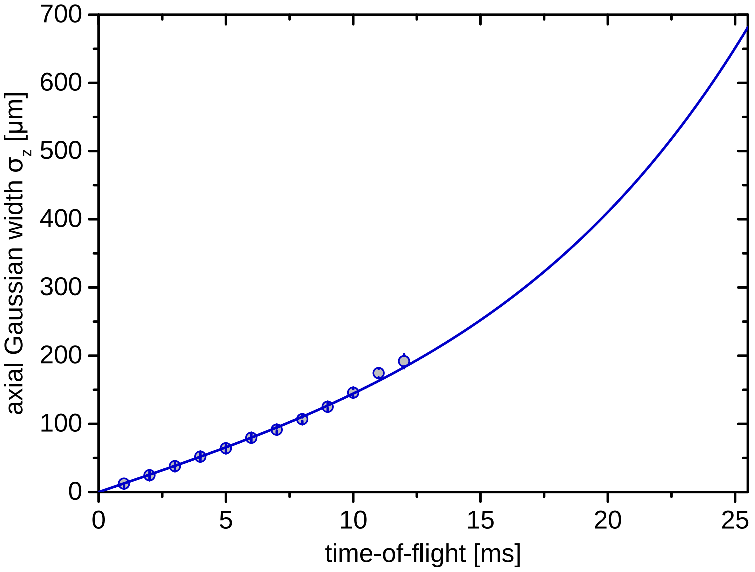

Figure 4.10.: Axial Gaussian width σ_z during time-of-flight evolution. Due to the tight confinement in z-direction, the gas expands quickly in this direction. Thus, its density is reduced quickly and interactions are minimized. The line describes the hydrodynamic expansion of a 3D Fermi gas in the BEC limit into a harmonic saddle point potential as described in [Ket08, Cla08], and was adapted to our experimental parameters. As already observed in [Dyk10], it also describes the quasi-2D case well.

In order to reduce these interactions, we ramp the magnetic offset field to $B = 692\,\mathrm{G}$ right before we release the gas from the SWT. At this magnetic field, $a \approx 1500\,a_0$, which is the lowest feasible interaction strength on the BEC side. We perform the ramp at the maximum possible speed of $dB/dt \approx -2.4\,\mathrm{G}/\mu\mathrm{s}$, which leads to ramp durations of less than $125\,\mu\mathrm{s}$. This is fast enough that the momentum distribution cannot adjust to the new interaction strength (see below).

A similar rapid ramp technique was also used for measurements in the 3D BEC-BCS crossover [Reg04, Zwi04, Zwi05]. In addition to quenching the interactions, it projects atom pairs into deeply bound molecules. This has the important consequence that the relative momentum of the atom pair is projected out. Our measured momentum distribution thus only contains the center of mass momentum of atom pairs. Hence, we can neither distinguish between fermionic Cooper pairs and bosonic molecules, nor obtain information about the Tan contact [Tan08]. On the other hand, this has the great advantage that also fermionic BCS condensates give the clear signature of an enhanced low-momentum density. It thus enables us to analyze the momentum distribution for condensation in a consistent way both on the BEC- and on the BCS side of the resonance.

Validation

In order to exclude systematic effects that alter the momentum distribution during the matter-wave focusing process, we investigate two effects: non-ballistic expansion and the adaptation of the sample to the interaction strength after the rapid magnetic field ramp.

Non-ballistic expansion due to interactions during the time-of-flight evolution can be quantified by estimating the number of scattering events during the evolution. At $B = 692\,\mathrm{G}$, the sample consists of deeply bound molecules. Their mean scattering rate is given by

$$\Gamma_{\mathrm{sc}} = \sigma \bar{v} \bar{n} \quad . \tag{4.6}$$

The total scattering cross section between the bosonic molecules (see chapter 2.2.1) is given by $\sigma = 8\pi a^2$. The mean velocity of the molecules is $\bar{v} = \sqrt{2k_B T / 2m}$, where $2m$ is the mass of a molecule. We estimate the mean in-situ molecule density $\bar{n}_{\mathrm{in-situ}}$ from the measured mean 2D density $\bar{n}_{2D}$, assuming a Gaussian distribution of the molecules in the lowest axial harmonic oscillator level of the SWT. Neglecting expansion in radial direction, we estimate the mean density in time-of-flight to be

$$\bar{n}(t) \approx \bar{n}_{\mathrm{in-situ}} \frac{\sigma_{z,\, in-situ}}{\sigma_z(t)} \tag{4.7}$$

with the axial Gaussian width σ_z (see figure 4.10).

The total number of scattering processes per molecule during time-of-flight as a function of time can now be found by integrating Γ_{sc} over the evolution time:

$$N_{\mathrm{sc}}(t) = \int_0^t \Gamma_{\mathrm{sc}}(t) dt \quad . \tag{4.8}$$

For the coldest achievable temperatures ($T \approx 65\,\mathrm{nK}$), $N_{sc}(t)$ is depicted in figure 4.11. Most of the scattering processes occur during the first milliseconds of the expansion, while the density is still large. For longer times, the scattering rate goes to zero and the number of scattering processes per molecule saturates to $N_{\mathrm{sc}}(t \to \infty) \approx 0.1$. Thus, only about 10 % of the molecules scatter during the whole process. Hence, the redistribution of momentum during the release and the time-of-flight evolution is negligible.

Adaptation to the interaction strength after the rapid ramp is an important issue, as it would lead to signatures of condensation at points in the phase

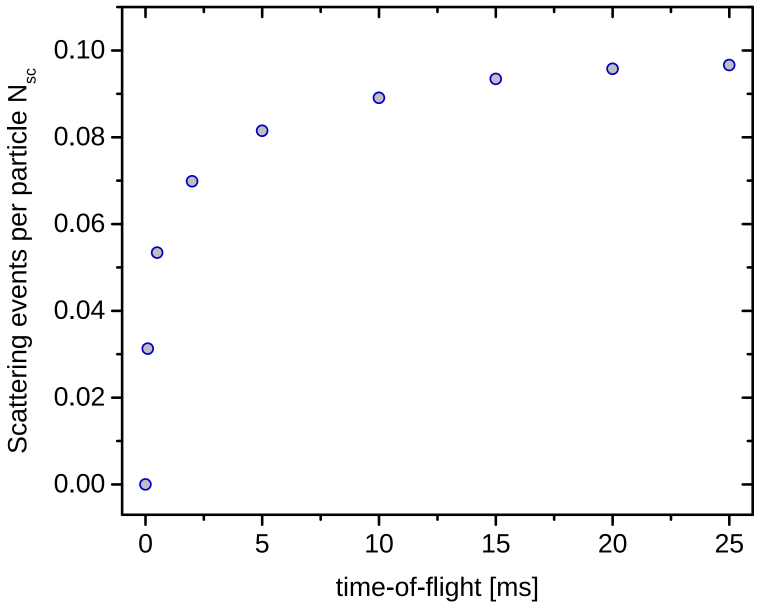

Figure 4.11.: Simulation of the total scattering events per particle during time-of-flight evolution in the harmonic potential. After a steep increase for short times, where the density is high, $N_{\mathrm{sc}}(t)$ saturates to approximately 0.1. This number of collisions can only lead to a negligible redistribution of momentum.

diagram where no condensation occurs. The timescale of the ramp thus has to be fast enough so the momentum distribution cannot adjust to the new interaction strength.

To ensure this, we extract the temperature (see chapter 5.2.1) from momentum distributions obtained with and without the rapid ramp both on the BEC side (732 G) and on the BCS side (872 G) of the resonance. For both interaction strengths, the temperatures are consistent within their uncertainty. Thus, the measured temperature is not affected by the rapid ramp.

Furthermore, we investigate the non-Gaussian fraction of the momentum distribution, which manifests itself in an enhanced occupation of low momentum states (see chapter 5.2.2) and is a signature of condensation. This low momentum peak is destroyed during the release in the strongly interacting limit. In the fermionic limit, it is not visible without the rapid ramp, which projects atom pairs into deeply bound molecules and thus removes the relative momentum of their constituents. Thus, we can only directly compare the non-Gaussian fraction with and without the ramp in the bosonic regime. Here, we find them to be identical.

Additionally, we ensure that the ramp to the bosonic regime does not create a non-Gaussian fraction even when there was none present in the original sample, especially for high magnetic fields on the BCS side. To do this, we prepare a sample at 900 G at a temperature where we do not observe condensation. We then perform the rapid ramp, and afterwards keep the sample in the trap for a variable hold time t_{hold}, before we release it for $T/4$ momentum distribution imaging.

We observe that the non-Gaussian fraction starts to develop in the sample only after $t_{\mathrm{hold}} \approx 11\,\mathrm{ms}$. Thus, the adaptation to the new interaction strength is two orders of magnitude slower than the rapid ramp, which we perform in less than $125\,\mu\mathrm{s}$. Hence, the rapid ramp technique does not affect the measured non-Gaussian fraction.

4.6.4. Axial Collimation

As an extension to the $T/4$ matter-wave focusing technique, we developed a technique to limit the fast axial expansion of the sample. The expansion has the desirable effect to reduce the density and thus interactions during the evolution time. However, it also leads to a large axial extension of the sample at the end of the time-of-flight evolution. This extension is greater than the depth of focus of our imaging setup, and thus limits the optical resolution.

The implementation of the axial collimation technique complicates the measurement process and caused technical problems while taking the data presented here. Since the momentum resolution without the axial collimation is sufficient for the analysis we performed with this data, we thus decided not to use it for our measurements. However, since it will be helpful for future high-resolution measurements of the momentum distribution it is shortly presented here.

In order to stop the axial expansion, we again rely on the evolution of the gas in a harmonic potential. Shortly after releasing the sample from the SWT into the radial evolution potential U_{ev}, we turn on the CBODT, which we modulate as explained in chapter 4.2.2 in order to make it as round as possible in the radial plane. The atoms then evolve in the CBODT for a quarter of its axial oscillation period, until they reach their turning point in the potential. After this time, the axial expansion is stopped and we turn the CBODT off again. A similar technique has been described as Delta-Kick Cooling in [Amm97]. The working principle is depicted in figure 4.12.

In a first experiment, we use an axial trapping frequency of $\omega_z^{\mathrm{CBODT}} \approx 2\pi \cdot 500\,\mathrm{Hz}$ for the collimation pulse. The collimation is thus achieved after $t_{\mathrm{col}} = 2\pi/4\omega_z^{\mathrm{CBODT}} \approx 0.5\,\mathrm{ms}$. Figure 4.13 shows the axial extension of the gas during the time-of-flight evolution with (blue) and without (green) the collimation pulse. The axial Gaussian width σ_z after the evolution time is strongly reduced to approximately $70\,\mu\mathrm{m}$ by the collimation pulse.

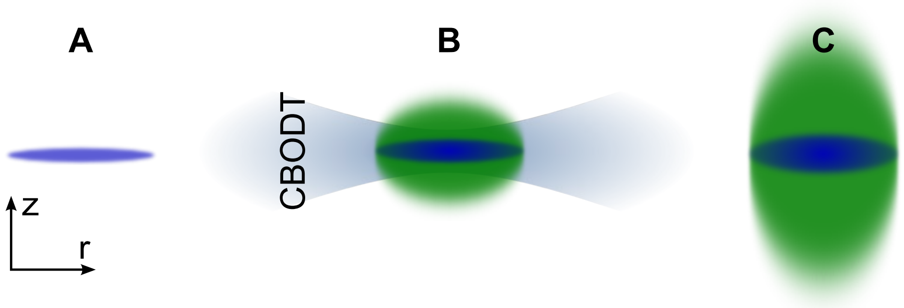

Figure 4.12.: Evolution of the density distribution during time-of-flight with (blue) and without (green) the collimation pulse. Shortly after the release from the SWT (A), the CBODT is switched on for a quarter of its axial oscillation period. The axial expansion of the sample is thus stopped (B). After time-of-flight expansion, the axial extension of the collimated sample is considerably smaller than that of the uncollimated sample (C).

During the axial collimation, the sample also experiences a potential in radial direction. This leads to an additional focusing in radial direction and thus to a decreased evolution time. At the used depth of the CBODT, the radial trapping frequency is on the order of $2\pi \cdot 10\,\mathrm{Hz}$,[4] which is similar to that of the radial magnetic potential $\omega_{\mathrm{ev}} = 2\pi(10.2 \pm 0.1)\,\mathrm{Hz}$. Since the atoms evolve in the combined potential only for a short time, the total evolution time is thus only slightly reduced.

In principle, the ellipticity of the modulated CBODT in the radial plane should lead to an elliptic distortion of the measured pair momentum distribution. Similar to the effect of the collimation on the expansion time, the elliptic distortion is small. Assuming a harmonic CBODT potential, we calculate it to be below $1\,\%$. However, due to the strong anharmonicity of the modulated CBODT in radial direction, it might deviate from this estimate. In the momentum distributions obtained with the collimation pulse, we do not see a significant distortion.

As mentioned above, we did not use the axial collimation technique for the measurements presented in this thesis since it introduces additional experimental complications and error sources. The two most important points are described below.

Due to an asymmetry in the control circuit of the offset field coils, the rapid magnetic field projection ramp leads to a transfer of momentum in axial direction

---

[4] Due to the modulation of the CBODT, we cannot measure the actual trapping frequency and have to estimate it from the unmodulated case.

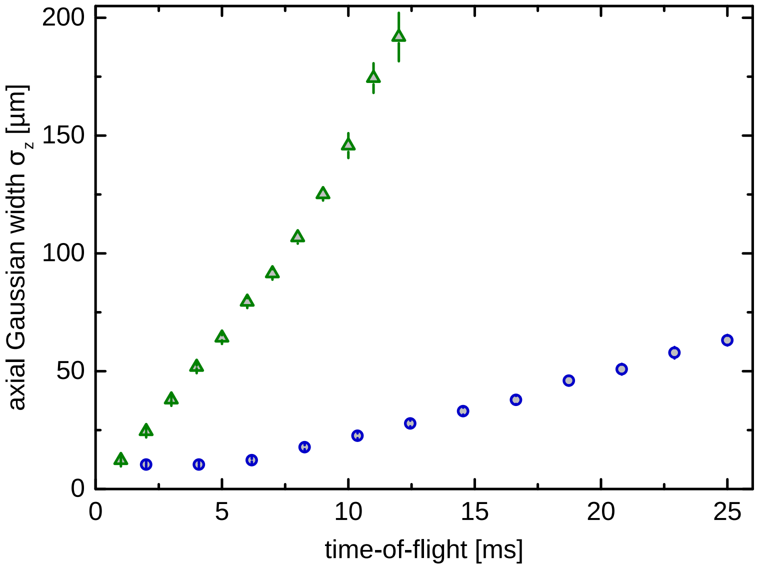

Figure 4.13.: Axial Gaussian width σ_z of the gas during time-of-flight evolution without (green) and with (blue) collimation pulse. With the help of the collimation pulse, it is possible to reduce σ_z to approximately $70\,\mu$m after time-of-flight evolution. Thus, the optical resolution should not be limited by the vertical extension of the gas anymore.

on the whole sample. Without the collimation pulse, we can compensate for this momentum by applying a magnetic field gradient during the time-of-flight evolution. For the collimation pulse however, it is crucial to have a good alignment of the CBODT with the sample, which we could not achieve in combination with the projection ramp.

Additionally, by limiting the axial expansion of the gas, one also achieves a higher scattering rate during time-of-flight evolution. This might influence the measured momentum distribution more than the loss of optical resolution due to the large axial extension of the gas.

We were able to improve the offset field control circuit since we took the presented data. Additionally, it should be possible to sufficiently reduce the scattering rate during time-of-flight evolution by using a lower magnetic offset field. Thus, we will be able to use the collimation technique for future measurements and hence improve the resolution of the measured momentum distribution.

5. Pair Condensation in a Strongly Interacting 2D Fermi Gas

With the techniques described in the two previous chapters, we investigate the properties of the 2D Fermi gas in the BEC-BCS crossover. Parts of the content of this chapter have been published in [Rie14].

We create a quasi-2D sample in a single layer of the SWT, which we then probe at 10 different interaction strengths and 22 different temperatures to map out the phase diagram. For each point in the phase diagram, we measure both the density distribution and the corresponding pair momentum distribution in the radial plane by in-situ and $T/4$ absorption imaging. The obtained absorption images are shown in figures 5.1 (density distribution) and 5.2 (pair momentum distribution) for some of the investigated temperatures and interaction strengths.

In the density distribution shown in figure 5.1, one can nicely see the smooth crossover from a bosonic system at low magnetic offset fields to a fermionic system at high magnetic fields. At the weakest interaction strength in the bosonic regime (692 G), the sample consists of bosonic molecules. They accumulate in the lowest energy states of the harmonic trap, which leads to a narrow density distribution with central densities of up to $2.7\ \text{atoms}/\mu\text{m}^2$. With increasing magnetic fields, the growing repulsive interaction between the molecules leads to a broadening of the density distribution. At the same time, the central density is reduced. For even higher magnetic fields, the molecules dissociate and the gas consists of attractively interacting fermionic atoms. In this regime, the width of the density distribution grows even further due to the Pauli pressure. At the same time, the peak density decreases until it reaches approximately $0.76\ \text{atoms}/\mu\text{m}^2$ at the lowest temperature at 922 G.

With increasing temperature, the distribution becomes broader and the central density gradually decreases to values between $1.1\ \text{atoms}/\mu\text{m}^2$ (692 G) and $0.61\ \text{atoms}/\mu\text{m}^2$ (922 G).

In the pair momentum distribution shown in figure 5.2, one observes a drastic enhancement of the density at low momenta. The height of this sharp low-momentum peak reaches its maximum at the lowest temperatures around 782 G. Here, the central momentum density is larger by a factor of approximately 34 than that of the highest shown temperature at the same field. Far on the BCS

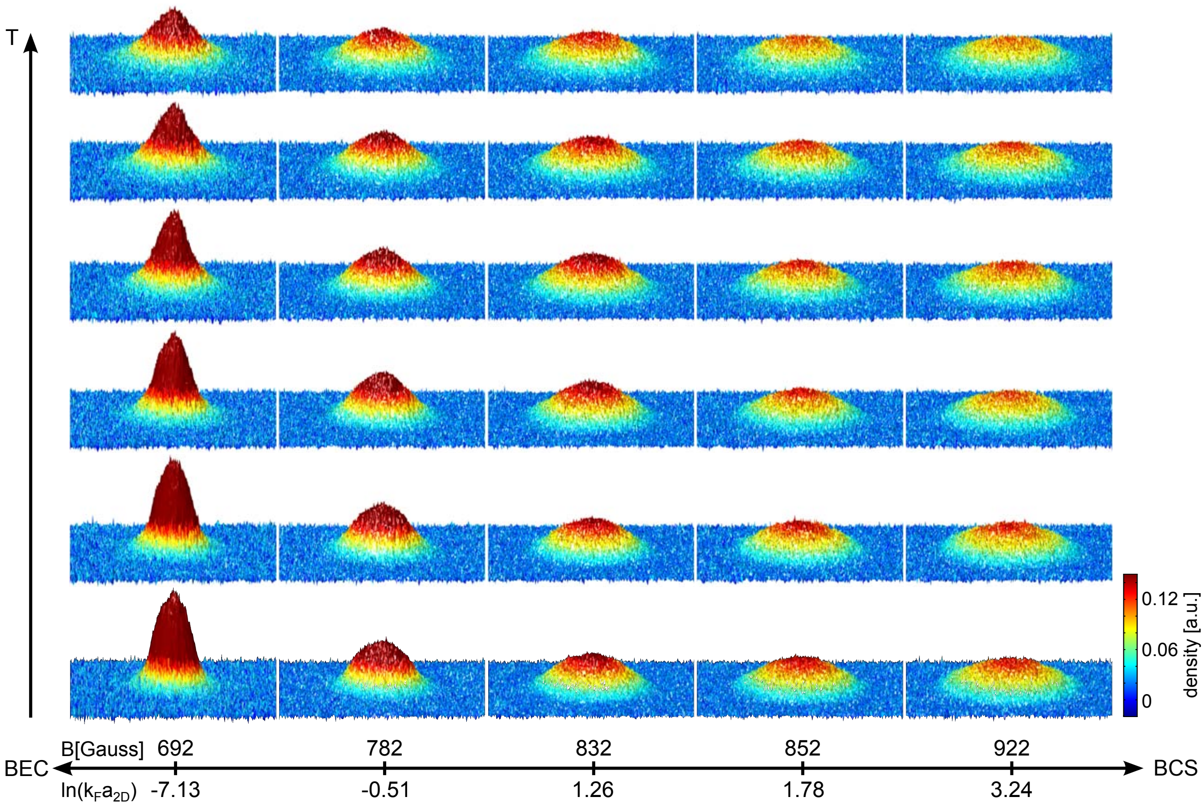

Figure 5.1.: In-situ density distribution of the gas for some of the investigated interaction strengths and temperatures. One can nicely observe the smooth transition between a gas of bosonic molecules, which has a narrow distribution with a high central density, and a Fermi gas, which has a wide and much flatter distribution. Each image is the average of approximately 30 individual measurements.

side (922 G), the peak vanishes. With increasing temperature, the central momentum density decreases. For sufficiently high temperatures, the sharp peak vanishes for all investigated interaction strengths.

Comparing the momentum- and density distribution at the coldest temperatures at 852 G and 922 G, one observes a jump by a factor of 9 in the peak momentum density $\tilde{n_0}$, whereas the central spatial density n_0 only changes by less than 10 %. On the temperature axis (vertical axis in figures 5.1 and 5.2), the behavior is qualitatively similar: there is a rapid increase of the low momentum density while the central density of the gas changes only slightly.

We attribute the observed macroscopic occupation of low momentum states to

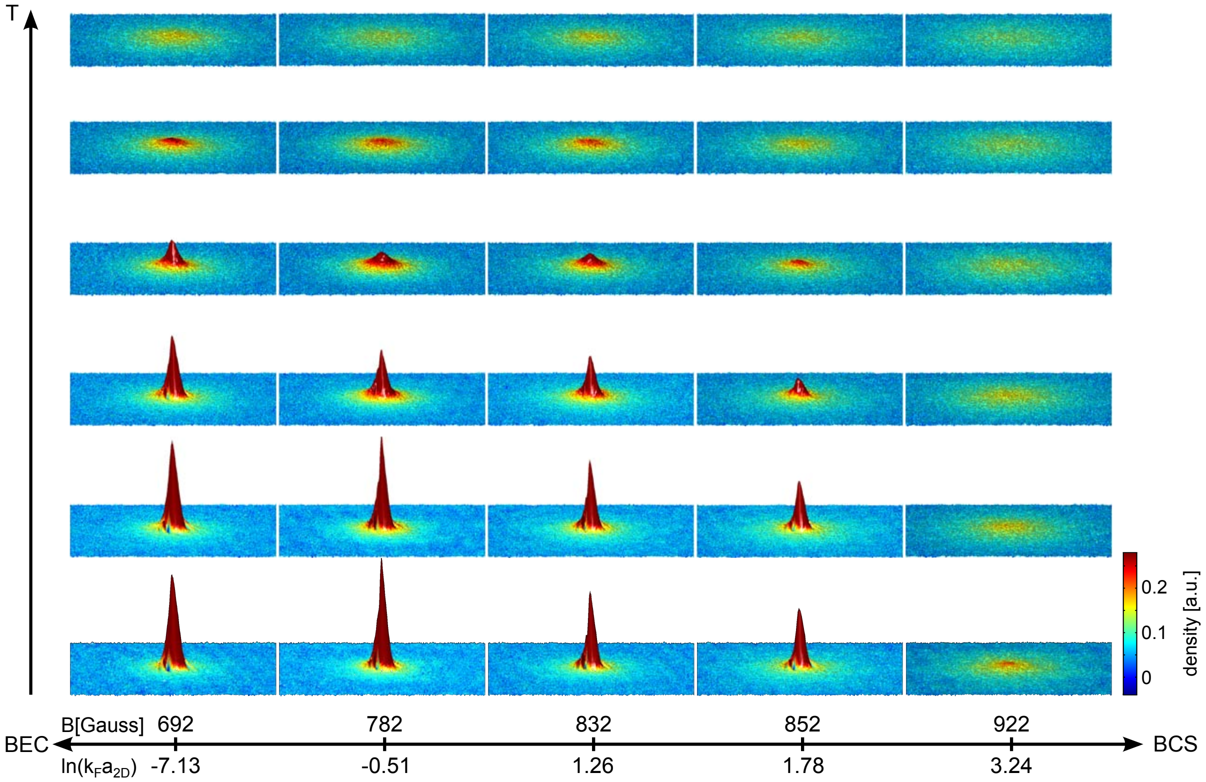

Figure 5.2.: Momentum distribution of the gas for the same interaction strengths and temperatures as in figure 5.1. A dramatic peak at low momenta is clearly visible for low temperatures and small magnetic fields. It heralds the condensation of the gas into a phase of long range phase coherence. Each image is the average of approximately 30 individual measurements.

the existence of a low-temperature phase with long range phase coherence. The observed abrupt increase of this order parameter thus heralds the condensation of the gas into this phase. Similar observations have been made with 3D Bose-Einstein condensation [And95, Dav95] and in 2D Bose gases [Cla09, Tun10, Pli11], where they were interpreted as BKT phase transition into the QLRO superfluid phase (see chapter 2.3.3).

The following chapters treat the quantitative analysis of the measured density- and pair momentum distributions. First, it is shown how we determine the Fermi temperature of the sample from its peak density and thus map the system onto a homogeneous 2D Fermi gas. Then, the extraction of the temperature and the non-thermal fraction of the sample is described, and the determination of the critical temperature is explained. Finally, all obtained quantities are combined to create the phase diagram of the gas. Furthermore, we analyzed the coherence properties of the gas, which is described in the last chapter.

Due to the good radial symmetry of both distributions, we azimuthally average all data and perform the further analysis with the radial distributions. This has the advantage of improving the signal-to-noise ratio especially at large radii, where the density is low and noise becomes an issue.

5.1. Normalization of Temperature and Interaction Parameter

In order to obtain universally valid results for a generic Fermi gas, we normalize all measured temperatures to the Fermi temperature T_F. We use the homogeneous definition of T_F as given in equation (2.34),

$$T_{F,2D} = \frac{\hbar^2}{2mk_B}(4\pi n_{2D}) \quad ,$$

where we replace n_{2D} with the central 2D density n_0 of our sample. Thus, we apply local-density approximation (LDA) in the middle of the trap, where the phase space density is highest, and map our trapped gas onto the homogeneous description.

Furthermore, we characterize the interaction strength in units of $\ln(k_F a_{2D})$. In analogy to T_F, we obtain k_F in LDA from the central 2D density of our sample according to the homogeneous definition given in equation (2.35):

$$k_{F,2D} = \sqrt{4\pi n_{2D}} \quad .$$

Thus, all obtained so-called degeneracy temperatures T/T_F and interaction strengths $\ln(k_F a_{2D})$ can be directly compared to the homogeneous Fermi gas with a generic contact interaction.

In contrast to the homogeneous system, the peak column density and thus the Fermi temperature T_F and wave vector k_F change with temperature and interaction strength. To adjust the interaction strength, we tune the 3D scattering length a by means of a magnetic Feshbach resonance (see chapter 2.2.2). This adjusts the 2D scattering length a_{2D} according to equation (2.17). In addition to a_{2D}, the 2D interaction parameter $\ln(k_F a_{2D})$ also depends on k_F and thus on the peak column density which changes with temperature. Thus, $\ln(k_F a_{2D})$ is not constant at a given magnetic offset field. We hence use the magnetic offset field to identify the interaction strength when referring to a data set which includes different temperatures. Values of $\ln(k_F a_{2D})$ which correspond to more than one temperature are approximate values and correspond to $\ln(k_F a_{2D})$ at T_c/T_F. A translation of the used magnetic fields into ℓ_z/a can be found in table A.1 in the appendix.

The dependence of the Fermi temperature on the interaction strength and the temperature is shown in figure 5.3.

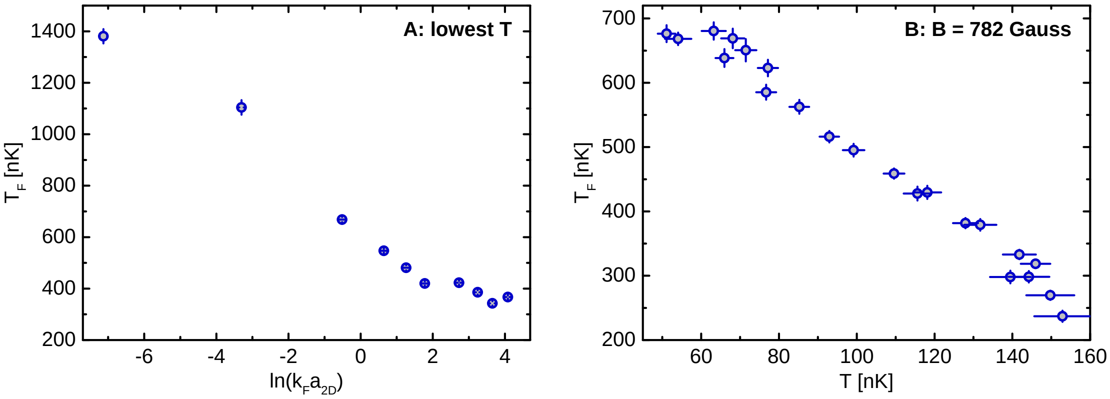

Figure 5.3.: Fermi temperature T_F as a function of $\ln(k_F a_{2D})$ at the lowest attainable temperature (A) and as a function of temperature at 782 G ($\ln(k_F a_{2D}) \approx -0.59$) (B). The values are obtained from the central 2D density in an LDA mapping to the homogeneous case according to equations (2.34) and (2.35). Each data point is the average of approximately 30 individual measurements, error bars denote the standard error of the mean (SEM).

Figure 5.3 (A) shows the Fermi temperature T_F of the sample as a function of $\ln(k_F a_{2D})$ at the lowest attainable temperature. In the fermionic regime, where $\ln(k_F a_{2D}) \gg 1$, T_F goes towards approximately 350 nK, and is still decreasing at the largest $\ln(k_F a_{2D})$ shown. It reaches $k_B T_F \approx \hbar\omega_z \approx k_B \cdot 265\,\mathrm{nK}$ at 1400 G, which we have adjusted with the particle number (see chapter 4.3). For decreasing $\ln(k_F a_{2D})$, T_F grows until it reaches $T_F \approx 1400\,\mathrm{nK}$ at $\ln(k_F a_{2D}) \approx -7.1$. Note that here, in the bosonic limit, the Fermi surface does not exist. T_F should therefore be interpreted as a typical density scale of the system.

Figure 5.3 (B) shows T_F as a function of temperature at a magnetic field of 782 G ($\ln(k_F a_{2D}) \approx -0.59$). With growing temperature, the harmonically trapped sample can access a larger area in the trap and becomes less dense. In the homogeneous gas, this decrease in density corresponds to a decrease in T_F and in $k_F \propto \sqrt{T_F}$. Thus, also $\ln(k_F a_{2D})$ decreases with growing temperature at a constant magnetic field.

5.2. Temperature and Condensate Fraction

Since we have access to the pair momentum distribution of the gas, we can simply obtain its temperature from a Boltzmann fit to the thermal wings. In combination with the Fermi temperature T_F, we can extract the dimensionless degeneracy temperature T/T_F. Thus, our temperatures can be directly compared to generic fermionic theory.

The Boltzmann fit also yields the non-thermal fraction N_q/N of the gas, which we define as the fraction of the momentum density which exceeds the thermal distribution. This quantity is an important measure for the observed condensation. However, in 2D it cannot be used to extract the transition temperature T_c, since already significantly above T_c the momentum distribution deviates from that of a thermal gas.

5.2.1. Temperature

To obtain the temperature of each sample, we fit the thermal wings of the radial pair momentum distribution with a Boltzmann distribution

$$\tilde{n}(p, t=0) = n(r, t=T/4) = A_0 \exp\left(-\frac{M\omega_{\mathrm{ev}}^2 r^2}{2k_B T}\right) \quad . \tag{5.1}$$

Here, A_0 is the amplitude, M is the mass of the evolving particles, $\omega_{\mathrm{ev}} \approx 2\pi(10.2 \pm 0.1)\,\mathrm{Hz}$ is the trapping frequency of the magnetic evolution potential, k_B is Boltzmann's constant and T is the temperature of the sample. The average radial pair momentum distribution at the lowest attainable temperature at $\ln(k_F a_{2D}) = -0.51$ (782 G) and the corresponding fit are shown in figure 5.4. In order to make the Boltzmann fit appear as a straight line, we plot $\log(\tilde{n}(k))$ against k^2, where $k = p/\hbar$.

In the high-momentum wing, the Boltzmann fit describes the data well over more than one order of magnitude in density, and approximately an order of magnitude on the momentum axis. This corresponds to more than 50 pixels. For low momenta, the momentum density shows the already mentioned enhancement and exceeds the Boltzmann fit by up to two orders of magnitude.

Figure 5.5 shows the obtained temperature as a function of the heating strength (see chapter 4.4) on the BEC side (692 G, $\ln(k_F a_{2D}) \approx -7.3$) and on the BCS side of the resonance (952 G, $\ln(k_F a_{2D}) \approx 3.7$). In the BCS regime, one observes that

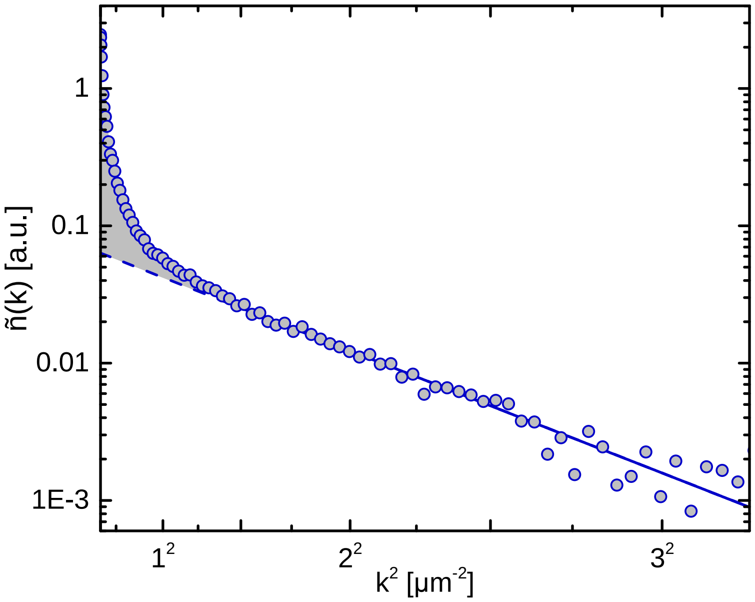

Figure 5.4.: Pair momentum density as a function of the momentum at the lowest attainable temperature $T/T_F \approx 0.08$ at $\ln(k_F a_{2D}) \approx -0.51$. The thermal wing is well described by a Boltzmann distribution (equation (5.1)), which appears as a straight line in this representation. It yields the temperature of the gas. At low momenta, the momentum distribution exhibits a condensate peak which clearly exceeds the thermal distribution. The non-thermal fraction N_q/N is marked in gray. Data points are the average of approximately 30 azimuthally averaged measurements. The solid part of the fit curve indicates the fit range.

the temperature only increases up to a heating strength of 17. When the gas is heated further, it stays constant. This behavior can be explained by looking at the particle number: for stronger heating, particles are lost on the fermionic side.[1] We thus do not use the data at these very high temperatures for the further analysis.

In both regimes, the lowest attainable temperatures agree within their errors and are at approximately 65 nK. The highest attainable temperatures lie at approximately 180 nK (BEC side) and approximately 93 nK (BCS side). Since both samples are heated in an identical way before the different interaction strengths are set (see chapter 4.4), this seems unexpected at the first glance. However, one has to take into account that the effective particle number differs by a factor of two between the two limits. Whereas the gas consists of free atoms on the BCS

---

[1] On the bosonic side, the particles occupy lower trap levels and are therefore are not lost for similarly strong heating.

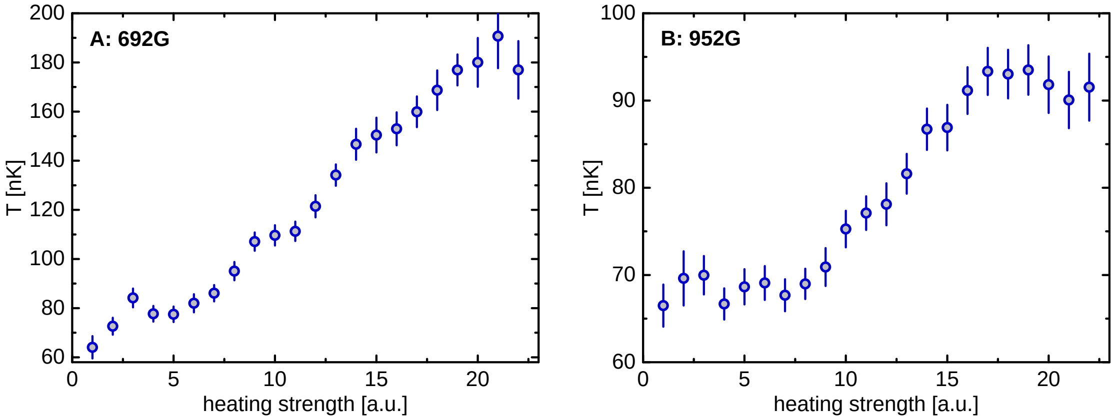

Figure 5.5.: Temperature of the gas as a function of the heating strength on the BEC side (A) and the BCS side (B). For heating strengths larger than 17, particles get lost on the BCS side and the temperature stays approximately constant. Thus, we do not use these high temperatures for further analysis. The highest temperatures differ by almost a factor of 2 between (A) and (B). This is due to the formation of diatomic molecules on the BEC side, which reduce the particle number and thus the heat capacity of the thermal gas by a factor of 2. Each data point is the average of approximately 30 individual measurements, error bars denote the SEM.

side, it consists of half as many diatomic molecules on the BEC side. In a 2D classical ideal gas of structureless particles, the temperature T of a gas is related to the particle number N and internal energy U by [Dem13]

$$U = Nk_B T \quad . \tag{5.2}$$

Thus, an increase by a factor of two in N as our sample is ramped across the crossover and molecules become unbound leads to a decrease in T by the same factor.

At the highest investigated temperatures, our gas approaches the thermal limit and thus the factor of 2 in difference between the BEC side and the BCS side. At smaller temperatures, the gas is quantum degenerate and the simple classical gas description breaks down.

Mass Dependence of the Fitted Temperature

As one can see from equation (5.1), the temperature extracted from the Boltzmann fit to the momentum distribution is proportional to the mass M of the expanding particles. On the BCS side of the resonance ($B \geq 892\,\mathrm{G}$), the thermal part of the gas consists of free atoms with mass $M = m$. On the BEC side ($B \leq 782\,\mathrm{G}$), it consists of diatomic molecules and $M = 2m$.

In the crossover ($782\,\mathrm{G} < B < 892\,\mathrm{G}$), the thermal part consists of a mixture of atoms and molecules. However, we do not observe two separate slopes in the pair momentum distribution. Thus, it is unclear which mass to use for the temperature determination. However, fits assuming the atomic and the molecular mass yield the lower and upper bound for the temperature of the gas.

Due to the continuous character of the crossover, it seems reasonable to assume a monotonous behavior of the temperature with the interaction parameter. For simplicity, we perform a first-order approximation and linearly interpolate the degeneracy temperature T/T_F between 782 G and 892 G for each heating strength. This is illustrated for the lowest attainable temperature in figure 5.6.

The qualitative behavior of the thus obtained temperatures in the crossover seems to justify the simple linear interpolation. The degeneracy temperature is close to that obtained with the molecular mass on the bosonic side and becomes closer to that obtained with the atomic mass as the sample becomes more fermionic.

We estimate the systematic uncertainties of this method by considering the upper and lower bound for T/T_F. To obtain these bounds, we make two assumptions:

- the temperature behaves monotonic in the crossover, i.e. $(T/T_F)_{782\,G} < T/T_F < (T/T_F)_{892\,G}$, and
- T/T_F has to lie between the value obtained with the atom and the molecule mass, i.e. $(T/T_F)_m < T/T_F < (T/T_F)_{2m}$.

The combination of these intervals for each data point then yields the bounds and thus a conservative estimate of the systematic uncertainty. The obtained uncertainties can be found in chapter A.3 in the appendix.

5.2.2. Non-Thermal Fraction

In addition to the temperature, the Boltzmann fit to the radial pair momentum distribution also yields the non-thermal fraction N_q/N of the gas.[2] We define this quantity as the fraction of the momentum density which lies above the Boltzmann

---

[2] This non-thermal fraction is denoted the quasi-condensate in some publications [Pro01, Pro02].

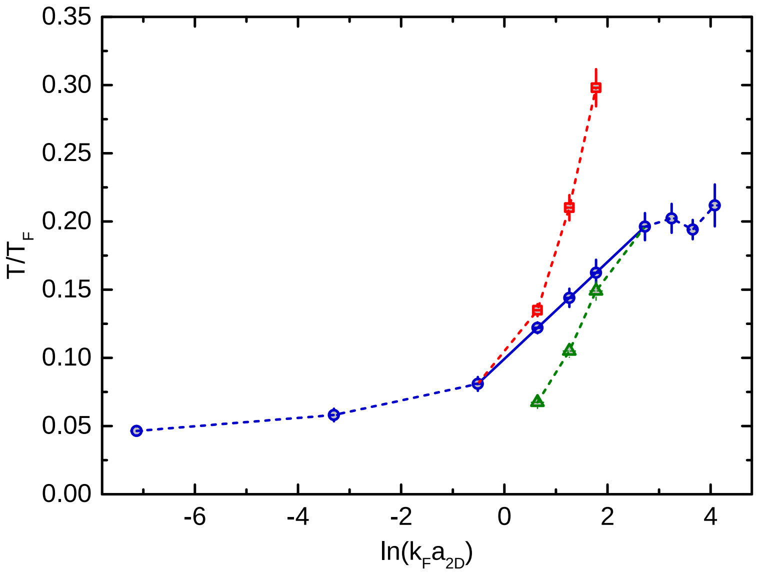

Figure 5.6.: Temperature interpolation at the lowest attainable temperature. We obtain T/T_F in the crossover by interpolating between the last clearly bosonic and fermionic points for each heating strength (solid blue line). The obtained temperature lies between those obtained with the molecular (red squares) and atomic (green triangles) mass. It approaches the molecular temperature close to the BEC side and the atomic temperature close to the BCS side. Note that the behavior of T/T_F indicates that the crossover from molecules to atoms in the thermal part happens at small positive $\ln(k_F a_{2D})$ rather than at $\ln(k_F a_{2D}) = 0$ (see chapters 2.3.4 and 5.4). Each data point is the average of approximately 30 individual measurements, error bars denote the SEM. Systematic uncertainties of the interpolation are not depicted.

fit (gray area in figure 5.4). In the BEC limit, N_q/N thus includes effects of Bose enhancement. Without knowledge of the chemical potential, the exact magnitude of this effect is hard to quantify. However, fitting the momentum distribution with a Bose function only yields plausible results when the enhancement over the Boltzmann fit is smaller than a few percent. Still, for the interpretation of our data, one should keep this effect in mind. Figure 5.7 shows the obtained non-thermal fraction as a function of the degeneracy temperature T/T_F at an interaction strength of $\ln(k_F a_{2D}) \approx -0.59$ (782 G).

The non-thermal fraction reaches values of almost 60 % for the coldest attainable temperatures ($T/T_F \approx 0.08$). With increasing temperatures, it first decreases

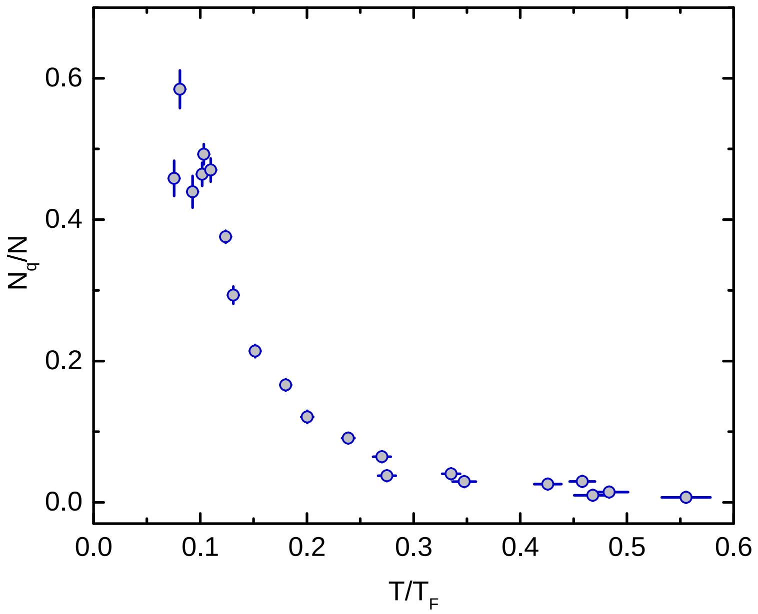

Figure 5.7.: Non-thermal fraction N_q/N as a function of T/T_F at $\ln(k_F a_{2D}) \approx -0.59$ (782 G). At low temperatures, N_q/N rapidly decreases. For higher temperatures, the decrease becomes slow. Only for $T/T_F \gtrsim 0.5$, N_q/N goes to zero. Each data point is the average of approximately 30 individual measurements, error bars denote the SEM.

rapidly. Then, the decrease becomes considerably slower around $T/T_F \approx 0.2$. N_q/N tends to zero only for $T/T_F \gtrsim 0.5$. It is important to note that in the high temperature regime the non-thermal fraction does not manifest itself in a sharp low-momentum peak. Instead, the momentum distribution deviates smoothly from the thermal behavior for a wide range of low momenta. This can be seen in figure 5.8. This behavior was predicted to occur in the weakly interacting 2D Bose gas above the superfluid transition temperature T_c [Pro01, Pro02, Bis09]. It was experimentally validated in [Cla09, Tun10, Pli11, Hun11] for the interacting Bose gas. This presuperfluid increase of low momentum density makes it difficult to determine T_c from the non-thermal fraction. We thus extract T_c from the peak momentum density. This is described in the next chapter.

5.3. Critical Temperature

Due to the smooth presuperfluid increase of low-momentum density described in the last chapter, the non-thermal fraction of the momentum distribution is not

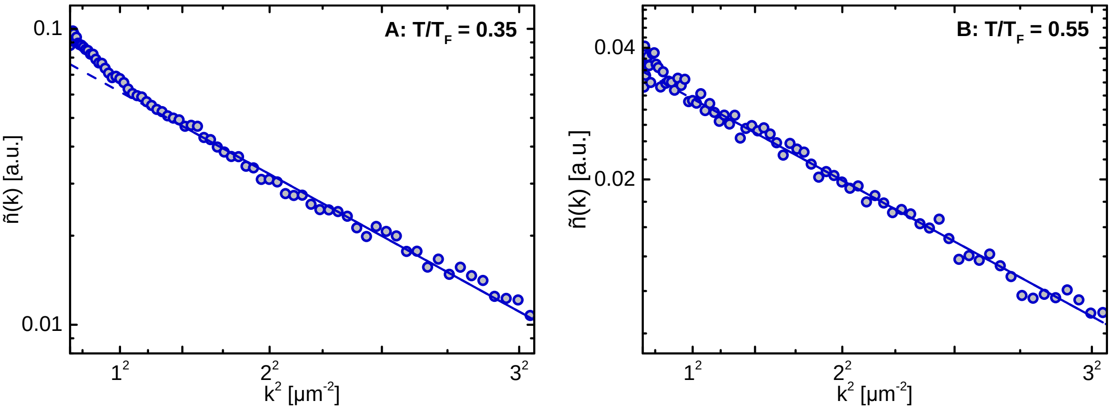

Figure 5.8.: Pair momentum density as a function of the momentum at high temperatures. In contrast to lower temperatures (see figure 5.4), there is no sharp low-momentum peak. Instead, there is a smooth increase of the low-momentum density at intermediate temperatures like $T/T_F \approx 0.35$ (A), which leads to a non-thermal fraction of $N_q/N \approx 3\,\%$. Only at the highest investigated temperatures of $T/T_F \approx 0.55$, N_q/N vanishes and the momentum distribution becomes purely Gaussian. Data points are the average of approximately 30 azimuthally averaged measurements. The solid part of the fit curve indicates the fit range.

a suitable parameter to extract the superfluid transition temperature T_c. Much rather, the peak momentum density, i.e. the height of the condensate peak, should be used: it is a measure for the number of atoms in the lowest momentum states, which is equivalent to the number of atoms in a long-range coherent state.

To get a feeling for the long-range coherence of the gas, we estimate the fraction of atoms in the long-range coherent phase similarly to [Pli11]. We calculate the fraction of the gas with a coherence length larger than $\ell_{coh} \geq 12.5\,\mu\text{m} \gg \lambda_{dB}$. It corresponds to the fraction of the momentum density within the innermost two pixels of the radial momentum distribution. At the lowest temperature at $\ln(k_F a_{2D}) = (B = 782\,\text{G})$, where we observe the highest low-momentum peak, this fraction is approximately $3.5\,\%$. Thus, a significant fraction of the gas has a correlation length which is clearly larger than thermal length scales.

For the determination of the critical temperature, we obtain the peak momentum density $\tilde{n}_0$ from the momentum distribution by fitting the inner $10-15$ pixels with a Gaussian. For the fit, we omit the innermost pixel since its fluctuations are not evened out in the azimuthal averaging process. Although the condensate peak is not expected to have a Gaussian momentum profile, this phenomenological fit to a small number of data points describes the tip of the low momentum peak well.

We normalize $\tilde{n}_0$ by the in-situ peak density n_0 and plot $\tilde{n}_0/n_0$ as a function of the degeneracy temperature. This is shown in figure 5.9 for a magnetic offset field of 782 G ($\ln(k_F a_{2D}) \approx -0.7$). One can clearly distinguish between two regimes: for high temperatures, the normalized peak density is small and almost constant, whereas it rapidly increases with falling temperature in the low temperature regime. We interpret this behavior as a signature of the phase transition.

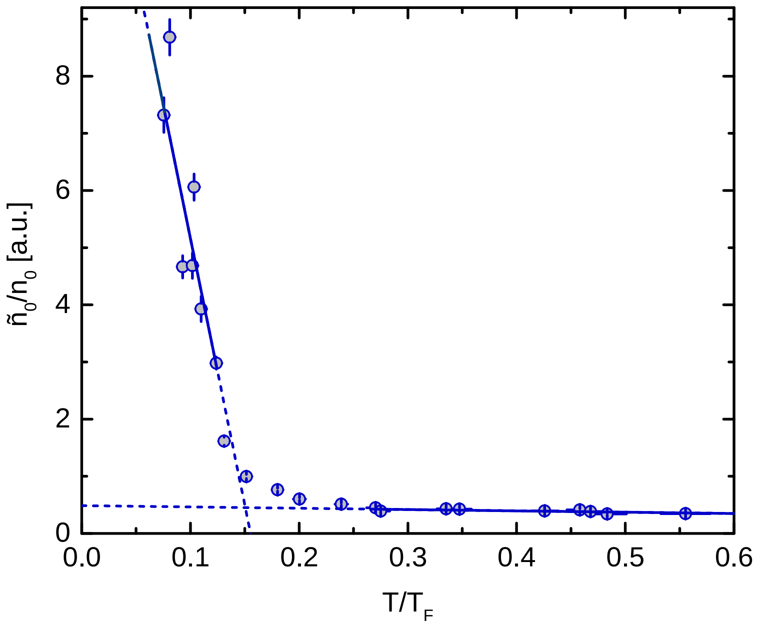

Figure 5.9.: Normalized peak momentum density $\tilde{n}_0/n_0$ as a function of the degeneracy temperature T/T_F at $B = 782\,\mathrm{G}$ ($\ln(k_F a_{2D}) \approx -0.7$). At low temperatures, $\tilde{n}_0/n_0$ decreases rapidly with temperature. At high temperatures, $\tilde{n}_0/n_0$ is small and roughly constant. The transition temperature T_c can be extracted from the intersection of linear fits to the two regimes. Each data point is the average of approximately 30 individual measurements, error bars denote the SEM. The solid part of the fit curves indicates the fit range.

Both regimes in figure 5.9 are well described by linear functions. We thus interpret the intersection of the linear fits to each regime as the transition temperature T_c/T_F. The statistical error of T_c/T_F is given by the standard errors of the two linear fits.

For interaction strengths below $\ln(k_F a_{2D}) \leq 1.8$ ($B \leq 852\,\mathrm{G}$), the low-momentum peak is sufficiently pronounced and we can determine T_c/T_F. Further towards the

BCS side, T_c/T_F lies below the lowest attainable temperature. Here, we can only give our lowest attainable temperature as an upper bound for T_c/T_F. The obtained critical temperatures and can be found in table A.1 in the appendix.

5.4. Phase Diagram

To obtain the phase diagram of the 2D Fermi gas in the BEC-BCS crossover, we combine the data obtained from the previously described analyses for all investigated temperatures and interaction strengths. The result is shown in figure 5.10. We plot the non-thermal fraction N_q/N as a color scale as a function of the degeneracy temperature T/T_F and the interaction parameter $\ln(k_F a_{2D})$. Gray circles denote our data points, between which we interpolate the color scale linearly. Additionally, we plot the transition degeneracy temperature T_c/T_F as a function of $\ln(k_F a_{2D})$ as black points with their statistical errors. The dashed connections between these points are a guide to the eye. Gray areas indicate experimentally inaccessible regions. The theoretical predictions for T_c/T_F according to equation (2.52) in the BEC regime and equation (2.53) and (2.54) in the BCS regime are shown as white dashed and dotted lines (compare also to the predicted phase diagram in figure 2.6). Numbers for the critical temperature including all statistical and systematic errors can also be found in table A.1 in the appendix.

Looking at the phase diagram, one first notices that the lowest attainable degeneracy temperature T/T_F on the BCS side is higher than on the BEC side by almost a factor of 4. This is mainly due to the decrease of the density and thus the Fermi temperature T_F between the BEC- and the BCS regime (see chapter 5.1). The lowest attainable absolute temperature only changes weakly with the interaction strength and lies at approximately 65 nK.

Comparing the critical degeneracy temperature T_c/T_F to the non-thermal fraction N_q/N, one observes that the phase transition always occurs at $N_q/N \approx 30\,\%$. This is well above of what can be explained by Bose enhancement. The presuperfluid increase of low momentum density thus involves a significant fraction of the sample for all interaction strengths.

In the BEC limit of the phase diagram ($\ln(k_F a_{2D}) \approx -7.3$, $B = 692\,\mathrm{G}$), the critical temperature is $T_c/T_F = 0.104 \pm 0.017$. This corresponds to a critical phase space density of $\rho_c = n_0 \lambda_{dB} = 4.82 \pm 0.79$. With increasing magnetic field, T_c/T_F slowly increases towards the crossover. This behavior is in agreement with the bosonic theory given by equation (2.52) [Pet03]. Although the values are consistent with the prediction within their systematic uncertainty (not shown in figure 5.10, see chapter A.3), the measured critical temperature systematically lies above the prediction.

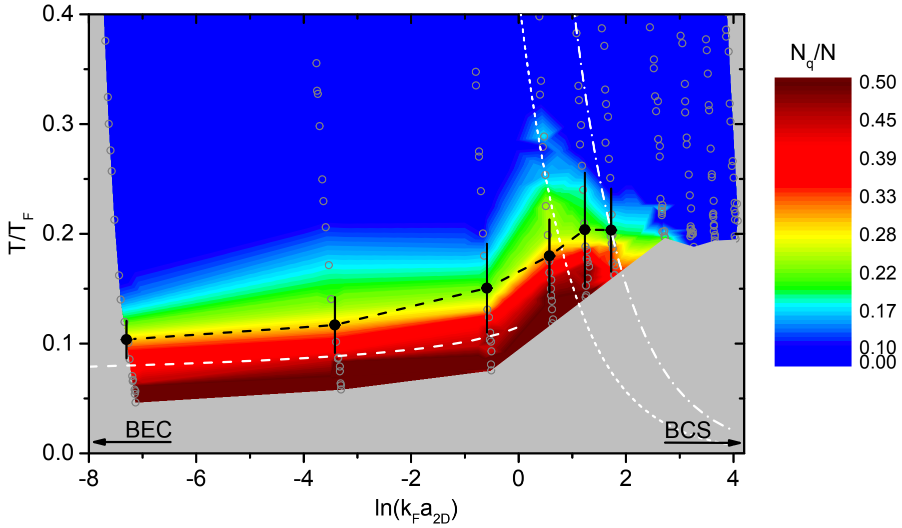

Figure 5.10.: Phase diagram of the 2D Fermi gas in the BEC-BCS crossover. The non-thermal fraction N_q/N is depicted as a color scale, measured data points are gray open circles. The critical temperature T_c/T_F with its statistical errors is represented by black points. Theoretical predictions for T_c/T_F according to bosonic theory (equation (2.52)) correspond to the white dashed line, those according to BCS theory without (equation (2.53)) and with GMB correction (equation (2.54)) correspond to the white dash-dotted and dotted line, respectively.

The theory curve reproduces the qualitative behavior of the critical temperature well even in the strongly interacting regime up to $\ln(k_F a_{2D}) = 0$. This is remarkable, since the theory assumes an interacting Bose gas. It might thus indicate that the gas has a bosonic character up to $\ln(k_F a_{2D}) = 0$. This should be seen in connection with the behavior of the degeneracy temperature, which exhibits a steep increase centered around $\ln(k_F a_{2D}) \approx 1$ while being almost constant in the bosonic and fermionic limits (see figure 5.6). Together, these two observations indicate that the crossover should happen at small positive $\ln(k_F a_{2D})$ rather than around $\ln(k_F a_{2D}) = 0$. This contradicts results which see the crossover centered around $\ln(k_F a_{2D}) = 0$. However, it is in agreement with quantum Monte-Carlo calculations [Ber11, Nga13, Lev14], which predict the crossover to happen on the BCS side of the resonance around $\ln(k_F a_{2D}) \approx 0.5$ (see chapter 2.3.4). Intuitively, the shifted crossover point can be understood by looking at the binding energy of the universal dimer (see figure 2.4). Unlike in 3D, the dimer does not become unbound on resonance even in the two-body picture.[3] Since it has a considerable binding energy at $\ln(k_F a_{2D}) = 0$, the gas still consists of molecules at the investigated temperatures and can thus be described by bosonic theory.

In the crossover region, the critical temperature increases and reaches its maximum between $\ln(k_F a_{2D}) \approx 1.2 - 1.7$ ($B = 832 - 852\,\mathrm{G}$), at a degeneracy temperature of $T_c/T_F \approx 0.2$.[4] The maximum of the non-thermal fraction lies at $\ln(k_F a_{2D}) \approx 0.5$.

Further on the BCS side, BCS theory predicts an exponential decay of T_c/T_F with $\ln(k_F a_{2D})$ as shown in equations (2.53) and (2.54). Unfortunately, we do not achieve sufficiently low degeneracy temperatures in this regime to observe the phase transition. For $\ln(k_F a_{2D}) \gtrsim 2$, we can thus only give an upper limit of $T_c/T_F \lesssim 0.2$. However, the behavior of the non-thermal fraction suggests a decrease of T_c/T_F with $\ln(k_F a_{2D})$ on the BCS side of the resonance.

The theoretical predictions for T_c/T_F from BCS theory without and with the GMB correction for particle hole fluctuations around the Fermi surface (see equations (2.53) and (2.54)) lie below the experimental data. It is worth noting that in this regime, a Boltzmann fit to the in-situ distributions seems to yield lower temperatures. However, it only uses a small part of the distribution at the edge of the trap, and is heavily dependent on the fit range as well as on the assumed potential shape. Furthermore, the uncertainty due to noise in this low-density region is large. Within these uncertainties, the thus extracted temperatures agree with those obtained from the momentum distribution.

The deviation of our data from the theory curve might be partially due to a possible breakdown of BCS theory in the strongly interacting regime. Additionally, it also hints towards the already mentioned increase of T_c/T_F in the quasi-2D geometry. This should be clarified in future experiments, where T_c/T_F could be measured as a function of the atom number and thus the population of axially excited motional levels.

In conclusion, the measured phase diagram shows the transition into a long-range coherent phase across the 2D BEC-BCS crossover. The observed transition temperatures and features like the presuperfluid increase of the non-thermal fraction suggest that this is the BKT transition into the predicted QLRO superfluid phase. However, to truly confirm the character of the transition, an analysis of the coherence in the condensed phase is necessary. This analysis is described in the next chapter.

---

[3] In the presence of a surrounding gas, even the 3D dimer only becomes unbound above the resonance, see [Zwi04].

[4] The exact numbers are given in table A.1 in the appendix.

5.5. Coherence Properties

In order to verify the character of the observed transition, we probe the coherence properties of the gas. We do this in two independent ways. In the first measurement, we let the sample interfere with itself with the help of a short time-of-flight evolution. Thus, we make areas of coherent phase visible. In the second measurement, we Fourier transform the momentum distribution and thus obtain a trap average of the first order correlation function $g_1(\mathbf{r_0} + \mathbf{r}, \mathbf{r_0})$. Below the critical temperature, we observe an algebraic decay of correlations which is in qualitative agreement with the predictions for a homogeneous 2D system.

5.5.1. Self-Interference

To probe the coherence properties of the gas by means of self-interference, we release the gas from the optical SWT and let it evolve in time-of-flight for 4 ms. This time is sufficiently short that the obtained distribution in the radial plane is dominated by the initial spatial distribution rather than by the momentum distribution. During the time-of-flight, phase fluctuations in the gas are transformed into density fluctuations due to self-interference [Ima09].

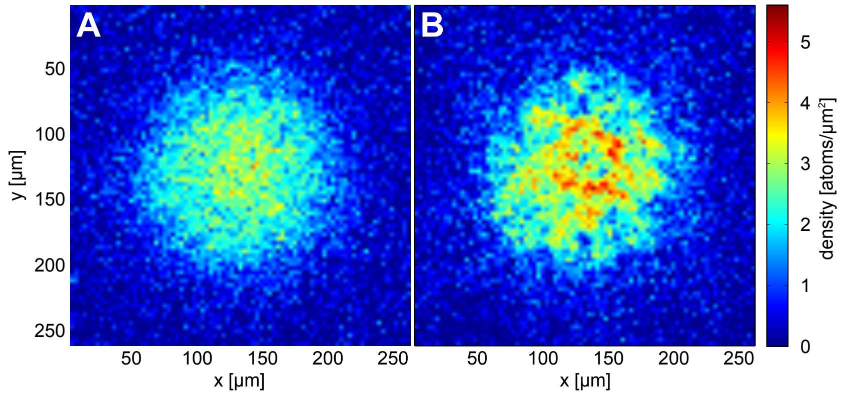

Figure 5.11.: In-situ density distribution (A) and density distribution after 4 ms time-of-flight (B). In-situ, the sample does not exhibit long-range density fluctuations. After the short time-of-flight, initial phase fluctuations are mapped onto density fluctuations due to self-interference in the sample. The resulting distribution shows randomly distributed macroscopic areas of high and low density. They correspond to areas of coherent phase in the initial sample and are thus a signature of quasi long-range order. Each image is the result of one individual measurement.

The results of such a measurement are shown in figure 5.11 for the coldest attainable temperature at $\ln(k_F a_{2D}) = -7.13$ ($B = 692\,\mathrm{G}$). Figure 5.11 (A) shows the smooth density distribution before the time-of-flight evolution. Here, density fluctuations are suppressed due to the interactions in the gas. Figure 5.11 (B) shows the density distribution after short time-of-flight. It exhibits strong density modulations, which form a pattern of randomly distributed areas of high and low density. The size of the largest areas is on the order of few $10\,\mu$m, which is an order of magnitude larger than the thermal de-Broglie wavelength $\lambda_{dB} \approx 2\,\mu$m. At the same time, the areas are approximately an order of magnitude smaller than the size of the sample. They are thus a signature of coherence on finite length scales much larger than expected for a thermal gas.

In order to confirm the true randomness of the observed modulation pattern, we average approximately 30 individual images taken at the same experimental parameters. The resulting averaged distribution shows a smooth atom cloud with no internal structure.

Below the critical temperature, we observe similar behavior for all investigated interaction strengths. Above T_c, the large length scale fluctuations vanish. For large $\ln(k_F a_{2D})$, the modulation amplitude seems to decrease. However, here the density of the gas is reduced by more than a factor of 3 (see figure 5.1), and the observation of the fluctuations becomes difficult due to the reduced signal-to-noise ratio. Thus, we do not perform a quantitative evaluation across the whole phase diagram.

The observation of finite range coherence well below the critical temperature rules out the presence of true long-range order (TLRO) in the condensed phase. Thus, the observed transition cannot be Bose-Einstein condensation. At the same time, the existence of coherent areas of random size significantly larger than λ_{dB} is a strong indication for quasi long-range order (QLRO), as predicted for the superfluid phase in a 2D gas. In combination with the measured phase diagram, this measurement is thus a strong piece of evidence that the observed condensation is the predicted BKT transition.

In principle, it is possible to obtain quantitative information about the phase correlations in the gas with the help of the density-density correlation function

$$g_2(\mathbf{r_1}, \mathbf{r_2}) = \frac{\langle n_{2D}(\mathbf{r_1}) n_{2D}(\mathbf{r_2}) \rangle}{\langle n_{2D}(\mathbf{r_1}) \rangle \langle n_{2D}(\mathbf{r_2}) \rangle} \quad . \tag{5.3}$$

Here, n_{2D} stands for the 2D density after the short time-of-flight, and $\langle\ \rangle$ denotes the average of the respective quantity.

By comparing the experimentally obtained $g_2(\mathbf{r_1}, \mathbf{r_2})$ with the results of a simulation [Sin14], we tried to verify the expected algebraic decay of the first order correlation function g_1 (see equation (2.42)) and obtain its scaling exponent η. However, the comparison of the inhomogeneous, harmonically trapped gas and the homogeneous simulations is difficult [Pre14]. To minimize the influence of the trap on the phase space density and thus the coherence properties of the gas, we only analyzed a circle with a radius of 8 pixels in the center of the trap. Within this circle, the average 2D density changes by less than 10 %. Thus, the deviation from the homogeneous system should be small.

However, the small analyzed area also leads to a bad signal-to-noise ratio. Additionally, it was found in previous publications that the observed density modulation is very sensitive to small imaging artifacts. In particular, effects like defocussing [Cho12, Lan13] or the deviation from the atomic transition frequency can strongly alter the observed modulation. We were thus only able to qualitatively reproduce the predicted oscillatory behavior of $g_2(\mathbf{r_1}, \mathbf{r_2})$ [Sin14]. The extraction of quantitative information from the density modulation was not possible. Consequently, we use a different method to further investigate the correlations in the gas. This method is described in the following chapter.

5.5.2. Algebraic Decay of Correlations

In order to obtain further information about the correlations in our sample, we study its first order correlation function $g_1(\mathbf{r})$, which we obtain by means of a 2D Fourier transform of the 2D momentum distribution $\tilde{n}(k_x, k_y)$ (see chapter 2.3.3). The obtained correlation function $g_1(x, y)$ shows good radial symmetry, and we thus azimuthally average it to obtain the radial correlation function $g_1(r)$. It is shown for a sample at 692 G ($\ln(k_F a_{2D}) \approx -7.3$) at a low and a high temperature in figure 5.12.

The blue data points correspond to $T/T_F \approx 0.05$, where a large part of the sample is condensed into the superfluid phase. For radii between $r \geq 16\,\mu$m and $r \leq 90\,\mu$m, they clearly exhibit an algebraic decay $g_1(r) \propto r^{-\eta}$ as expected from BKT theory. We observe such an algebraic decay for all temperatures below T_c.

For the homogeneous case, one expects the exponent to be $\eta = 0.25$ at T_c and to go to zero as T goes to zero. However, the values we obtain for η lie between $\eta \approx 1$ at T_c and $\eta \approx 0.6$ at the lowest attainable temperature.

The observed correlations thus decay faster than expected for the homogeneous case. This might be due to the influence of the finite size harmonic trap, which introduces an additional length scale into the system. In addition, the measured momentum distribution is an average over the whole trap and thus the spatially varying phase space density of the gas. Thus, the g_1 correlation function we obtain from it also has to be interpreted as an average quantity.

A quantum Monte-Carlo simulation of our quasi-2D homogeneously trapped gas

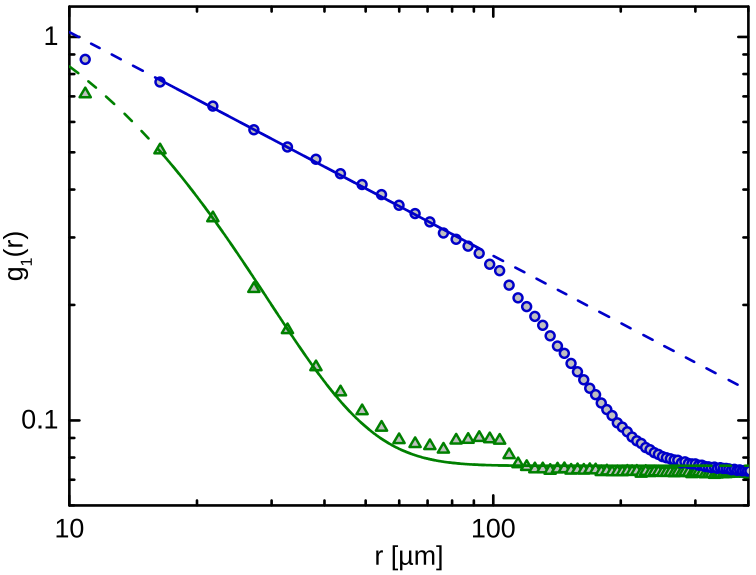

Figure 5.12.: Azimuthal average of correlation function $g_1(\mathbf{r})$ obtained from the 2D Fourier transform of the pair momentum distribution. The blue circles correspond to the lowest attainable temperature $T/T_F \approx 0.05$, well below T_c/T_F. An algebraic fit to the data (blue line) yields a characteristic exponent of $\eta = 0.6 \pm 0.009$. The green triangles correspond to $T/T_F \approx 0.11$, just above T_c/T_F. Here, the correlations can be described by an exponential decay with a decay length of $10.4 \pm 0.3\,\mu$m. The cutoff of the data at $r \geq 100\,\mu$m is due to the finite size of the sample, the finite value at large radii is due to noise. Each data point is the average of approximately 30 individual measurements. The solid part of the fit curves indicates the fit range.

[Hol14] reproduces the high characteristic exponents found in the experimental data. While the quantitative behavior of the observed correlations still needs further analysis, we are thus optimistic that it can be understood.

The green data points were taken slightly above the critical temperature at $T/T_F \approx 0.11$. They do not exhibit an algebraic decay, but can be described by an exponential decay as expected for a non-condensed gas in the degenerate regime [Had11]. The feature around $r \approx 100\,\mu$m is caused by a fringe in the absorption image. We observe a similar behavior for all temperatures above T_c. As the temperature approaches T_c from above, the correlation length increases. At T_c, the correlations change from exponential to algebraic.

In summary, the extracted correlations only match the expectations for a homogeneous gas qualitatively. Still, the phase transition between the algebraically decaying superfluid phase and the exponentially decaying non-condensed phase is clearly visible in this analysis. This observation thus confirms the BKT character of the observed phase transition. In addition, it also confirms the critical temperature T_c/T_F obtained from the rapid increase of the low-momentum density.

6. Conclusion and Outlook

In the course of this thesis, we designed and built an apparatus which enables us to create and probe a quasi two-dimensional strongly interacting Fermi gas of ultracold atoms. In addition to the density distribution of the gas, which we obtain from absorption imaging, we can access its momentum distribution. We do this by means of a matter-wave focusing technique: we let the gas evolve in a weak harmonic potential, until the initial momentum of each particle has been mapped to its position after a quarter of the potential's oscillation period. In combination with a projection of atom pairs onto deeply bound molecules, which removes the relative momentum of the atoms in the pair, this technique yields the pair momentum distribution.

The coherence properties of the gas are encoded in its momentum distribution. A purely thermal gas without long-range coherence follows a Boltzmann momentum distribution. In contrast, long-range coherence corresponds to an enhanced low-momentum density.

At sufficiently low temperatures, we find a strong enhancement of low momenta, which manifests itself in a sharp peak in the center of the momentum distribution. We extract the non-thermal fraction and the temperature of the gas from a Boltzmann fit to the thermal wings of the momentum distribution. We identify the critical temperature T_c of the observed transition with the temperature where the low-momentum peak forms.

By tuning the temperature and the interaction strength of the gas, we measure its phase diagram across the BEC-BCS crossover. We map it onto homogeneous theory by applying local density approximation at the trap center. The phase diagram shows condensation into the long-range ordered phase both on the bosonic and on the fermionic side of the crossover. The critical temperature ranges from $T_c/T_F \approx 0.1$ in the bosonic regime up to $T_c/T_F \approx 0.2$ in the strongly interacting limit.

We compare the measured critical temperature with the predictions for the Berezinskii-Kosterlitz-Thouless (BKT) transition. The measured T_c agrees with bosonic theory within our errors in the strongly interacting regime on the BEC side. In the strongly interacting regime on the BCS side, the measured T_c lies above the predictions. This deviation might be due to a possible breakdown of BCS theory in the strongly interacting regime. However, it might also indicate an increase of the critical temperature due to the influence of the third dimension in our quasi-2D system, which has been recently predicted [Fis14].

To investigate the coherence properties of the condensed phase, we perform a self-interference measurement with the gas, where we observe macroscopic density modulations below T_c. They correspond to modulations of the initial phase of the sample on length scales above the thermal wavelength and below the system size. This observation is a signature of the expected quasi long-range character of correlations in the condensed phase.

For a more quantitative investigation of the coherence properties, we analyze the Fourier transformation of the momentum distribution, which yields the trap averaged first-order correlation function $g_1(r)$. Below T_c, it exhibits an algebraic decay of correlations with r. This algebraic decay is expected for the superfluid phase in a homogeneous 2D gas. However, the characteristic exponent of the algebraic decay is higher than predicted by homogeneous theory. This might be a feature of the trapped gas, and is reproduced in a quantum Monte-Carlo simulation of our system [Hol14].

The combination of our results yields strong evidence that we have observed the BKT transition into the quasi long-range phase coherent 2D superfluid phase in the strongly interacting 2D Fermi gas.

In addition to the analysis presented in this thesis, we are currently working on the extraction of the equation of state $n_{2D}(\mu, T, \ln(k_F a_{2D}))$ from our data in collaboration with our theory partners. We obtain the 2D density $n_{2D}(\mathbf{r}, T, \ln(k_F a_{2D}))$ from the measured in-situ data as a function of the the position $\mathbf{r}$, the temperature T, and the interaction strength $\ln(k_F a_{2D})$. By applying local density approximation, we want to obtain $\mu(\mathbf{r}) = \mu_0 - V(\mathbf{r})$ and thus the equation of state. To map out $V(\mathbf{r})$, we plan to use data taken in the weakly interacting Fermi regime, where the equation of state can be computed. Whereas the extraction of μ_0 from the in-situ data is complicated, it should be possible to obtain it from the Gaussian decay of the momentum distribution on long length scales.

For the 3D Fermi gas, similar measurements have been described in [Nas10, Ku12]. In the 2D Fermi gas in the BEC-BCS crossover, the pressure of the gas in the trap center has been measured as a function of $\ln(k_F a_{2D})$ [Mak14].

The superfluidity of the observed condensed phase has not yet been directly confirmed in the strongly interacting 2D Fermi gas. Similar to experiments in the 3D Fermi gas [Zwi05, Wei14] or the 2D Bose gas [Des12], this could be done by stirring the condensed gas and observing the formation of quantized vortices, or the existence of a critical velocity below which the gas cannot be excited.

Furthermore, it would be interesting to measure the behavior of T_c in the dimensional crossover from 2D to 3D. The predicted increased critical temperature in this regime [Fis14] might help explain the observed high T_c in layered superconductors, where the electron gas is confined in quasi two-dimensional planes [Nor11, Jos13].

As mentioned in chapter 3, we included a 2D optical lattice into the setup in addition to the standing wave trap (SWT) used for the experiments presented here. We already tested the lattice setup by Kapitza-Dirac scattering of atoms on the optical potential [Bec13] and by loading atoms into it. We are currently working on the creation of a sample in a single layer egg-crate shaped lattice by combining the 2D lattice with a single layer of the SWT. Starting with a 2D superfluid of deeply bound molecules in the SWT and slowly ramping on the 2D lattice, we should be able to continuously drive the system into a Mott insulating state of molecules. The 2D geometry should enable the in-situ observation of the Mott insulator, similar to the bosonic case [Gem09, Bak10, She10].

By dissociating the molecules with a magnetic field ramp to the fermionic side, we should be able to prepare a fermionic band insulator, where each lattice site is filled with one atom in each of the two spin states. To obtain a fermionic metal or Mott insulator, one has to prepare a state with one atom per spin state, corresponding to half filling of the conductance band. This should be possible with the help of a dynamic lattice, where it is possible to merge and split lattice sites. In such a lattice, we could prepare a molecular Mott insulator, where each lattice site is populated by a diatomic molecule. By adiabatically splitting each lattice site into two separate sites at repulsive interactions [Mur14a], it should be possible to create a low entropy fermionic Mott insulator with one single atom per site. Furthermore, in the presence of tunneling between the sites a macroscopically entangled antiferromagnetically ordered state should form.

To create such a dynamic lattice, we are currently working on the realization of arbitrary optical potentials with the help of a spatial light modulator (SLM). In combination with a high resolution objective [Ser11], it will enable us to create single-site resolved optical lattices of various geometries which can be changed dynamically during the experiment, as well as arbitrary non-periodic structures. In addition to the mentioned preparation scheme for antiferromagnetic order, the SLM will allow us to test lattice cooling techniques [McK11], which might offer an alternative way to reach very low entropies.

Another goal for our apparatus is the preparation of a three-component Fermi gas in the optical lattice. ^{6}Li provides three experimentally accessible Zeeman sublevels (see figure 2.2). Due to the overlapping broad Feshbach resonances between these three components [Zür13], it is possible to create a three-component sample with nearly symmetric interactions. Unlike a two-component Fermi gas, where inelastic collisions are kinematically forbidden, such a three-component Fermi gas is unstable in free space due to three-body recombination, which is resonantly enhanced by the Efimov effect [Efi70, Ott08]. To probe the properties of the gas beyond this three-body loss, it has been proposed to stabilize it using quantum Zeno loss blocking in a periodic potential [Kan09]. This effect has been verified experimentally in [Sya08, Yan13]. In such a stabilized three-component Fermi gas, we will be able to study exotic states of matter such as the so-called atomic color-superfluid [Rap07, Wil07, Pri11]. Here, two components of the gas form pairs, while the third component remains free. Such experiments could be useful to gain insight into quantum chromodynamics.

In summary, the flexibility of our experimental apparatus will allow for the realization and investigation of a large class of different systems, which will lead to insights into various fields of physics.

A. Appendix

A.1. Measured Critical Temperatures

B [Gauss]	ℓ_z/a	$\ln(k_F a_{2D})$ (stat.)(sys.)	T_c/T_F (stat.)(sys.)
692	7.11	-7.30 (4) $\binom{+4}{-5}$	0.104 (17) $\binom{+21}{-19}$
732	3.98	-3.42 (2) $\binom{+4}{-6}$	0.117 (25) $\binom{+25}{-22}$
782	1.55	-0.59 (1) $\binom{+4}{-7}$	0.151 (40) $\binom{+33}{-27}$
812	0.55	0.57 (1) $\binom{+2}{-7}$	0.180 (33) $\binom{+65}{-36}$
832	0	1.23 (1) $\binom{+2}{-8}$	0.204 (52) $\binom{+64}{-48}$
852	-0.46	1.72 (1) $\binom{+2}{-9}$	0.203 (38) $\binom{+57}{-36}$
892	-1.22	2.73 (1) $\binom{+2}{-9}$	< 0.196 (10) $\binom{+47}{-31}$
922	-1.67	3.24 (1) $\binom{+2}{-9}$	< 0.202 (11) $\binom{+51}{-31}$
952	-2.04	3.65 (1) $\binom{+2}{-10}$	< 0.194 (07) $\binom{+53}{-30}$
982	-2.35	4.08 (1) $\binom{+2}{-10}$	< 0.212 (15) $\binom{+55}{-33}$

Table A.1.: Measured parameters as a function of the magnetic offset field B. The interaction parameters ℓ_z/a and $\ln(k_F a_{2D})$ as well as the obtained critical temperature T_c/T_F are given. Since $\ln(k_F a_{2D})$ is temperature dependent, the given value corresponds to that at T_c/T_F where we observed the phase transition. For magnetic fields above 852 G, the lowest attainable temperature is given as an upper bound for T_c/T_F, and $\ln(k_F a_{2D})$ corresponds to that temperature. Statistical errors are standard errors of the mean, systematic errors are calculated as explained in chapter A.3.

A.2. Binding Energy of the Universal Dimer

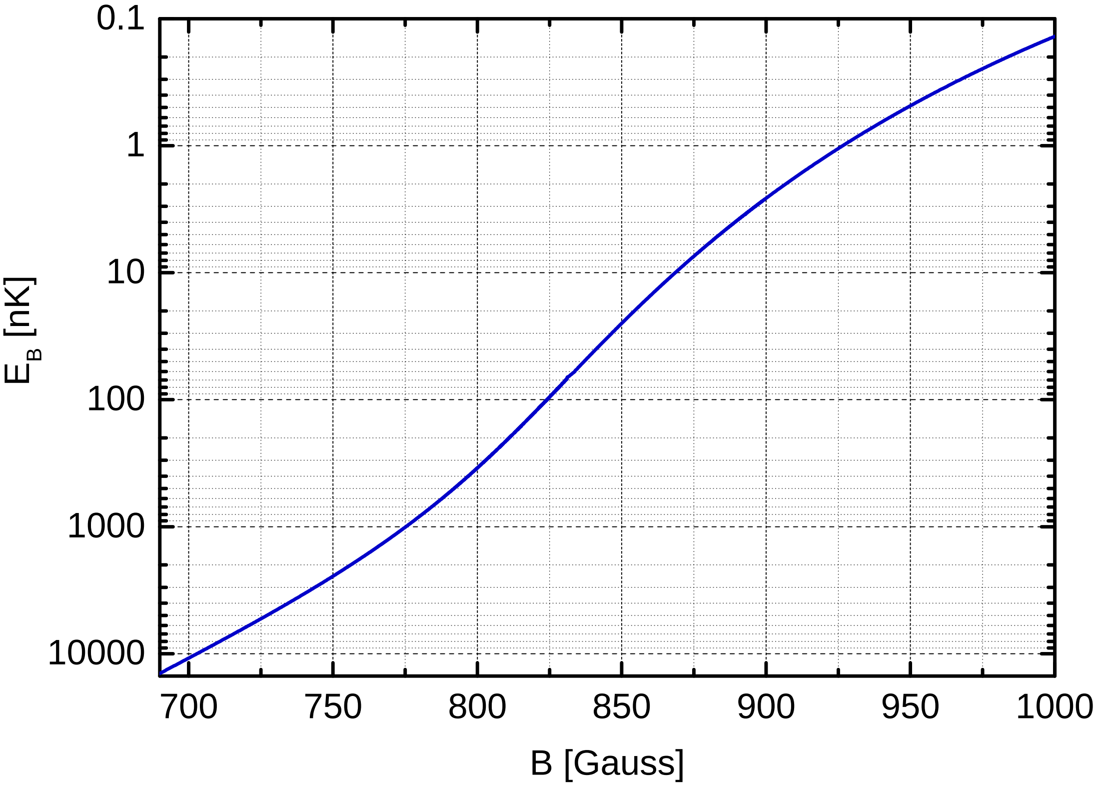

Figure A.1.: Binding energy of the two-body bound state for typical parameters in our experiment. The values are calculated according to equation (2.23), with $\ell_z = 551.2\,\mathrm{nm}$. This corresponds to the SWT depth of approximately 500 nK at which all experiments were conducted.

A.3. Systematic Uncertainties

In the previous chapters, only the statistical errors of the measured quantities were given. However, there are several effects which lead to systematic uncertainties in our measurements. The systematic uncertainties arising from different sources were discussed in the respective chapters. Here, their influence on the measured quantities is summarized. This chapter was previously published in [Rie14].

- **Trap frequency of the expansion potential** (see chapter 3.4.1):
  We measure the trap frequency of the expansion potential ω_{exp} with a relative uncertainty of approximately 3%. This leads to an uncertainty of 6% in the fitted temperature T according to equation (5.1).

- **Magnification of the imaging system** (see chapter 3.5):
  We calibrate the magnification of the imaging system using Kapitza-Dirac scattering of atoms on the optical lattice potential. The resulting uncertainty in the magnification is approximately 6.5%. This uncertainty quadratically enters the temperature obtained from the fit with equation (5.1). Thus, T has a relative systematic uncertainty of approximately 13%.

- **Atoms in non-central pancakes** (see chapter 4.2.2):
  From the tomographic measurement of the distribution of the gas over the SWT layers, we obtain an upper bound of 11% for the fraction of atoms in the non-central layer. To estimate their influence on the measured peak density n_0, we assume that their temperature is not affected by the evaporative cooling in the SWT due to the small atom number. However, it is affected by the heating procedure where the depth of the trap is modulated. The minimum temperature of these atoms is thus about 100 nK, the temperature after the transfer into the SWT. Assuming a thermal Boltzmann gas, we calculate the density of 5500 atoms in the two non-central layers to be $n_{0,\mathrm{nonc.}} = 0.14\,\mathrm{atoms}/\mu\mathrm{m}^2$ [Ket08]. This leads to an overestimation of T_F by 5% for the lowest magnetic fields, and 19% at the highest magnetic fields, where n_0 is smaller due to the fermionic character of the sample. Analogously, k_F is overestimated by 2.5% to 9.5%.

- **Imaging intensity $\boldsymbol{I_0/I_{sat}}$** (see chapter 4.5.2):
  The measured atom density depends on the intensity I_0/I_{sat} of the imaging beam (see equation (4.4)). We calibrate the imaging intensity to be $I_0/I^*_{sat} = 0.97^{+0.13}_{-0.08}$. This leads to an uncertainty in the peak density n_0 and thus we obtain $T_F\ ^{+7\%}_{-4\%}$ and $k_F\ ^{+3.5\%}_{-2\%}$. The same uncertainty applies to the peak momentum density $\tilde{n}_0$. It thus cancels in $\tilde{n}_0/n_0$.

- **Reduced absorption cross section of molecules** (see chapter 4.5.2):
A finite molecular binding energy leads to a reduced absorption cross section for the lowest three magnetic fields (692 G, 732 G and 782 G). The experimentally determined correction factor is given in table 4.1. By rescaling the obtained images with this factor, we compensate for this effect. The uncertainty in the rescaling factor leads to an uncertainty in the peak density n_0 and thus T_F which is smaller than 8%. The corresponding uncertainty in k_F is smaller than 4%.

- **Evolution time** (see chapter 4.6):
The measured momentum distribution depends on the evolution time in the harmonic radial potential. By measuring the temperature as a function of time-of-flight, we find a maximum for $t = T/4 = \pi/(2\omega_{\mathrm{ev}})$. Deviations from the ideal evolution time, which is slightly below 25 ms, lead to a systematic underestimation of T by approximately 5%. The peak momentum density $\tilde{n}_0$ is underestimated by a similar factor.

- **Fit range for temperature determination** (see chapter 5.2.1):
The temperature determined from the Boltzmann fit to the tail of the momentum distribution weakly depends on the region included in the fit. This leads to a relative uncertainty of 7% in T for low temperatures and up to 13% at the highest investigated temperatures. The same effect also leads to a systematic uncertainty in the determined non-thermal fraction N_q/N. The absolute uncertainty in N_q/N ranges from 0.06 at low temperatures to about 0.02 at high temperatures.

- **Temperature interpolation (812 G - 852 G)** (see chapter 5.2.1):
For the magnetic fields 812 G, 832 G, and 852 G, the thermal tail of the momentum distribution cannot be described by a pure molecular or atomic gas. This makes a temperature determination according to equation (5.1) impossible. Thus, the reduced temperature T/T_F is determined by linear interpolation between the values at 782 G and 892 G for each heating strength. The boundaries for the resulting values are estimated assuming that T/T_F behaves monotonously with $\ln(k_F a_{2D})$ and that T/T_F must lie between the values obtained assuming a purely atomic or molecular sample. The obtained relative uncertainties are biggest for small temperatures. They are usually on the order of 10%-25% and range up to 50% for few individual values.

Resulting total systematic uncertainties: Assuming a Gaussian distribution of the previously mentioned 8 independent error sources, we calculate the total relative systematic uncertainty of T/T_F. For magnetic fields where the temperature is not interpolated, we obtain $T/T_F{}^{+29\%}_{-28\%}$ for low temperatures and low magnetic fields to $T/T_F{}^{+38\%}_{-29\%}$ at high temperatures and high magnetic fields. At the magnetic fields where the temperature is determined by interpolation, the systematic uncertainties are significantly bigger and one obtains approximately $T/T_F{}^{+50\%}_{-35\%}$ at low temperatures and $T/T_F{}^{+35\%}_{-32\%}$ at high temperatures.

The systematic uncertainty in $\ln(k_F a_{2D})$ is dominated by the uncertainties in k_F. We thus neglect uncertainties in a_{2D}. The total absolute systematic uncertainty then lies between $\ln(k_F a_{2D})^{+0.07}_{-0.08}$ for low magnetic fields and $\ln(k_F a_{2D})^{+0.07}_{-0.12}$ for high magnetic fields. The systematic uncertainties of T/T_F and $\ln(k_F a_{2D})$ at the critical temperature T_c are listed in table A.1.

Bibliography

[Abe04] E. Abers, *Quantum Mechanics* (Pearson Education, 2004).

[Amm97] H. Ammann, N. Christensen, *Delta Kick Cooling: A New Method for Cooling Atoms*, Phys. Rev. Lett. **78**, 2088–2091 (Mar 1997).

[And95] M. H. Anderson, J. R. Ensher, M. R. Matthews, C. E. Wieman, E. A. Cornell, *Observation of Bose-Einstein Condensation in a Dilute Atomic Vapor*, Science **269**, 198–201 (1995).

[Bak10] W. S. Bakr, A. Peng, M. E. Tai, R. Ma, J. Simon, J. I. Gillen, S. Fölling, L. Pollet, M. Greiner, *Probing the Superfluid-to-Mott Insulator Transition at the Single-Atom Level*, Science **329**, 547–550 (2010).

[Bar57] J. Bardeen, L. N. Cooper, J. R. Schrieffer, *Microscopic Theory of Superconductivity*, Phys. Rev. **106**(1), 162–164 (Apr 1957).

[Bar04] M. Bartenstein, A. Altmeyer, S. Riedl, S. Jochim, C. Chin, J. H. Denschlag, R. Grimm, *Crossover from a molecular Bose-Einstein condensate to a Degenerate Fermi Gas*, Phys. Rev. Lett. **92**, 120401 (2004).

[Bau12] S. K. Baur, B. Fröhlich, M. Feld, E. Vogt, D. Pertot, M. Koschorreck, M. Köhl, *Radio-frequency spectra of Feshbach molecules in quasi-two-dimensional geometries*, Phys. Rev. A **85**, 061604 (Jun 2012).

[Bau14] M. Bauer, M. M. Parish, T. Enss, *Universal Equation of State and Pseudogap in the Two-Dimensional Fermi Gas*, Phys. Rev. Lett. **112**, 135302 (Apr 2014).

[Bec13] J. Becher, *A two dimensional optical lattice for ultracold fermions* (2013), Bachelor thesis, Ruprecht-Karls-Universität Heidelberg.

[Bed86] J. Bednorz, K. Müller, *Possible highT c superconductivity in the Ba-La-Cu-O system*, Zeitschrift für Physik B Condensed Matter **64**(2), 189–193 (1986).

[Ber72] V. L. Berezinskii, *Destruction of long-range order in one-dimensional and two-dimensional systems possessing a continuous symmetry group. II. Quantum systems*, Sov. Phys. JETP **34**, 610 (1972).

[Ber11] G. Bertaina, S. Giorgini, *BCS-BEC Crossover in a Two-Dimensional Fermi Gas*, Phys. Rev. Lett. **106**, 110403 (Mar 2011).

[Bis78] D. J. Bishop, J. D. Reppy, *Study of the Superfluid Transition in Two-Dimensional* ^{4}He *Films*, Phys. Rev. Lett. **40**, 1727–1730 (Jun 1978).

[Bis09] R. N. Bisset, M. J. Davis, T. P. Simula, P. B. Blakie, *Quasicondensation and coherence in the quasi-two-dimensional trapped Bose gas*, Phys. Rev. A **79**, 033626 (Mar 2009).

[Blo08] I. Bloch, J. Dalibard, W. Zwerger, *Many-body physics with ultracold gases*, Rev. Mod. Phys. **80**, 885 (2008).

[Blo12] I. Bloch, J. Dalibard, S. Nascimbene, *Quantum simulations with ultracold quantum gases*, Nat Phys **8**(4), 267–276 (April 2012).

[Bog60] N. Bogoliubov, *On some problems of the theory of superconductivity*, Physica **26**(Supplement), S1 – S16 (1960).

[Boh12] J. E. Bohn, *Towards an ultracold three-component Fermi Gas in a two-dimensional optical lattice* (2012), Diploma thesis, Ruprecht-Karls-Universität Heidelberg.

[Bot06] S. S. Botelho, C. A. R. Sá de Melo, *Vortex-Antivortex Lattice in Ultracold Fermionic Gases*, Phys. Rev. Lett. **96**, 040404 (Feb 2006).

[Bra09] E. Braaten, H.-W. Hammer, D. Kang, L. Platter, *Three-Body Recombination of* ^{6}Li *Atoms with Large Negative Scattering Lengths*, Phys. Rev. Lett. **103**, 073202 (Aug 2009).

[Bre31] G. Breit, I. I. Rabi, *Measurement of Nuclear Spin*, Phys. Rev. **38**(11), 2082–2083 (Dezember 1931).

[Bro23] L. de Broglie, *Waves and Quanta*, Nature (London) **112**, 540 (1923).

[Chi10] C. Chin, R. Grimm, P. Julienne, E. Tiesinga, *Feshbach resonances in ultracold gases*, Rev. Mod. Phys. **82**(2), 1225 (2010).

[Cho12] J.-y. Choi, S. W. Seo, W. J. Kwon, Y.-i. Shin, *Probing Phase Fluctuations in a 2D Degenerate Bose Gas by Free Expansion*, Phys. Rev. Lett. **109**, 125301 (2012).

[Cla08] B. E. Clancy, *Hydrodynamics of a Rotating Strongly Interacting Fermi Gas* (2008), PhD Thesis, Duke University.

[Cla09] P. Cladé, C. Ryu, A. Ramanathan, K. Helmerson, W. D. Phillips, *Observation of a 2D Bose Gas: From Thermal to Quasicondensate to Superfluid*, Phys. Rev. Lett. **102**, 170401 (2009).

[Dav95] K. B. Davis, M.-O. Mewes, M. R. Andrews, N. J. van Druten, D. S. Durfee, D. M. Kurn, W. Ketterle, *Bose-Einstein condensation in a gas of sodium atoms*, Phys. Rev. Lett. **75**(22), 3969–3973 (1995).

[Dem13] W. Demtröder, *Experimentalphysik 1*, Springer-Lehrbuch ; SpringerLink : Bücher (Springer, Berlin, Heidelberg, 2013), 6th Edn.

[Des12] R. Desbuquois, L. Chomaz, T. Yefsah, J. Leonard, J. Beugnon, C. Weitenberg, J. Dalibard, *Superfluid behaviour of a two-dimensional Bose gas*, Nature Physics **8**(9), 645 (2012).

[Dyk10] P. Dyke, *Quasi Two-Dimensional* ^{6}Li *Fermi Gas* (2010), PhD Thesis, Swinburne University of Technology.

[Dyk11] P. Dyke, E. D. Kuhnle, S. Whitlock, H. Hu, M. Mark, S. Hoinka, M. Lingham, P. Hannaford, C. J. Vale, *Crossover from 2D to 3D in a Weakly Interacting Fermi Gas*, Phys. Rev. Lett. **106**, 105304 (2011).

[Eag69] D. M. Eagles, *Possible Pairing without Superconductivity at Low Carrier Concentrations in Bulk and Thin-Film Superconducting Semiconductors*, Phys. Rev. **186**, 456–463 (1969).

[Efi70] V. Efimov, *Energy levels arising from resonant two-body forces in a three-body system*, Physics Letters B **33**, 563 – 564 (1970).

[Fel11] M. Feld, B. Fröhlich, E. Vogt, M. Koschorreck, M. Köhl, *Observation of a pairing pseudogap in a two-dimensional Fermi gas*, Nature **480**(7375), 75–78 (Dezember 2011).

[Fes58] H. Feshbach, *Unified theory of nuclear reactions*, Annals of Physics **5**(4), 357 – 390 (1958).

[Fey82] R. P. Feynman, *Simulating physics with computers*, International journal of theoretical physics **21**(6), 467–488 (1982).

[Fis14] A. M. Fischer, M. M. Parish, *Quasi-two-dimensional Fermi gases at finite temperature*, ArXiv e-prints (August 2014).

[Fli10] T. Fließbach, *Statistische Physik* (Spektrum Akademischer Verl., Heidelberg, 2010), 5th Edn.

[Fre01] D. L. Freimund, K. Aflatooni, H. Batelaan, *Observation of the Kapitza-Dirac effect*, Nature **413**(6852), 142–143 (September 2001).

[Fri00] N. Friedman, L. Khaykovich, R. Ozeri, N. Davidson, *Compression of cold atoms to very high densities in a rotating-beam blue-detuned optical trap*, Phys. Rev. A **61**, 031403 (Feb 2000).

[Frö11] B. Fröhlich, M. Feld, E. Vogt, M. Koschorreck, W. Zwerger, M. Köhl, *Radio-Frequency Spectroscopy of a Strongly Interacting Two-Dimensional Fermi Gas*, Phys. Rev. Lett. **106**, 105301 (2011).

[Frö12] B. Fröhlich, M. Feld, E. Vogt, M. Koschorreck, M. Köhl, C. Berthod, T. Giamarchi, *Two-Dimensional Fermi Liquid with Attractive Interactions*, Phys. Rev. Lett. **109**, 130403 (2012).

[Gem09] N. Gemelke, X. Zhang, C.-L. Hung, C. Chin, *In situ observation of incompressible Mott-insulating domains in ultracold atomic gases*, Nature **460**(7258), 995–998 (August 2009).

[Gio08] S. Giorgini, L. P. Pitaevskii, S. Stringari, *Theory of ultracold atomic Fermi gases*, Rev. Mod. Phys. **80**, 1215–1274 (Oct 2008).

[Gör01] A. Görlitz, J. M. Vogels, A. E. Leanhardt, C. Raman, T. L. Gustavson, J. R. Abo-Shaeer, A. P. Chikkatur, S. Gupta, S. Inouye, T. Rosenband, W. Ketterle, *Realization of Bose-Einstein Condensates in Lower Dimensions*, Phys. Rev. Lett. **87**, 130402 (Sep 2001).

[Gre03] M. Greiner, C. A. Regal, D. S. Jin, *Emergence of a molecular Bose-Einstein condensate from a Fermi gas*, Nature **426**, 537–540 (2003).

[Gri00] Rudolf Grimm, Matthias Weidemüller, Yurii B. Ovchinnikov, *Optical dipole traps for neutral atoms*, Adv. At. Mol. Opt. Phys. **Vol. 42**, 95–170 (2000).

[Gün05] K. Günter, T. Stöferle, H. Moritz, M. Köhl, T. Esslinger, *p-Wave Interactions in Low-Dimensional Fermionic Gases*, Phys. Rev. Lett. **95**, 230401 (Nov 2005).

[Had06] Z. Hadzibabic, P. Krüger, M. Cheneau, B. Battelier, J. Dalibard, *Berezinskii-Kosterlitz-Thouless crossover in a trapped atomic gas*, Nature **441**, 1118 (2006).

[Had11] Z. Hadzibabic, J. Dalibard, *Two-dimensional Bose fluids: An atomic physics perspective*, Rivista del Nuovo Cimento, vol. **34,**, pp.389–434 (2011).

[Hoh67] P. C. Hohenberg, *Existence of Long-Range Order in One and Two Dimensions*, Phys. Rev. **158**, 383 (1967).

[Hol07] M. Holzmann, G. Baym, J.-P. Blaizot, F. Laloë, *Superfluid transition of homogeneous and trapped two-dimensional Bose gases*, Proceedings of the National Academy of Sciences **104**(5), 1476–1481 (2007).

[Hol14] M. Holzmann, private communications (2014).

[Hun11] C.-L. Hung, X. Zhang, N. Gemelke, C. Chin, *Observation of scale invariance and universality in two-dimensional Bose gases*, Nature **470**(7333), 236–239 (2011).

[Ima09] A. Imambekov, I. E. Mazets, D. S. Petrov, V. Gritsev, S. Manz, S. Hofferberth, T. Schumm, E. Demler, J. Schmiedmayer, *Density ripples in expanding low-dimensional gases as a probe of correlations*, Phys. Rev. A **80**, 033604 (Sep 2009).

[Isk09] M. Iskin, C. A. R. S. de Melo, *Evolution from BCS to Berezinskii-Kosterlitz-Thouless Superfluidity in One-Dimensional Optical Lattices*, Phys. Rev. Lett. **103**, 165301 (Oct 2009).

[Joc03] S. Jochim, M. Bartenstein, A. Altmeyer, G. Hendl, S. Riedl, C. Chin, J. Hecker Denschlag, R. Grimm, *Bose-Einstein Condensation of Molecules*, Science **302**(5653), 2101–2103 (Dezember 2003).

[Jos13] J. V. José (Ed.), *40 years of Berezinskii-Kosterlitz-Thouless Theory* (World Scientific, New Jersey, 2013).

[Kan09] A. Kantian, M. Dalmonte, S. Diehl, W. Hofstetter, P. Zoller, A. J. Daley, *Atomic Color Superfluid via Three-Body Loss*, Phys. Rev. Lett. **103**(24), 240401– (Dezember 2009).

[Kap33] P. L. Kapitza, P. A. M. Dirac, *The reflection of electrons from standing light waves*, Mathematical Proceedings of the Cambridge Philosophical Society **29**, 297–300 (5 1933).

[Ket08] W. Ketterle, M. W. Zwierlein, *Making, probing and understanding ultracold fermi gases*, Proc. of the International School of Physics 'Enrico Fermi', Course CLXIV (2008).

[Kos73] J. M. Kosterlitz, D. J. Thouless, *Ordering, metastability and phase transitions in two-dimensional systems*, Journal of Physics C: Solid State Physics **6**(7), 1181 (1973).

[Kos12] M. Koschorreck, D. Pertot, E. Vogt, B. Fröhlich, M. Feld, M. Köhl, *Attractive and repulsive Fermi polarons in two dimensions*, Nature **485**(7400), 619 (Mai 2012).

[Krü07] P. Krüger, Z. Hadzibabic, J. Dalibard, *Critical Point of an Interacting Two-Dimensional Atomic Bose Gas*, Phys. Rev. Lett. **99**, 040402 (Jul 2007).

[Ku12] M. J. H. Ku, A. T. Sommer, L. W. Cheuk, M. W. Zwierlein, *Revealing the Superfluid Lambda Transition in the Universal Thermodynamics of a Unitary Fermi Gas*, Science **335**, 563–567 (2012).

[Lan13] T. Langen, *Comment on "Probing Phase Fluctuations in a 2D Degenerate Bose Gas by Free Expansion"*, Phys. Rev. Lett. **111**, 159601 (Oct 2013).

[Leg80] A. J. Leggett, *Cooper pairing in spin-polarized Fermi systems*, J. Phys. (Paris) Coll. **41**, C7–19 (1980).

[Lev14] J. Levinsen, M. M. Parish, *Strongly interacting two-dimensional Fermi gases*, ArXiv e-prints (August 2014).

[Mak14] V. Makhalov, K. Martiyanov, A. Turlapov, *Ground-State Pressure of Quasi-2D Fermi and Bose Gases*, Phys. Rev. Lett. **112**, 045301 (Jan 2014).

[Mar10] K. Martiyanov, V. Makhalov, A. Turlapov, *Observation of a Two-Dimensional Fermi Gas of Atoms*, Phys. Rev. Lett. **105**, 030404 (2010).

[McK11] D. McKay, B. DeMarco, *Cooling in strongly correlated optical lattices: prospects and challenges*, Rep. Prog. Phys. 74 054401 (Oktober 2011).

[Mer66] N. D. Mermin, H. Wagner, *Absence of Ferromagnetism or Antiferromagnetism in One- or Two-Dimensional Isotropic Heisenberg Models*, Phys. Rev. Lett. **17**, 113 (1966).

[Met02] H. J. Metcalf, P. v. Straten, *Laser cooling and trapping*, Graduate texts in contemporary physics (Springer, New York ; Berlin ; Heidelberg [u.a.], 2002), corr. 2. print Edn.

[Mur14a] S. Murmann, A. Bergschneider, V. M. Klinkhamer, G. Zürn, T. Lompe, S. Jochim, *Two Fermions in a double well: Exploring a fundamental building block of the Hubbard model*, ArXiv e-prints (Oktober 2014).

[Mur14b] P. A. Murthy, D. Kedar, T. Lompe, M. Neidig, M. G. Ries, A. N. Wenz, G. Zürn, S. Jochim, *Matter-wave Fourier optics with a strongly interacting two-dimensional Fermi gas*, Phys. Rev. A **90**, 043611 (Oct 2014).

[Nas10] S. Nascimbène, N. Navon, K. J. Jiang, F. Chevy, C. Salomon, *Exploring the thermodynamics of a universal Fermi gas*, Nature **463**(7284), 1057–1060 (2010).

[Nei13] M. Neidig, *A realization of a two-dimensional Fermi gas in a standing wave trap* (2013), Master thesis, Ruprecht-Karls-Universität Heidelberg.

[Nel77] D. R. Nelson, J. M. Kosterlitz, *Universal Jump in the Superfluid Density of Two-Dimensional Superfluids*, Phys. Rev. Lett. **39**, 1201–1205 (Nov 1977).

[Nga13] V. Ngampruetikorn, J. Levinsen, M. M. Parish, *Pair Correlations in the Two-Dimensional Fermi Gas*, Phys. Rev. Lett. **111**, 265301 (Dec 2013).

[Nor11] M. R. Norman, *The Challenge of Unconventional Superconductivity*, Science **332**(6026), 196–200 (2011).

[Ock10] C. F. Ockeloen, A. F. Tauschinsky, R. J. C. Spreeuw, S. Whitlock, *Detection of small atom numbers through image processing*, Phys. Rev. A **82**, 061606 (Dec 2010).

[Ott08] T. B. Ottenstein, T. Lompe, M. Kohnen, A. N. Wenz, S. Jochim, *Collisional Stability of a Three-Component Degenerate Fermi Gas*, Phys. Rev. Lett. **101**(20), 203202– (November 2008).

[Pau25] W. Pauli, *Über den Zusammenhang des Abschlusses der Elektronengruppen im Atom mit der Komplexstruktur der Spektren*, Zeitschrift für Physik **31**(1), 765–783 (1925).

[Pet00] D. S. Petrov, M. Holzmann, G. V. Shlyapnikov, *Bose-Einstein Condensation in Quasi-2D Trapped Gases*, Phys. Rev. Lett. **84**, 2551–2555 (2000).

[Pet01] D. S. Petrov, G. V. Shlyapnikov, *Interatomic collisions in a tightly confined Bose gas*, Phys. Rev. A **64**, 012706 (Jun 2001).

[Pet02] C. J. Pethick, H. Smith, *Bose-Einstein Condensation in Dilute Gases* (Cambridge University Press, 2002).

[Pet03] D. S. Petrov, M. A. Baranov, G. V. Shlyapnikov, *Superfluid transition in quasi-two-dimensional Fermi gases*, Phys. Rev. A **67**, 031601 (Mar 2003).

[Pit03] L. Pitaevskii, S. Stringari, *Bose-Einstein Condensation*, International Series of Monographs on Physics - 116 (Oxford University Press, 2003).

[Pli11] T. Plisson, B. Allard, M. Holzmann, G. Salomon, A. Aspect, P. Bouyer, T. Bourdel, *Coherence properties of a two-dimensional trapped Bose gas around the superfluid transition*, Phys. Rev. A **84**, 061606 (Dec 2011).

[Pre14] S. Pres, *BKT-phase transition in a strongly interacting 2d Bose gas* (2014), Master thesis, Ruprecht-Karls-Universität Heidelberg.

[Pri11] A. Privitera, I. Titvinidze, S.-Y. Chang, S. Diehl, A. J. Daley, W. Hofstetter, *Loss-induced phase separation and pairing for three-species atomic lattice fermions*, Phys. Rev. A **84**, 021601 (Aug 2011).

[Pro01] N. Prokof'ev, O. Ruebenacker, B. Svistunov, *Critical Point of a Weakly Interacting Two-Dimensional Bose Gas*, Phys. Rev. Lett. **87**, 270402 (Dec 2001).

[Pro02] N. Prokof'ev, B. Svistunov, *Two-dimensional weakly interacting Bose gas in the fluctuation region*, Phys. Rev. A **66**, 043608 (Oct 2002).

[Ran89] M. Randeria, J.-M. Duan, L.-Y. Shieh, *Bound states, Cooper pairing, and Bose condensation in two dimensions*, Phys. Rev. Lett. **62**, 981–984 (Feb 1989).

[Rap07] A. Rapp, G. Zaránd, C. Honerkamp, W. Hofstetter, *Color Superfluidity and "Baryon" Formation in Ultracold Fermions*, Phys. Rev. Lett. **98**(16), 160405 (Apr 2007).

[Reg04] C. A. Regal, M. Greiner, D. S. Jin, *Observation of Resonance Condensation of Fermionic Atom Pairs*, Phys. Rev. Lett. **92**(4), 040403–4 (2004).

[Rie10] M. G. Ries, *A magneto-optical trap for the preparation of a three-component Fermi gas in an optical lattice* (2010), Diploma thesis, Ruprecht-Karls-Universität Heidelberg.

[Rie14] M. G. Ries, A. N. Wenz, G. Zürn, L. Bayha, I. Boettcher, D. Kedar, P. A. Murthy, M. Neidig, T. Lompe, S. Jochim, *Observation of pair condensation in a strongly interacting two-dimensional Fermi gas*, ArXiv e-prints (September 2014).

[Rud01] P. Rudy, R. Ejnisman, A. Rahman, S. Lee, N. P. Bigelow, *An all optical dynamical dark trap for neutral atoms*, Opt. Express **8**(2), 159–165 (Jan 2001).

[Sak94] J. J. Sakurai, *Modern Quantum Mechanics* (Addison-Wesley Publishing Company, Inc., 1994).

[Sal07] B. E. A. Saleh, M. C. Teich, *Fundamentals of photonics*, Wiley series in pure and applied optics (Wiley, Hoboken, N.J., 2007), 2nd Edn.

[Sch93] A. Schilling, M. Cantoni, J. D. Guo, H. R. Ott, *Superconductivity above 130 K in the Hg-Ba-Ca-Cu-O system*, Nature **363**(6424), 56–58 (Mai 1993).

[Sch99] U. Schünemann, H. Engler, R. Grimm, M. Weidemüller, M. Zielonkowski, *Simple scheme for tunable frequency offset locking of two lasers*, Rev. Sci. Instrum. **70**(1), 242–243 (Januar 1999).

[Ser11] F. Serwane, *Deterministic preparation of a tunable few-fermion system*, Dissertation, Ruprecht-Karls-Universität Heidelberg, http://www.mpi-hd.mpg.de/biblio/preprints/2011-048.pdf (2011).

[She10] J. F. Sherson, C. Weitenberg, M. Endres, M. Cheneau, I. Bloch, S. Kuhr, *Single-atom-resolved fluorescence imaging of an atomic Mott insulator*, Nature **467**(7311), 68–72 (2010).

[Sim10] P. Simon, *Apparatus for the preparation of ultracold Fermi gases* (2010), Diploma thesis, Ruprecht-Karls-Universität Heidelberg.

[Sin14] V. P. Singh, L. Mathey, *Noise correlations of two-dimensional Bose gases*, Phys. Rev. A **89**, 053612 (May 2014).

[Som12] A. T. Sommer, L. W. Cheuk, M. J. H. Ku, W. S. Bakr, M. W. Zwierlein, *Evolution of Fermion Pairing from Three to Two Dimensions*, Phys. Rev. Lett. **108**, 045302 (2012).

[Sya08] N. Syassen, D. M. Bauer, M. Lettner, T. Volz, D. Dietze, J. J. García-Ripoll, J. I. Cirac, G. Rempe, S. Dürr, *Strong Dissipation Inhibits Losses and Induces Correlations in Cold Molecular Gases*, Science **320**(5881), 1329–1331 (2008).

[Tan08] S. Tan, *Large momentum part of a strongly correlated Fermi gas*, Annals of Physics **323**(12), 2971 – 2986 (2008).

[Tun10] S. Tung, G. Lamporesi, D. Lobser, L. Xia, E. A. Cornell, *Observation of the Presuperfluid Regime in a Two-Dimensional Bose Gas*, Phys. Rev. Lett. **105**, 230408 (2010).

[Wei09] M. Weidemüller, C. Zimmermann, *Cold Atoms and Molecules*, Physics textbook (Wiley, 2009).

[Wei14] W. Weimer, K. Morgener, V. P. Singh, J. Siegl, K. Hueck, N. Luick, L. Mathey, H. Moritz, *The critical velocity in the BEC-BCS crossover*, ArXiv e-prints (August 2014).

[Wen13] A. Wenz, *From Few to Many: Ultracold Atoms in Reduced Dimensions*, Dissertation, Ruprecht-Karls-Universität Heidelberg, http://www.lithium6.de/publications (2013).

[Wil07] F. Wilczek, *Quantum chromodynamics: Lifestyles of the small and simple*, Nature Physics **3**, 375–376 (2007).

[Wu87] M. K. Wu, J. R. Ashburn, C. J. Torng, P. H. Hor, R. L. Meng, L. Gao, Z. J. Huang, Y. Q. Wang, C. W. Chu, *Superconductivity at 93 K in a new mixed-phase Y-Ba-Cu-O compound system at ambient pressure*, Phys. Rev. Lett. **58**, 908–910 (Mar 1987).

[Yan13] B. Yan, S. A. Moses, B. Gadway, J. P. Covey, K. R. A. Hazzard, A. M. Rey, D. S. Jin, J. Ye, *Observation of dipolar spin-exchange interactions with lattice-confined polar molecules*, Nature **501**(7468), 521–525 (September 2013).

[Zha12] Y. Zhang, W. Ong, I. Arakelyan, J. E. Thomas, *Polaron-to-Polaron Transitions in the Radio-Frequency Spectrum of a Quasi-Two-Dimensional Fermi Gas*, Phys. Rev. Lett. **108**, 235302 (Jun 2012).

[Zür09] G. Zürn, *Realization of an Optical Microtrap for a Highly Degenerate Fermi Gas* (2009), Diploma thesis, Ruprecht-Karls-Universität Heidelberg.

[Zür13] G. Zürn, T. Lompe, A. N. Wenz, S. Jochim, P. S. Julienne, J. M. Hutson, *Precise Characterization of* ^{6}Li *Feshbach Resonances Using Trap-Sideband-Resolved RF Spectroscopy of Weakly Bound Molecules*, Phys. Rev. Lett. **110**, 135301 (Mar 2013).

[Zwe11] W. Zwerger, *The BCS-BEC Crossover and the Unitary Fermi Gas*, Lecture Notes in Physics (Springer, 2011).

[Zwi03] M. W. Zwierlein, C. A. Stan, C. H. Schunck, S. M. F. Raupach, S. Gupta, Z. Hadzibabic, W. Ketterle, *Observation of Bose-Einstein Condensation of Molecules*, Phys. Rev. Lett. **91**, 250401 (2003).

[Zwi04] M. W. Zwierlein, C. A. Stan, C. H. Schunck, S. M. F. Raupach, A. J. Kerman, W. Ketterle, *Condensation of Pairs of Fermionic Atoms near a Feshbach Resonance*, Phys. Rev. Lett. **92**, 120403 (2004).

[Zwi05] M. W. Zwierlein, J. R. Abo-Shaeer, A. Schirotzek, C. H. Schunck, W. Ketterle, *Vortices and superfluidity in a strongly interacting Fermi gas*, Nature **435**, 1047–1051 (2005).

[Zwi06] M. W. Zwierlein, *High-Temperature Superfluidity in an Ultracold Fermi Gas*, Dissertation, Massachusetts Institute of Technology (2006).

Danksagung

Ich bedanke mich herzlich bei allen, die zum Gelingen dieser Arbeit beigetragen haben, insbesondere bei

- Selim, für die Möglichkeit, diese Doktorarbeit durchzuführen, die mir viel Spaß gemacht hat. Außerdem für die hervorragende Betreuung, deinen ansteckenden Enthusiasmus, und dafür, dass du immer ein offenes Ohr und eine Lösung für alle Fragen und Probleme hast. Ich habe viel von dir gelernt!
- der gesamten Ultracold-Gruppe: Friedhelm, Timo, Thomas, Andre, Gerhard, Philipp, Johanna, Andrea, Vincent, Mathias, Simon, Jan-Hendrik, Puneet, Sebastian, Dhruv, Luca, sowie unserem Ehrenmitglied Igor. Für eure Hilfe im Labor und am Schreibtisch, für's Korrekturlesen, aber auch für eine tolle Atmosphäre und jede Menge Spaß. Für Schneeballschlachten, Feuerzangenbowle mit Stichflamme, die ganze Nacht lang Doktorhüte basteln, wilde Diskussionen, und am Ende doch immer noch alles zum Laufen bringen. Ohne euch wäre diese Arbeit nicht möglich gewesen!
- Tilman Enss, Jesper Levinsen, Pietro Massignan, Ludwig Mathey und Meera Parish für wichtige Diskussionen über 2D Physik, sowie Markus Holzmann für die Simulation unserer Korrelationsfunktionen.
- Prof. Matthias Weidemüller für die freundliche Übernahme des Zweitgutachtens.
- Prof. Thomas Gasenzer und Prof. Ulrich Platt für die Bereitschaft, Teil meiner Prüfungskommission zu sein.
- dem MPI für Kernphysik, insbesondere der Gruppe Ullrich und Prof. Klaus Blaum sowie Helga Krieger, für die freundliche Aufnahme unserer Arbeitsgruppe und dass wir nicht zwei mal umziehen mussten.
- der Gruppe Weidemüller für den produktiven Austausch und viele Kickerspiele. Außerdem für die freundliche Leihgabe des Nufern fiber amplifiers, als unserer mal wieder kaputt war.

- der mechanischen Werkstatt am MPI für die Herstellung vieler Bauteile, die unsere Experimente überhaupt erst möglich machen. Mein besonderer Dank gilt Florian Säubert von der MPI Lehrwerkstatt für die hervorragende Arbeit beim Bau der Feshbachspulen und des Interferometers für die Stehwellenfalle.
- den Werkstätten am PI, insbesondere Herrn Ziegler und Herrn Angelov für die Herstellung vieler Bauteile, die unsere Experimente überhaupt erst möglich machen. Außerdem für die tatkräftige Unterstützung bei unserem Umzug ans PI, sowie dabei, die Infrastruktur in den neuen Laboren zum Laufen zu bringen.
- Dominic Litsch für die Hilfe bei Lasersicherheit und Laboreinrichtung.
- Ulrich Schmidt für die freundliche Hilfe bei zahlreichen Kühlwasser- und Klimanotfällen in der Anfangsphase am PI.
- der EDV-Abteilung am PI, insbesondere Jörg Marks für Verhandlungen mit dem URZ, und Norman Jooß und Kai Worsch für die Hilfe dabei, unsere IT-Infrastruktur in das Netzwerk einzubinden.
- dem gesamten PI für die freundliche Aufnahme, insbesondere Frau Krämer, die uns vor viel Bürokratie beschützt.
- meinen Freunden für gemeinsame Urlaube, Wochenendaktivitäten, nette Abende oder einfach zusammen zu Mittag essen.
- meinen Eltern und Geschwistern dafür, dass ihr immer hinter mir steht. Und dass ich immer gerne zu euch nach Hause komme.
- Monica, für deine Unterstützung und dein Verständnis in den letzten Wochen und Monaten. Und einfach nur dafür, dass es dich gibt.